NWRI — UNPUBLISHED
DONELAN, M (1983)

Environment Canada

Environnement Canada

CANADA CENTRE FOR INLAND WATERS

CENTRE CANADIEN DES EAUX INTERIEURES

National Water Research Institute

Institut national de la recherche sur les eaux

DIRECTIONAL SPECTRA OF WIND-GENERATED WAVES

by

M. A. Donelan[1], J. Hamilton[2,3] and W. H. Hui[2]

TD
7
D664
1983

Canada

This manuscript has been submitted to the
Philosophical Transactions of the Royal Society of London

DIRECTIONAL SPECTRA OF WIND-GENERATED WAVES

by

M. A. Donelan[1], J. Hamilton[2,3]
and W. H. Hui[2]

[2]Department of Applied Mathematics
University of Waterloo

[3]Current Affiliation:
Vickers-Offshore, Barrow-in-Furness, England

[1]Shore Processes Section
Hydraulics Division
National Water Research Institute
Canada Centre for Inland Waters
Burlington, Ontario
January 1983

TABLE OF CONTENTS

	Page
ABSTRACT	iii
MANAGEMENT PERSPECTIVE	v
1. **INTRODUCTION**	1
2. **FUNDAMENTALS OF WIND WAVES**	5
2.1 Irrotational Waves	5
2.1.1 Governing equations	5
2.1.2 Free waves	6
2.1.3 Forced waves	8
2.2 Statistical Representation of the Wave Field	11
2.3 Nonlinear Wave-Wave Interactions	13
3. **EXPERIMENTAL ARRANGEMENTS**	15
3.1 Field Site	15
3.2 Array Design	16
3.3 Wave Staffs	17
3.4 Meteorological Measurements	20
4. **ANALYSIS METHOD**	21
4.1 Introduction	21
4.2 The Modified Barber Method	23
4.3 Some Sources of Error	29
5. **SUMMARY OF DATA**	32
6. **TYPICAL DIRECTIONAL SPECTRA**	36
6.1 Field Wave-Number Frequency Spectra	36
6.2 Laboratory Wave-Number Frequency Spectra	37
7. **POLAR ANALYSIS**	38
7.1 Introduction	38
7.2 Parametric Representation	40
8. **THE FREQUENCY SPECTRUM**	45
8.1 The Rear Face	46
8.2 The Parameters of the Spectrum	50
8.3 Non-Dimensional Fetch and Energy	53
8.4 Comparison with Other Spectra	55
8.5 The Equilibrium Level Versus Wind Speed	56

		Page
9.	**WAVE DIRECTION VERSUS WIND DIRECTION**	59
10.	**PHASE SPEED**	61
	10.1 'Average' Phase Speed	61
	10.2 Phase Speed of Free Waves	64
	10.3 Phase Speed of Bound Harmonics	65
	10.4 Amplitude Dispersion and Doppler Shift of Laboratory Waves	66
	10.5 Amplitude Dispersion of Field Waves	69
	10.6 Root Mean Square Slope	71
11.	**DIRECTIONAL DISTRIBUTIONS OF WAVE ENERGY**	74
	11.1 Introduction	74
	11.2 L and θ_A Dependence	76
	11.3 The s Parameter	77
	11.4 The $\cos^{2m}\theta$ Spreading Function	81
	11.5 The $\mathrm{Sech}^2(\beta\theta)$ Spreading Function	82
	11.6 Dependence on ω/ω_p	84
	11.7 The Directional Spread of the Forward Face	85
12.	**CONCLUDING REMARKS**	87
APPENDIX		90
	DETAILS OF THE DIRECTIONAL SPECTRUM ANALYSIS METHOD	
REFERENCES		97
ACKNOWLEDGEMENTS		
FIGURES		

ABSTRACT

From observations of wind and of water surface elevation at 14 wave staffs in an array in Lake Ontario and in a large laboratory tank, the directional spectrum of wind-generated waves on deep water is determined using a modification of Barber's (1963) method. Systematic investigations reveal the following: (a) the frequency spectrum in the rear face is proportional to the minus 4 power of the frequency ω with the equilibrium range parameter and the peak enhancement factor clearly dependent on the ratio of wind speed to peak wave speed; (b) the angular spreading θ of the wave energy is of the form $\mathrm{sech}^2\ \beta\theta$, where β is a function of frequency relative to the peak; (c) depending on the gradient of the fetch, the direction of the wave at the spectral peak may differ from the mean wind direction by up to 50°f, but this observed difference is predictable by a similarity analysis; (d) under conditions of strong wind forcing, significant effects on the phase velocity due to amplitude dispersion and the presence of bound harmonics are clearly observed which are in accordance with Stokes theory, whereas (e) the waves under natural wind condition show amplitude dispersion, but bound harmonics are too weak to be detected among the background of free waves.

RÉSUMÉ

À partir d'observations du vent et du niveau de l'eau dans un réseau de 14 bouées réparties sur le lac Ontario et sur un grand bassin de laboratoire, on a établi le spectre directionnel des vagues soulevées par le vent en eau profonde, en utilisant une version modifiée de la méthode de Barber (1963). Des recherches systématiques ont révélé: a) que le spectre de fréquence à l'arrière est inversement proportionnel à la puissance quatrième de la fréquence , le paramètre d'intervalle d'équilibre et le facteur de grossissement maximal étant fonctions du rapport de la vitesse du vent à la vitesses maximale des vagues; b) que la dispersion angulaire de l'énergie des vagues est de la forme $\text{sech}^2\ \beta\theta$, où β est une fonction de la fréquence par rapport au maximum; c) que, selon le gradient du fetch, la direction de la vague au maximum spectral peut s'écarter de la direction moyenne du vent par autant que 50°, cette différence observée étant prévisible par analyse de similitude; d) que, en conditions de vent violent, on peut nettement observer les importants effets de la dispersion d'amplitude et de la présence d'harmoniques limites sur la vitesse de phase, effets qui sont en accord avec la théorie de Stokes, tandis que e) les vagues soulevées par des vents normaux présentent une dispersion d'amplitude, mais les harmoniques limites sont trop faibles pour être détectées dans le bruit de fond des vagues libres.

MANAGEMENT PERSPECTIVE

An accurate description of the spectrum of wind-generated waves is required in coastal engineering, offshore structure design, naval architecture, interpreting satellite imagery and in numerical forecasting or hindcasting of waves. This report describes the most comprehensive attempt yet made to tie down the distribution of wave energy in direction and frequency and also the speed of propagation of different wave components. Some well known theories have been verified and other unexpected results have turned up, which will have a fundamental effect on the application of wave theory to practical purposes.

Although the study draws on laboratory and lake data, the results are presented in non-dimensional form and easily scaled up to oceanic conditions. A lake presents some significant advantages over an ocean for this sort of research - fetch limits imposed by the shoreline permit the study of very young (undeveloped) waves such as might be found in typical oceanic storms or in reservoirs. In fact, in the context of wind-generated waves, Lake Ontario is an ocean with well defined lateral boundaries.

The extraordinary length of this report reflects the authors determination to keep together the intimately connected parts of this work.

T. Milne Dick
Chief, Hydraulics Division
February 1983

PERSPECTIVE DE GESTION

Une description précise du spectre des vagues soulevées par le vent est nécessaire dans les domaines suivants: génie côtier, conception d'ouvrages marins, architecture navale, interprétation des images de satellite et prévision numérique ou a posteriori des vagues. Le présent rapport décrit la tentative la plus sérieuse pour établir la distribution de l'énergie des vagues en fonction de la direction et de la fréquence, et pour calculer la vitesse de propagation des différentes composantes des vagues. Certaines théories bien connues ont été vérifiées et d'autres résultats inattendus auront une incidence considérable sur la mise en application de la théorie des vagues.

Même si l'étude s'appuie sur des données prises en laboratoire et dans le lac, les résultats sont présentés sous forme adimensionnelle et peuvent être facilement ramenés à l'échelle océanique. L'étude d'un lac plutôt que d'un océan présente des avantages dans ce genre de recherche: à cause des fetchs limités par la ligne de rivage, on peut étudier de très jeunes vagues (non développées) comme on en observe dans les tempêtes océaniques types ou dans les réservoirs. En fait, à l'échelle des vagues de vent, le lac Ontario est un océan aux limites latérales bien définies.

L'ampleur du rapport dénote la détermination des auteurs à présenter comme un tout les éléments, étroitement liés entre eux, de cette recherche.

T. Milne Dick, Chef
Division de l'hydraulique
février 1983

1. INTRODUCTION

Directional spectra of wind-generated waves find application in fields as diverse as basic air-sea interaction, upper mixed layer dynamics, practical wave forecasting, satellite surveillance and engineering design of marine structures and vehicles. In recent years, the concept of a simple but "significant" wave has been nearly displaced by statistical descriptions of the sea-surface based largely on fetch-limited data. This paper attempts to provide a carefully documented description of the purely wind-generated wave directional spectrum derived from lake data which is free of residual wave energy (swell). Laboratory spectra are used to extend our understanding of strongly forced natural waves.

By far the most widely used and accepted method of studying wind waves has been by examination of the spectra of single point time traces of the wave surface elevation. This has been born of the recognition that observed sea states require a statistical description, and that the theoretical shape for waves of small amplitude is a sinusoid (Airy, 1845). Hence, by the principle of linear superposition, the spectral representation is a natural description of wave kinematics.

The form of the (second order) nonlinear correction to the sinusoidal form of water waves was first computed by Stokes (1847). This correction predicts the familiar narrow high crest and broad shallow trough intuitively recognized in observations of wind-generated waves, together with an associated increase in the wave phase speed. In terms of the spectral representation, this would appear as enhanced energy at frequencies equal to integral multiples of the wave spectral peak frequency and alterations in the distribution in wave-number space of the directional spectrum. The first of these features has often been recognized in spectral observations (e.g. Sutherland, 1967; Kinsman, 1960), however, it is only recently that the changed phase speed has been verified using correlations between adjacent wave height measurements (Ramamonjiarisoa, 1974).

Now, as soon as nonlinear features begin to be discussed, the principle of superposition is no longer applicable and the spectral representation, although still possible must be treated with care, especially when seeking to interpret any higher order features which may be present. Indeed, it has been shown by Whitham (1967) that the frequency dispersion introduced by the Stokes correction to the phase speed will tend to destabilize a train of uniform parallel crested waves. Thus, the wave spectrum should not be regarded as representing a permanent description of the sea state which would be maintained in the absence of wind forces and viscous dissipation, instead the spectrum will be in a state of flux through nonlinear interaction of the various spectral components.

Fortunately, however, the second order nonlinear or Stokes' interactions do not result in large frequency shifts of the wave energy. The instability of a Stokes wave train was first discovered by Brooke Benjamin (1967) as a 'side band' instability which would eventually cause wave breaking but could not transfer energy to other than adjacent frequencies.

Phillips (1960) has shown that the third order nonlinearities which transfer energy from three waves to a fourth, are the first ones which can cause continuous energy transfer over large frequency distances to a free wave. The size of this transfer was first computed by Hasselmann et al. (1973), and has since been the subject of many papers: Hasselmann (1962, 1963a, 1963b), Fox (1976), Longuet-Higgins (1976), Korvin-Kroukovsky (1967), Zakharov (1968), Webb (1978), Dungey and Hui (1979). However, because of their high order, these interactions are only of importance when discussing the evolution of the wave spectra with time or fetch. Observations of wave spectra at a particular point in time and space might be supposed to exhibit principally features associated with linear wave theory and the Stokes' corrections to it. However, to verify that this is indeed the case requires knowledge not simply of the one-dimensional frequency spectrum but of the three-dimensional directional spectrum which describes the wavelength and directional distributions of each frequency component. For this reason and others associated with the practical matter of wave forecasting, much attention has recently been

paid to obtaining estimates of the directional spectrum of wind-generated waves.

Barnett and Kenyon (1975), in a recent review of the study of wind waves, discussed the methods then available for the measurement of directional spectra. At that time, some measurements had been made of what we call the two-dimensional spectrum, i.e., in which the radian wave-number k and the (radian) frequency ω were assumed to satisfy the linear dispersion relation on deep water.

$$\omega^2 = gk. \tag{1.1}$$

Using aerial photogrammetry, Cote et al. (1960) had obtained the first wave-number (two-dimensional) spectrum. But, apart from a pioneering attempt by Garratt (1970), who had obtained four spectra, no systematic attempt to explore the properties of the full three-dimensional (wave-number frequency) spectrum had come to light.

Since that time, a completely new family of methods has become available for measuring the two- and three-dimensional spectra, namely, using remote techniques (e.g., Tyler et al. 1974; Trizna, Bogle, Moore and Howe, 1980; Schuler 1978; Pawka, Hsiao, Shemdin and Inman 1980; Mcleish et al. 1980; Fontanel and DeStaerke 1980; Irani et al. 1981; Holthuijsen 1981; Wu, 1977). Among the established methods reported by Barnett and Kenyon (1975) are those using the pitch-roll and cloverleaf buoys (Longuet-Higgins et al. 1963, Hasselman et al. 1980), and the measurements from an array of wave staffs. The disadvantage of the pitch-roll and cloverleaf buoys is that the linear dispersion relationship must be assumed and that only the first few Fourier coefficients of the angular distribution of the spectral energy density can be determined. This study was undertaken using an array of wave staffs, thus allowing the calculation of much finer detail in the directional distribution, at some cost in computer time.

The present investigation began in 1975 when a tower was built at the western end of Lake Ontario to record wave data and wind data in order to determine the directional spectrum of wind-generated waves. Complimentary laboratory experiments of wind-generated waves were performed in the large wind-wave tank of the Canada Centre for Inland Waters.

Our primary purposes in conducting this study are:

(i) determine the dispersion relation appropriate to natural wind waves.

(ii) describe the fetch-limited frequency spectrum in terms of a small number of parameters.

(iii) find a parametric representation for the spreading function of the directional distribution.

(iv) use laboratory data to extend the parameter range of field observations.

In addition the data set is of very high quality and allows new information to be obtained on many problems previously not resolved, for example, the dependence of the spectral shape parameters on fetch and wave age, a more detailed look at the polar distribution of the spectral density, and its dependence on wave frequency and other parameters.

Details of the array design are described in §3 and the outline of analysis of the directional spectrum from the wave data based on Barber's (1963) idea is given in §4, with details given in the appendix.

A summary of data of the experiments is given in §5, followed by a description in §6 of typical three-dimensional spectra observed in Lake Ontario and in the laboratory. The polar analyses of the directional spectrum are given in §7. In §8 we attempt to parameterize the fetch-limited frequency spectrum and in §9 we show that peak propagation directions may be forecast even in areas of appreciable fetch gradient. §10 is devoted to an exploration of the dispersion relation of first laboratory and then field waves, followed by the parameterization of the polar directional distribution in §11. A summary of our findings is provided in §12 including a list of the parametric formulae required to describe the energy content, propagation speeds and directional spread of wind-generated waves.

We begin with a discussion of the fundamental theory underlying the analysis and interpretation of the spectra of wind-generated surface gravity waves.

2. FUNDAMENTALS OF WIND WAVES

In this section, a brief summary and extension of the fundamental results of wind waves is given which will be used in later sections of the paper. Surface tension of water will be neglected throughout as the waves observed and discussed in this paper are long enough for it to play no significant role.

2.1 Irrotational Waves

2.1.1 Governing equations

Observation suggests that, to a good first approximation, surface wave can be regarded as irrotational, for which the velocity potential ϕ satisfies

$$\nabla^2\phi = 0 \tag{2.1}$$

$$\frac{\partial\phi}{\partial z} = 0 \qquad \text{at } z = -h \tag{2.2}$$

$$\frac{\partial\zeta}{\partial t} + \frac{\partial\phi}{\partial x}\frac{\partial\zeta}{\partial x} + \frac{\partial\phi}{\partial y}\frac{\partial\zeta}{\partial y} - \frac{\partial\phi}{\partial z} = 0, \qquad \text{at } z = \zeta \tag{2.3}$$

$$\frac{\partial\phi}{\partial t} + \frac{1}{2}(\nabla\phi)^2 + g\zeta = -p_a/\rho_w, \qquad \text{at } z = \zeta \tag{2.4}$$

where t is the time variable, (x, y, z) cartesian coordinates with z measured vertically upwards from the equilibrium water surface, h the water depth (assumed constant), $\zeta(x, y, t)$ the water surface elevation, ρ_w water density, and p_a the pressure of the wind in excess of its equilibrium value. Waves are called free waves or forced waves according as $p_a = 0$ or not.

For infinitesimal (slope) waves, the boundary conditions (2.3) and (2.4) may be simplified by neglecting higher order terms, resulting in

$$\frac{\partial^2 \phi}{\partial t^2} + g \frac{\partial \phi}{\partial z} = - \frac{1}{\rho_w} \frac{\partial p_a}{\partial t} \qquad \text{at } z = 0 \tag{2.5}$$

When p_a is zero or has a sinusoidal dependence on time and the horizontal coordinate vector $\underset{\sim}{x} = (x, y)$, as is likely the case in wind wave generation, a solution to the linear equations (2.1), (2.2) and (2.5) exists in the following form

$$\phi = A \cosh k (z + h) \exp [i (\underset{\sim}{k} \cdot \underset{\sim}{x} - \omega t)], \; i = \sqrt{-1} \tag{2.6}$$

Where A is a constant, provided that the frequency ω and the magnitude of the horizontal wave-number vector $k = |\underset{\sim}{k}|$ satisfy certain dispersion relations as required by (2.5). The phase velocity $\underset{\sim}{c} = \omega/\underset{\sim}{k}$ also depends on the wave-number.

2.1.2 Free waves

For free waves, $p_a = 0$, the Stokes' wave has been calculated analytically to 11th order in wave slope (Hui & Tenti 1982). To second order:

$$\zeta = a \exp [i (kx - \omega t)] + \frac{k}{2} a^2 \exp [2i (kx - \omega t)] \tag{2.7}$$

When (2.3) and (2.4) are satisfied to the second order, the dispersion relation is (Whitham, 1974)

$$\omega^2 = gkT [1 + \frac{9T^4 - 10T^2 + 9}{8T^4} k^2 a^2] \tag{2.8}$$

where

$$T = \tanh kh \tag{2.9}$$

In the limit of infinitesimal waves on deep water, (2.8) reduces to (1.1). For a single train of harmonic waves, any departure from the linear dispersion relation must be due to one or more of the following effects: (a) finite amplitude, (b) finite depth (c) existence of currents and (d) forcing of the wind.

Comparisons of Equation (2.8) and (1.1) show that the effect of finite amplitude a or finite slope, is to increase the frequency ω for a given wave-number k or, equivalently, to decrease the wave-number (by at most about 20%) for a given frequency. This is generally called the (local) amplitude dispersion. Finite amplitude Stokes effects may also be due to the energy of the second (and possibly higher) harmonics of (2.7) at the peak frequency ω_p, say, appearing in the wave-number spectrum at frequencies $2\omega_p$, $3\omega_p$ etc. These will be called higher harmonic effects. For both effects, the energy density in the wave-number spectrum for a given frequency will appear inside the linear dispersion circle (1.1) in wave-number $\underset{\sim}{k}$ space: the local effect will shift the energy slightly inside the circle by up to about 20%, whereas the higher harmonic effect will shift it at least half-way inside. So, they are quite distinct. In both situations, the effect of finite wave amplitude is to increase the phase velocity.

On the other hand, it can also be seen from Equation (2.8) that the effect of finite depth h is to decrease the frequency for a given wave-number, or equivalently to increase the wave-number for given frequency (hence decreasing the phase velocity) except for very shallow water when $T^2 < (3/2)^3/^2$ ka; in that case, the effect is reversed. However, the latter is outside the scope of the present study. Thus for moderate depths, the finite depth effect is to move the energy density, in the wave-number space for a given frequency, slightly outside the linear dispersion circle (1.1). In fact, this effect is negligible in the cases discussed in this paper which correspond to deep water waves.

The water currents in the present investigation are quite small compared with the phase velocity of the wave. Their effects on

the dispersion relation are generally insignificant escept for laboratory waves. More detailed discussions are given in §10.

2.1.3 Forced waves

To see the effect of windforcing on the dispersion relation, consider, for simplicity, a train of infinitesimal waves

$$\zeta = ae^{i(kx - \omega t)} \tag{2.10}$$

travelling in x-direction under the action of the wind. On deep water, the velocity potential is of the form

$$\phi = -i \frac{a\omega}{k} e^{kz} e^{i(kx - \omega t)} \tag{2.11}$$

The wind pressure that acts on the irrotational wave consists of two parts: one that is associated and correlated with the wave form and the remainder that is random and uncorrelated with the wave form. To determine the effect of the wind pressure on the dispersion relation only the first part needs to be taken into account. It is found (Phillips 1977, p. 113) that the pressure field that is correlated with the wave form is necessarily

$$p_a = (\nu + i\mu)\, \rho_\omega g\zeta. \tag{2.12}$$

In (2.12), the part proportional to μ is in-phase with the wave slope and an important problem in wind-wave generation theory is the determination of μ, the growth rate. On the other hand, either by simple Bernoulli arguments or by more detailed consideration (Phillips 1977, p. 131), it can be shown that ν is always negative, i.e. the part in (2.12) proportional to ν is in antiphase with the surface elevation.

Substitution of (2.10) - (2.12) into (2.5) yields

$$\omega^2 = gk \left[(1 + \nu) + i\mu \right] . \tag{2.13}$$

The magnitude of μ, a measure of the shear stress of the wind, is necessarily small under normal generating conditions in nature. As to the magnitude of ν which is a measure of gustiness of the wind, although also small in most cases it has been observed (to be reported later) that under very active generating conditions $|\nu|$ may not be negligible. In those cases, the effect of the forcing by the wind is to decrease the frequency for a given wave-number or equivalently to increase the wave-number for a given frequency. This will move the energy density somewhat outside the linear dispersion circle (1.1) in wave-number space, similar to the effect of finite depth.

For studying the properties of wind-generated wave fields, it is interesting to ask how the forced waves generated by the forcing wind evolve after the pressure force is removed. To consider this problem, let a train of forced waves of infinitesimal amplitude on deep water be given by

$$\phi = A(k)\, e^{kz} e^{i(kx - \sigma t)} \tag{2.14}$$

where the frequency σ may differ from the frequency of the corresponding free wave $\omega(\omega^2 = gk)$. Once the pressure force is removed, the frequency σ and wave-number k must evolve with time so as to satisfy the free surface condition (2.5) with $p_a = 0$. Thus

$$\left[\frac{A'}{A} \dot{k} + ix\dot{k} - i(\sigma + t\dot{\sigma}) \right]^2$$

$$+ \left[\frac{A'}{A} \ddot{k} + \left(\frac{A''}{A} - \frac{A'^2}{A^2} \right) \dot{k}^2 + ix\ddot{k} - i \frac{d}{dt} (\sigma + t\dot{\sigma}) \right] + gk = 0 \tag{2.15}$$

For (2.15) to hold true for all x and t, we obtain

$$k = \text{const.} \tag{2.16}$$

$$(\sigma + t\dot{\sigma})^2 = gk. \tag{2.17}$$

Equation (2.16) says that the wave-number (hence the wave length) is unchanged upon the removal of the pressure force. On the other hand, Equation (2.17) yields the following solution

$$\sigma t = \omega t + \psi \tag{2.18}$$

where the constant of integration represents the excess of the forced wave frequency σ over that of the free wave ω at the initial time $t = 1$ when the wave was set free.

An interpretation of the above result is obtained by substituting (2.18) into (2.14). Thus we have

$$\phi = A(k)\, e^{kz}\, e^{i(kx - \omega t - \psi)} \tag{2.19}$$

which implies that once the pressure force p_a is removed, a forced wave instantaneously becomes a free wave of the same wave length but with a sudden decrease in its phase equal to the excess of the forced wave frequency compared to the corresponding frequency of a free wave with the same wave length. Accordingly, if the observed directional spectrum shows some energy density outside the linear dispersion relation in wave-number space, as reported in §6.1, this must be taken as evidence of the occurrence of forced waves over a significant duration.

2.2 Statistical Representation of the Wave Field

Although some aspects of wind-wave generation, propagation and decay can be discussed with single sinusoidal wave components as shown in §2.1, a more fruitful approach for a general wave field starts with a statistical description. The wave field is assumed to be both stationary and homogeneous and thus, according to the Ergodic Hypothesis, space and time averages are equivalent to ensemble averages which will be denoted with an over bar. Thus the covariance of the surface displacement

$$\rho(\underset{\sim}{r}, t) = \overline{\zeta(\underset{\sim}{x}, t_0)\,\zeta(\underset{\sim}{x} + \underset{\sim}{r}, t_0 + t)} \tag{2.20}$$

depends on the time lag t and the space lag $\underset{\sim}{r}$ only. Particular cases of (2.20) are the covariance of the instantaneous surface displacement $\rho(\underset{\sim}{r}) = \rho(\underset{\sim}{r}, 0)$ and the covariance of the surface displacement at a fixed point $\rho(t) = \rho(\underset{\sim}{0}, t)$. Some properties of the self-correlation function $\rho(t)$ are discussed in Hamilton, Hui and Donelan (1979).

The wave spectrum is the Fourier transform of $\rho(\underset{\sim}{r}, t)$

$$X(\underset{\sim}{k}, \omega) = (2\pi)^{-3} \iiint \rho(\underset{\sim}{r}, t) \exp\left[-i(\underset{\sim}{k}\cdot\underset{\sim}{r} - \omega t)\right] d\underset{\sim}{r}\, dt \tag{2.21}$$

In particular

$$\overline{\zeta^2} = \iiint X(\underset{\sim}{k}, \omega)\, d\underset{\sim}{k}\, d\omega \tag{2.22}$$

The wave-number spectrum is

$$\Psi(\underset{\sim}{k}) = \int X(\underset{\sim}{k}, \omega)\, d\omega \tag{2.23}$$

which is the Fourier transform of $\rho(\underset{\sim}{r})$

$$\Psi(\underset{\sim}{k}) = (2\pi)^{-2} \iint \rho(\underset{\sim}{r})\, e^{-i\underset{\sim}{k}.\underset{\sim}{r}}\, d^2\underset{\sim}{r} \tag{2.24}$$

The frequency direction spectrum $F(\omega, \theta)$ is defined as

$$F(\omega, \theta) = \int_0^\infty X(\underset{\sim}{k}, \omega)\, k dk \tag{2.25}$$

where

$$\underset{\sim}{k} = (k \cos\theta, k \sin\theta)$$

so that

$$\overline{\zeta^2} = \int_{-\pi}^{\pi} \int_0^\infty F(\omega, \theta)\, d\omega\, d\theta \tag{2.26}$$

Frequently, an approximate directional-frequency spectrum $F_0(\omega, \theta)$ is derived by assuming the linear dispersion relation (1.1). Thus

$$F_0(\omega, \theta) = \int_0^\infty \delta\left(k - \frac{\omega^2}{g}\right) X(\underset{\sim}{k}, \omega)\, k dk \tag{2.27}$$

The frequency spectrum $\Phi(\omega)$ defined as

$$\begin{aligned} \Phi(\omega) &= 2 \iint X(\underset{\sim}{k}, \omega)\, d^2\underset{\sim}{k} && \omega > 0 \\ &= 0 && \omega < 0 \end{aligned} \tag{2.28}$$

is the cosine transform of the self-correlation function

$$\Phi(\omega) = \frac{2}{\pi} \int_0^\infty \rho(t) \cos \omega t\, dt \tag{2.29}$$

and in particular

$$\overline{\zeta^2} = \int_0^\infty \Phi(\omega)\, d\omega \tag{2.30}$$

2.3 Nonlinear Wave-Wave Interactions

The growth of an individual wave component at sea is dependent upon the energy input from the wind, wind-wave interactions and wave breaking. The interaction among surface gravity waves is in general very weak. However, four waves may interact nonlinearly and resonantly, and under these circumstances nonlinear wave-wave interaction appears to be an important mechanism for energy exchange among surface wave components in the ocean. For a random wave field, the rate of energy transfer in this way was determined by Hasselmann (1962, 1963). In terms of the spectral density of wave action per unit mass

$$N(\underset{\sim}{k}) = \frac{g}{\omega}\, \Psi(\underset{\sim}{k}) \tag{2.31}$$

the net rate of increase of action density of the components at wave-number $\underset{\sim}{k}_1$ is of the form

$$\frac{\partial N(\underset{\sim}{k}_1)}{\partial t} = \iiint G\left[(N_1 + N_2)\, N_3 N_4 - (N_3 + N_4)\, N_1 N_2 \right]$$

$$\times\ \delta(\omega_1 + \omega_2 - \omega_3 - \omega_4)\ \delta(\underset{\sim}{k}_1 + \underset{\sim}{k}_2 - \underset{\sim}{k}_3 - \underset{\sim}{k}_4)\, d\underset{\sim}{k}_2\, d\underset{\sim}{k}_3\, d\underset{\sim}{k}_4 \tag{2.32}$$

where $N_i = N(\underset{\sim}{k}_i)$; $\omega_i = (gk_i)^{1/2}$ and the coupling coefficient G is a complicated function of the wave-numbers $\underset{\sim}{k}_1, \ldots, \underset{\sim}{k}_4$. Numerical computations of the six-fold integral of (2.32) were performed by

Sell and Hasselmann (1972) and used in the JONSWAP (Hasselmann et al 1973) to conclude that "most of the growth on the forward face of the wind-wave spectrum can be attributed to the nonlinear energy transfer to longer waves". Longuet-Higgins (1976) and Fox (1976) showed that the coupling coefficient G between four nearly equal wave-numbers is finite and not zero. This implies that the exchange of energy within the peak of the spectrum is of dominant importance. Extending the idea of Longuet-Higgins, Dungey and Hui (1979) have developed an almost analytical method for efficient calculation of the energy transfer rate of (2.32) which is valid for typically narrow wind-wave spectra. They substantiated the JONSWAP conclusion and showed that energy transfer due to nonlinear wave-wave interaction is important at all stages of development of a wind-wave field. This will be taken into account in later sections in analysing the observed directional spectra.

3. EXPERIMENTAL ARRANGEMENTS

3.1 Field Site

The map (figure 3.1) shows the location of the stable platform (a bottom mounted tower - figure 3.2) in the western end of Lake Ontario. During any given year, Lake Ontario sees several episodes of wind speed in excess of 15 metres per second. Its surface temperature varies from about 1°C in the late winter to about 20°C in the late summer, and, with an air temperature range more than twice as great, near surface atmospheric stabilities can take on significant non-neutral values even in moderate winds. Although the prevailing winds are westerly yielding fetches of 1.1 to 2 km, fetches of up to 300 km occur throughout the year.

As indicated in figure 3.1 (inset), the bottom slopes relatively rapidly (about 11 m/km) from the shore to the location of the tower at 12 metres depth; whereas at and beyond the tower the bottom slope is gentle (1.5 m/km). In addition, the shoreline is very straight and the bottom contours are parallel for 3 km in both directions. The simplicity of the beach geometry allows us to account for refractive effects on the longer waves approaching the beach and to quite easily deduce the deep water spectrum from the measured topography-modified one. Clearly, placing the tower in appreciably deeper water would have multiplied communications and access difficulties.

The annual variation in water level is less than 1/2 metre; tides, seiches and wind set-up change the water level by, at most, 0.1 m; there are no significant tidal or seiche currents and other less organized currents are typically less than 10 cm/s.

The computer-controlled recording equipment (Birch et al. 1976) is housed in a trailer onshore and communication between tower and trailer is by means of an underwater cable. Other cables provide up to 6 Kwatts of well regulated mains power. Having laboratory quality electrical power at the field site simplified matters to a

degree which will be apparent to anyone who has had to operate without it. About 1 Kwatt of electrical power is consumed in sensing and recording. The additional power is useful in the operation of flood lights and power tools.

At the end of June 1977, when the array of wave staffs was removed from the tower, the field site had been in virtually continuous operation for 13 months - a track record due in some degree to the proximity of the field site to our laboratory (15 minutes by boat or car) and its technical support facilities.

3.2 Array Design

At the chosen site, wave periods of up to four seconds are common with larger peak periods up to eight seconds occurring less frequently. Waves having periods in excess of four seconds and, therefore, deep-water wavelengths in excess of 25 m are modified to some degree by the bottom topography. We, therefore, designed the array for the more common 'deep-water' waves (periods less than four seconds). Barber (1963) has suggested that the dispersion relation for surface water waves be invoked to avoid the need for a two-dimensional array. We specifically chose not to follow this piece of advice in order to determine the extent to which the dispersion relation is modified by nonlinearities in the wave field. Thus the array is in the form of a cross with a maximum extent of 28 m. Since we wanted to examine the entire gravity wave spectrum, a smaller unit spacing or 'space sampling interval' would have been desirable, but cost considerations limited the number of wave staffs and hence the unit spacing to one metre. The final arrangement of 14 wave staffs optimized as described by Barber (1963) is shown in figure 3.3. The only wave staff which is less than two metres from a 41 cm diameter leg at the point where it intersects the surface, is five metres from the nearest other staff so that any reflected waves from the legs would have little effect on the correlation between the wave staffs. On the longer arm of the array, only four of the 28 possible lags are missing, while only two of the 20 on the shorter arm are missing.

This array allows us to estimate the directional spectra in the manner described by Barber (1963) or Garrett (1970) for waves having wavelengths from 2 to 28 metres. As pointed out by Cartwright in the discussion following Barber's (1963) paper, longer waves may be resolved in much the same way as discussed by Longuet-Higgins et al. (1963). That is, the various differences between wave staffs may be used to estimate spatial derivatives (tilts, curvatures ...) of the surface. Therefore, the resolving power for waves longer than 28 m depends on the highest order of derivative which may be extracted from groups of wave staffs. The first derivatives (tilts) and the surface elevation yield the first five Fourier coefficients of the angular distribution of energy at a given frequency and the wavelength corresponding to that frequency (Longuet-Higgins et al. 1963).

The array is oriented so that waves from the longest fetch directions (57 to 83 degrees true) approach the array at 45° to the arms. This maximizes the directional sensitivity of the array to the long waves using the method of Longuet-Higgins et al. (1963). If the array were oriented so that the long waves approached along the x axis for instance, then the slope of the surface in the x direction would be insensitive to small variations of the approach direction of the waves about the x axis; on the other hand, although the slope of the surface in the y direction would be maximally sensitive to wave approach direction, it would be very small and possibly lost in the noise.

Although a few occasions of long period waves did occur during the experiment, this paper deals only with waves having peak period of 4 seconds and less, i.e. deep water waves. The analysis method, described in §4.2, draws heavily on the techniques outlined by Barber (1963).

3.3 Wave Staffs

The 14 wave staffs are of the capacitance type in which the sensing element is a teflon coated wire 6 m in length. The diameter of the wire is 1.6 mm, and the overall diameter is 4.8 mm. Each wave staff is suspended from the upper deck of the tower or one of the arms by steel cable, and held in 50 Kgm tension by rubber 'shock cords' which are anchored to the bottom. The total unsupported length

is 18 m with the top support being 6 m above mean water level. This arrangement avoided additional attachment structures at mid-depth, which would interfere with the flow field of the waves. The tower itself was constructed with the minimum of cross bracing, and, in fact, is free of any between 3 m above the mean water level and 6 m below. This region is disturbed only by the presence of the four 41 cm diameter legs and a fifth smaller pole of ellipsoidal cross section at the mid point of one side of the tower (see figure 3.2). The long unsupported length of the staffs has the disadvantage that passage of a wave moves them slightly and hence affects the array configuration. The magnitude of the displacement so produced is roughly proportional to the wave length of the incident wave and less than 0.3% (about 1 degree phase error) of it for waves which are resolvable by the array.

Among the characteristics of wave staffs of most interest to us were calibration stability, linearity and speed of response. Laboratory tests were conducted in a transparent pipe in which the water level could be rapidly adjusted. Readings were made at 1 m intervals and figure 3.4 gives some idea of the linearity. The deviation from the regression line shown is nowhere greater than 0.33% (Der and Watson 1977) and the slope and intercept of the regression line changed on average by 0.7% and 21 mvolts (equivalent to 1.3 cm) respectively over four months of field exposure. These laboratory tests established the linearity and stability of the wave staffs, but the actual calibration used was determined in the field by immersing the staffs to various depths near the tower. These field calibrations did not differ, on average, from the laboratory calibrations by more than 2% in the slope and 56 mv in the intercept.

The frequency response of the electronic circuitry of the wave staffs was computed and checked by replacing the wave staff with a voltage variable capacitor driven by a sine wave generator. The amplitude response is flat to 30 H_z and the phase shift from 0 to 10 H_z was $1.2°/H_z$ with a maximum variation of 10% among the 14 staffs. Therefore, the maximum relative phase shift between staffs at frequencies below 5 H_z was less than 1°. The highest frequencies for which we can resolve directional spectra are about 1 H_z for the

field and 4 H_z for the laboratory. Much more difficult to establish is the deterioration of frequency response due to the adherence of a film of water to the staff as the water level drops rapidly. A chart recording was made of the output voltage of a wave staff while the water level was dropped in the transparent pipe at the rate of about 1 m/s and then suddenly stopped. The sharpness of the corner, between the decreasing voltage part of the trace and its final constant value, served as an indication of the degree to which the surface film affected the frequency response of the wave staff. Within the time resolution (0.2 second) of the chart recorder used, the corner showed no roundness. It would appear then that the wave staffs were capable of faithful response in the frequency band of interest (0 to 5 H_z) - at least while clean. Evidently algal growth and the accumulation of dirt on the staffs would affect the ability of the teflon to reject water. To reduce this danger, the staffs were cleaned weekly in situ with a sponge attached to a rod. As a further precaution, for each run the standard deviations of surface displacement, as indicated by each of the 14 staffs with its own field calibration, were compared with the average standard deviation and any staff which differed from the average by more than 10% was deemed to be dirty or faulty and rejected. The noise level was sufficiently low that no filtering was deemed necessary before A to D conversion. The sharp fall off of the wave spectrum reduced the importance of aliasing. The digitization step (resolution) was 1.5 mm.

At the end of the field observations, a 1/28 scaled version of the wave staff array was constructed for use in the wind-wave flume of the Canada Centre for Inland Waters (figure 3.5). In this case, the sensor was made of a single length of teflon insulated hook-up wire of 1.1 mm outside diameter. Each staff was attached to plywood disks on the top and bottom of the wind-wave flume, and held in 1-1/2 Kgm tension. Calibration of the staffs was achieved during filling and emptying of the flume. Figure 3.4 illustrates the linearity of these staffs as well as the field staffs. The same electronic packages were used in both field and laboratory. In the laboratory, there was some evidence of 60 H_z noise on some of the

wave signals. As a result, all the signals were filtered with matched 12 db/octave Bessel (linear phase shift) low-pass filters, with -3 db points set at 30 H_z. The sampling frequency was 20 H_z per channel and the maximum resolvable wave-number 28 π rad/m, which corresponds to a frequency of about 5 H_z. The total time delay between channels, caused by the Bessel filter/A to D converter system, was determined by recording a sine wave from a signal generator on all channels simultaneously. At 5 H_z the maximum phase shift between any two channels was 1°. The digitization step (resolution) was 0.4 mm. It has been demonstrated by theory and experiment (Sturm and Sorrell, 1973) that surface intersecting wave gauges effectively average over a circle of diameter much larger than that of the gauge. The effective diameter increases slowly with the gauge diameter and, extrapolating their results, would be about 7 cm for our laboratory gauges, which is the limit of wave-length resolution of our laboratory array.

3.4 Meteorological Measurements

At the tower wind speed, direction and Reynolds stress measurements were made with a Gill anemometer bivane (Gill, 1975) mounted at 11.5 m above the water. In addition, air temperature, humidity, water temperature, heat flux and evaporation were also recorded. As an indication of horizontal homogeneity a meteorological buoy was moored about 11.2 km from the tower on a bearing of 59°.

Reynolds stress measurements were not made in the laboratory during the directional spectrum experiment, but may be inferred from an earlier experiment in which an x-film anemometer was placed 26.2 cm above the mean water and at the position shown in figure 3.5.

In this paper the wind is characterized by its speed rather than the momentum transfer (or Reynolds stress) to the surface. Since a significant proportion of the stress is supported by very short waves (beyond the limits considered herein) it would seem that the wind speed itself is more useful than the friction velocity as a means of relating the wind effects on the "energy containing" gravity waves.

4. ANALYSIS METHOD

4.1 Introduction

Directional spectra are generally computed from knowledge of the behaviour of the spatial and temporal correlation function (2.20). However, although the frequency spectrum of this function may be well defined, the spatial structure will be very poorly known. Thus, the pitch-roll buoy (Longuet-Higgins et al. 1963) measures the local amplitude and slope of ρ ($\underset{\sim}{r}$, t) near $\underset{\sim}{r}$ = 0. An array of N wave staffs can yield at the most N(N-1)/2 + 1 independent point observations of ρ ($\underset{\sim}{r}$, t) and, as will become evident, this will not be enough to enable direct estimates of the spectral energy density to be obtained at all the required points. Thus, in particular, we have 14 wave staffs (figure 3.3) yielding (allowing for duplicates) 165 possible spatial points at which $\rho(\underset{\sim}{r}, t)$ may be determined; whereas the possible resolution is such that we would like knowledge of the spectrum at 2337 locations (§4.2).

Thus, in practice, it is necessary to make assumptions about the location and form of the directional energy spectrum in order to reduce the number of degrees of freedom of the spectrum description to less than the number of pieces of available information. The various methods proposed for evaluating directional spectra may thus be characterized by the objectivity and flexibility of these assumptions.

The first practical directional spectra were obtained from a pitch-roll buoy (Longuet-Higgins et al. 1963). The important assumption that the linear dispersion relation $\omega^2 = gk$ was satisfied, enabled the (directional) wave spectrum to be expressed in the form

$$X(\underset{\sim}{k}, \omega) = \delta(|\underset{\sim}{k}| - \omega^2/g)\,[a_0 + a_1 \cos\theta + b_1 \sin\theta + a_2 \cos 2\theta + b_2 \sin 2\theta]$$

where a_0, a_1, b_1, a_2 and b_2 are real quantities determined by the analysis and θ is the polar angle of the wave-number $\underset{\sim}{k}$.

Subsequently, the "cloverleaf" buoy was developed (Cartwright and Smith 1964, Ewing 1969) enabling the polar distribution to be calculated including terms up to cos 4θ and sin 4θ, still however with the same assumption regarding the distribution of $X(\underset{\sim}{k}, \omega)$ with $|\underset{\sim}{k}|$.

The method utilized in the present analysis is based initially on the theoretical work of Barber (1963) who described the manner of obtaining a full three-dimensional (or wave-number frequency) spectrum $X(k_x, k_y, \omega)$ from an array of wave staffs. The spectrum, however, is masked by the sampling window W (or transfer function) of the array

$$X_{obs}(k_x, k_y, \omega) = \iint X(k_x - \ell, k_y - m, \omega)\, W(\ell, m)\, d\ell\, dm$$

This window will generally be extremely confusing (e.g., see figure 4.2) and the information content (degrees of freedom) will still be limited by the number of available staff separations as indicated above. Nevertheless, this procedure was implemented by Garrett (1970) with an array of nine wave staffs, but little quantitative information could be obtained because of the masking window and the limited number of wave staffs used. The method which we have adopted is an extension of the work of Garrett (1970) with post processing of the masked Barber spectrum to obtain the underlying true spectrum. The method adopted for obtaining the true spectrum (described in detail below §4.2) with the restricted information available is to choose objectively, by computer algorithm, the locations at which directional energy is observed to be. The amplitude of the spectral energy density is then obtained by a least squares fit to the observed masked wave-number spectrum. A consequence of this method is that confidence limits for the estimates arise naturally from the fitting process.

Since this method was finalized, a number of papers have been published suggesting methods of analyzing wave staff records to obtain directional spectra. For example, Davis and Regier (1977) include an extensive discussion of the criteria for array and processing design. However, the main thrust of their argument seems

to be obtaining optimal results from relatively sparse data. Comparatively little attention was paid therefore to computational efficiency and in their companion paper (Regier and Davis, 1977) they consider only two-dimensional spectra (satisfying the linear dispersion relationship) obtained from an array of six wave staffs. Borgman (1979) proposes both an iterative and a least squares approach to establishing the polar distribution which is similar in approach to that adopted here in the sense that by identifying the location of the energy an improved representation of the distribution can be obtained. However, no attempt is made to suggest methods of either estimating the dependence of X on $|\underset{\sim}{k}|$ or of obtaining confidence limits from the estimates obtained. Rikiishi (1978) proposes a direct method for analyzing two-dimensional spectra and considers the case $\omega^2 = \alpha g\,|\underset{\sim}{k}|$. Although his method appears to rely on a correct choice of α, he proposes a test (the detection of wave energy in the opposite quadrant from the major energy concentration) which 'might' enable α to be determined iteratively. However, this procedure does not allow for the possibility of energy being located at both $|\underset{\sim}{k}| = \omega^2/g$ and $|\underset{\sim}{k}| = 1/2\,\omega^2/g$ as would be expected for a Stokes wave.

To summarize, the method adopted for obtaining estimates of the directional spectra (described below) seems to compare well with other methods suggested both before and since its conception. Its advantages are:

(i) the lack of an assumption about the location and distribution of directional energy, particularly with respect to $|\underset{\sim}{k}|$.

(ii) the availability of confidence limits for the estimates.

4.2 The Modified Barber Method

All methods of obtaining directional spectra rely on the important relation (2.21) We first carry out the time Fourier transform of (2.21) to get the wave-number spectrum $\underset{\sim}{X}(k, \omega_0)$ at a given frequency ω_0. For simplicity, we will drop the reference to a fixed frequency ω_0 in the following. Thus $X(\underset{\sim}{k})$ means $X(\underset{\sim}{k}, \omega_0)$.

$$X(\underset{\sim}{k}) = (2\pi)^{-2} \iint \rho(\underset{\sim}{r})\, e^{-i\,\underset{\sim}{k}.\underset{\sim}{r}}\, d^2\underset{\sim}{r} \tag{4.1}$$

Following Barber we now introduce the assumption that the wave field is invariant with respect to placement in (x, y) space, provided that the length T of the time average is sufficiently long. Thus two wave staffs placed at $\underline{R}_i$ and $\underline{R}_j$ will provide an estimate for

$$\rho(\underset{\sim}{R}_i - \underset{\sim}{R}_j) = \rho^*(\underset{\sim}{R}_j - \underset{\sim}{R}_i)$$

by means of the formula (Barber 1963):

$$\rho^{ij} \equiv \rho(\underset{\sim}{R}_i - \underset{\sim}{R}_j) = \frac{a^i\, a^{j*}}{T^2} \tag{4.2}$$

where a_i is the Fourier transform

$$a^i = \int_0^T \zeta(\underset{\sim}{R}_i, t)\, e^{-i\omega t}\, dt \tag{4.3}$$

Using these estimates (4.2) for ρ in (4.1), we obtain the observed or raw Barber wave-number spectrum.

$$\xi(\underset{\sim}{k}) = \sum_{\ell} \overline{\rho}(\underset{\sim}{r}_{\ell}) \exp(-i\,\underset{\sim}{k}.\underset{\sim}{r}_{\ell}) \tag{4.4}$$

where the $\underset{\sim}{r}_{\ell}$ are the separations $\underset{\sim}{R}_i - \underset{\sim}{R}_j$, ρ is known and $\overline{\rho}(\underset{\sim}{r}_{\ell})$ is the average of all the estimates ρ^{ij} for ρ at the point

$$\underset{\sim}{r}_{\ell} = \underset{\sim}{R}_i - \underset{\sim}{R}_j$$

In figure 4.1 is plotted a contour map of a typical $\xi(\underset{\sim}{k})$. Note

(i) that negative values occur (this is unphysical)

(ii) $\xi(\underset{\sim}{k})$ is periodic outside the region

$$-\pi < k_x < \pi$$

$$-\pi < k_y < \pi$$

where k_x is the x component of $\underset{\sim}{k}$ and k_y the y component. This is because the 14 wave staffs are separated by multiples of one metre in the x and y directions. Thus replacing $\underset{\sim}{k}$ by $\underset{\sim}{k} + 2\pi \underset{\sim}{i}$ or $\underset{\sim}{k} + 2\pi \underset{\sim}{j}$ in the wave-number spectrum does not effect the observed ρ^{ij}.

(iii) there is energy outside the circles $k = \omega^2/g$ corresponding to the frequency limits ω_1, ω_2 of the band being considered.

Now as indicated above, the distortion introduced by the incomplete information for $\overline{\rho}(\underset{\sim}{r}_\ell)$ (the 14 wave staffs yield only 165 independent correlations) can be represented by means of a masking function M

$$\xi(\underset{\sim}{k}) = \iint X(\underset{\sim}{k}_1)\, M(\underset{\sim}{k} - \underset{\sim}{k}_1)\, d^2\underset{\sim}{k}_1 \tag{4.5}$$

where

$$M(\underset{\sim}{k}) = \sum_\ell \exp(-i\, \underset{\sim}{k}.\underset{\sim}{r}_\ell) \tag{4.6}$$

In figure 4.2 will be found a contour map of the masking function (by definition $M(\underset{\sim}{k})$ is real). It will be noticed that: there are negative areas explaining the negative areas in the raw spectrum; the prominence of the two bands along the k_x and k_y axis (related to the arrangement of the wave staffs along orthogonal axes); the value of $M(\underset{\sim}{k})$ at $\underset{\sim}{k} = 0$ is larger than values elsewhere; and finally the resolution is $O(\pi/x_{max})$ and $O(\pi/y_{max})$ in the x and y

directions were x_{max} and y_{max} are the maximum separations of the wave staffs in the x and y directions respectively.

With the aid of figure 4.2, the raw wave-number spectrum (figure 4.1) can be roughly interpreted and this is the procedure adopted by Garrett (1970) (however with fewer wave staffs). This is not an acceptable procedure however if any systematic analysis is to be done. It is therefore necessary to invert (4.5) to obtain $X(\underset{\sim}{k})$ directly.

The method adopted was to assume that $X(\underset{\sim}{k})$ took the form

$$X(\underset{\sim}{k}) = \sum_{m=1}^{M} E_m \, \delta(\underset{\sim}{k} - \underset{\sim}{k}_m) \tag{4.7}$$

where the $\underset{\sim}{k}_m$ are a set of locations ($m < 165$) chosen using the algorithm described in the appendix. The E_m are chosen on the basis of a least squares fit to the observed wave-number spectrum.

$$\frac{\partial}{\partial E_m} \left\{ \iint_D \left[\xi(\underset{\sim}{k}) - \sum_{m=1}^{M} E_m \iint \delta(\underset{\sim}{k} - \underset{\sim}{k}_m) \, M(\underset{\sim}{k} - \underset{\sim}{k}_1) \, d^2 \underset{\sim}{k}_1 \right]^2 d^2 \underset{\sim}{k} \right\} = 0 \tag{4.8}$$

in the region

D: $-\pi < k_x, k_y < \pi$

The cross products such as $\overline{M(\underset{\sim}{k} - \underset{\sim}{k}_1) \, M(\underset{\sim}{k} - \underset{\sim}{k}_0)}$ (4.9)

whose calculation is normally required by a least squares fit, would prove lengthy. However, as shown in the appendix, the calculation can be considerably simplified, and the least squares fit reduced to the set of formulae

$$\xi(\underset{\sim}{k}_\ell) = \sum_{m=1}^{M} E_m M(\underset{\sim}{k}_\ell - \underset{\sim}{k}_m) \tag{4.10}$$

$$\ell = 1, 2 \ldots M$$

these being merely the requirement that the residual be zero at the chosen locations $\underset{\sim}{k}_\ell$. Further details and the method of estimating the sensitivity of the inversion may also be found in the appendix.

In figure 4.3 is graphed the result of inverting the raw wave-number spectrum of figure 4.1, 32 points were used for the inversion and they explained 96% of the variance. Typical estimates for the standard deviations of the inverted spectrum amount to 10% of the peak height. Note that the algorithm for choosing the location $\underset{\sim}{k}_m$ is not biased towards any particular region, therefore the compactness of the $\underset{\sim}{k}_m$ and the general confinement within the linear dispersion bounds, illustrate the power of the method.

The steps in this process of recovering the detected wave-number spectrum $X(\underset{\sim}{k})$ from the raw (or observed) spectrum $\xi(\underset{\sim}{k})$ are illustrated in the composite figure 4.4. This figure was produced by analysing simulated surface elevation time series corresponding to a monochromatic infinite crested wave train travelling along the y axis in deliberate and flagrant disregard of the dispersion relation (1.1). Such data should yield delta functions in both frequency and wave-number space. Figure 4.4 shows the frequency spectrum, the raw (observed) wave-number spectrum, the array transfer function and the detected wave-number spectrum. It can be seen that the raw wave-number spectrum looks rather like the array transfer function but displaced from the origin along the y axis. In fact, the raw spectrum is a convolution of the single delta function wave-number spectrum with the array transfer function. The inversion process recovers the delta function (within grid resolution) and accounts for 99.88% of the energy in the prescribed spectrum.

Note that the wave-number spectrum whatever its shape is always represented by a set of delta functions. These delta functions may not be located arbitrarily but must be at one of a cartesian array of points

$$\underset{\sim}{k}_m = r\, dk_x \underset{\sim}{i} + s\, dk_y \underset{\sim}{j} \tag{4.11}$$

where r,s are integers and

$$dk_x = \frac{2\pi}{(2 \times 20 + 1)} ; \; dk_y = \frac{2\pi}{(2 \times 28 + 1)} \; m^{-1}$$

the maximum staff separations in the x and y directions being 20 and 28 metres respectively (figure 3.3). Hence, energy at sub grid spacings will be analyzed imperfectly by the inversion method. In figure 4.5 may be found the result of analyzing a simulated delta function wave-number spectrum with the delta function placed halfway between the nodes (4.11). In this case, the detected energy is spread principally to the four surrounding grid points. It will be seen that, although the peak is wider, the analyzed wave-number spectrum is still reasonably compact and positive definite (94.6% of the variance was explained by the analysis).

Finally in the region D there are 2337 locations $\underset{\sim}{k}_m$ and only a maximum of 165 possible correlations for the analysis to use. This is not a problem for the lower frequencies when the expected wave-number is small, however, for the higher frequencies it is necessary to consider, instead of delta functions, weighted collections of delta functions

$$\tilde{\delta}_m = \sum_i w_i \, \delta \, (\underset{\sim}{k} - \underset{\sim}{k}_1) \tag{4.12}$$

at restricted sets of locations $\underset{\sim}{k}$ (see the appendix for details). This reduces the number of free parameters necessary in the least squares fit and hence decreases the sensitivity of the fit and

increases the possible area covered. Delta functions have been used in preference to pyramidal or obloid functions because of the increased resolution available with the former. Also the implied smoothing outlined above can be justified on theoretical as well as empirical grounds as follows.

For the higher frequencies the correlations obtained at large separations $\underset{\sim}{r}_\ell$ will be less significant than those at small. Therefore, in the manner of Hamilton, Hui and Donelan (1979), to obtain a best fit raw wave-number spectrum, we should weight the larger separations less than the smaller i.e.

$$\xi(\underset{\sim}{k}) = \sum w(|\underset{\sim}{r}_\ell|)\, \overline{p}(\underset{\sim}{r}_\ell) \exp(-i\underset{\sim}{k}.\underset{\sim}{r}_\ell) \tag{4.13}$$

where $w(|\underset{\sim}{r}_\ell|)$ are the weights decreasing with increasing $\underset{\sim}{r}_\ell$. This weighting is known to be equivalent to smoothing $\xi(\underset{\sim}{k})$ hence less resolution will be available in fact and (4.12) is justified.

The method of analyzing the wave recordings adopted here produces compact wave-number spectra which should not be systematically distorted by the array geometry and error estimates which will be a function of the orientation. The error estimates are available from the least squares fit as standard deviations on the point estimates E_m (see the appendix).

4.3 Some Sources of Error

A further potential source of error (aside from the limitations of the analysis method) is the placement of the wave staffs. The wave staffs were designed to be placed at locations which were separated in the x and y directions by exact multiples of 1 metre. This length determines the Nyquist limit ($\pm\pi$ m^{-1}) of the array. On recovering the staffs, their locations were checked and some significant errors were detected. The designed and actual coordinates may be found listed in table 4.1.

TABLE 4.1

	x coordinates		y coordinates	
Staff	Design	Actual	Design	Actual
1	15	15.2	0	0.0
2	14	14.2	0	0.0
3	10	10.2	0	0.0
4	3	3.0	0	0.0
5	0	0.0	0	0.0
6	-3	-3.0	0	0.0
7	-5	-5.0	0	0.0
8	0	0.0	-15	-15.16
9	0	0.0	-14	-14.13
10	0	0.0	-11	-11.13
11	0	0.0	- 5	- 5.03
12	0	0.0	6	5.97
13	0	0.0	11	11.11
14	0	0.0	13	13.11

We were able to test the effect of these misplaced staffs by simulating a wave whose wave-number spectrum was a delta function at a location corresponding to a data point in the detected wave-number spectrum. Thus for the designed staff locations, the correlation $c(\underset{\sim}{k}_0)$ between the transfer function (located at this wave-number) and the observed wave-number spectrum $\Psi^0(\underset{\sim}{k})$

$$c(\underset{\sim}{k}_0) = M(\underset{\sim}{k} - \underset{\sim}{k}_0)\, \Psi^0(\underset{\sim}{k}) \,/\, \{ \overline{[M(\underset{\sim}{k})\, \Psi^0(\underset{\sim}{k})]^2} \}^{1/2}$$

would be 1.00. We observed the following values.

TABLE 4.2

n	$\underset{\sim}{k}_0 = nd\underset{\sim}{k}_y \underset{\sim}{j}$	$c(\underset{\sim}{k}_0)$
3	0.352	0.999
6	0.660	0.995
9	0.993	0.988
18	2.01	0.95
27	2.95	0.89

Since the analysis is stopped after 92% of the variance is explained, it can be seen that the staff placement errors must be a source of error at wave-numbers of 2.5 m^{-1} and higher. The error applies only to the field data.

5. SUMMARY OF DATA

The field experiment was designed to gather sufficient data to describe the directional spectrum of wind-generated waves under a variety of natural conditions. A suitably nondimensionalized description of the directional spectrum might be expected to be sensitive to nondimensional numbers descriptive of the general water-air interfacial conditions. It is difficult to conceive of a wind-wave generating process which is unaffected by the relative speeds of wind and waves; thus the parameter U/c, relating wind speed to wave phase speed, was regarded as the primary 'sorting' variable in classifying a population of wind-generated wave spectra. Inasmuch as the wind profile and the intensity of turbulence (hence the pressure fluctuation spectrum) play an important role in the wind-wave coupling problem and are strongly affected by the stability of the atmospheric surface layer, it would seem that a suitable nondimensional index of stability would be an additional parameter against which to examine the behaviour of the directional spectra. In this paper, we use the bulk Richardson, R_b as a convenient measure of atmospheric stability.

$$R_b = \frac{Zg\,(T_a - T_w)}{(237 + T_a)\,U^2}$$

where U and T_a are wind speed and air temperature evaluated at height Z; T_w is the water surface temperature. Finally, the degree of nonlinearity, the tendency towards whitecapping (instability) and the strength of wind-wave coupling are all, to some extent, reflected in the wave slope S.

We have chosen to classify the data in terms of the atmospheric stability R_b, an average wave slope S and the parameter U/c, relating wind and wave speeds. Other nondimensional parameters may be constructed from the variables of the overall flow and

geometry, but they are either virtually constant throughout our measurements or unlikely to influence that part of the directional spectrum which is accessible to our observational and computational arrangements.

Clearly, the establishment of the behaviour of the directional spectrum in the three-parameter space defined above would require a large number of measurements of the directional spectra. This led to the design of wholly automatic digital data logging for the field site. However, since each directional spectrum would be calculated from time series of 14 wave staffs sampled at 5 Hertz for 14 to 60 minutes, some preselection of recording times would be required to limit the collected data to a manageable quantity. Our approach was to use a mini-computer to control the data logging and to decide when to gather data suitable for the computation of directional spectra. The details of the data logging system are described by Birch et al. (1976), but a brief summary of the relevant aspects is warranted here. From May 1976 to July 1977, the field site was in nearly continuous operation. During most of that time, recordings were made of one-minute averages of wind speed and direction, air temperature and humidity, water temperature and currents, and mean square wave height. These averges were computed by the mini-computer using the raw data sampled at 5 Hertz. In addition, the fluxes of momentum, heat and moisture, and other cross products of the atmospheric turbulent fluctuations, were accumulated over 20 minutes and recorded. In this way, a continuous record was kept of mean parameters and fluxes of the air-water interface. Every ten minutes the average wind speed and air temperature over the previous ten minutes were computed and, if they differed by a preset amount from stored reference values, samples, taken five times a second sequentially from each of the channels mentioned above and all 14 wave staffs, were directly recorded for later processing. This mode of recording of the instantaneous time series for later spectral analysis, continued for one hour, after which the system returned to its normal mode of data logging of the one-minute averages. Ten

minutes after this, the reference wind speed and air temperature were updated, and the search for a further change in the wind speed or air temperature continued. It can be seen that this simple method would reduce the collection of raw data during peiods of steady winds, thereby avoiding repeated realizations of the wave field under very similar overall conditions. By the same token there was, of course, a bias towards changing conditions, but not an overwhelming one since it was not the rate of change of the wind speed or air temperature which initiated the 'fast' mode but rather the change itself which may have occurred over an hour or several days.

The net product of this scheme was a series of hour-long time series recordings over a wide range of the three parameters of interest. In this paper we are concerned with characteristics of the directional spectrum at steady state. There were 84 runs analyzed and the overall conditions prevailing during these runs are summarized in the histograms of figures 5.1, 5.2 and 5.3. The runs are grouped into arbitrary classes of the 'whole spectrum equivalent' values of the three parametrs U/c, R_b and S. That is, U/c is referenced to the peak of the spectrum and the wind at 10 metres height U_{10}/c_p and S is the "significant slope" as defined by Huang et al. (1981).

There were seven laboratory runs and these are separately listed in table 5.1 with the values of U_{10}/c_p, S and R_b also shown. The range of R_b for these cases is small as the wind-wave flume is not equipped with temperature controls of air or water.

TABLE 5.1. SUMMARY OF LABORATORY DATA

Symbol	V+	U	ω_p	$\overline{\zeta^2}$	U/c_p	S	R_b
Units	m/s	m/s	rad/s	cm^2		%	
Height (m)	0.26	10			10		0.26
Fetch (m)	49.8	49.8	53.5	53.5	53.5	53.5	49.8
Run							
2	3.29	4.58	15.0	0.19	7.5	1.6	+0.011
3	4.80	6.86	11.5	0.55	8.5	1.6	+0.004
5	7.79	11.94	9.0	3.37	11.8	2.4	+0.001
6	9.46	15.40	8.4	5.54	14.0	2.7	+0.001
7	10.87	18.83	7.7	9.56	15.9	3.0	+0.001
29	3.24	4.49	14.9	0.19	7.2	1.6	+0.007
30	12.00	21.88	7.0	20.08	16.5	3.6	+0.001

+ V is the measured wind speed

6. TYPICAL DIRECTIONAL SPECTRA

6.1 Field Wave-Number Frequency Spectra

In this section, we present and discuss some representative wave-number spectra calculated from wind-wave data recorded in Lake Ontario during 1976-1977. In all these calculations, the wave fields are assumed to be stationary and homogeneous.

In each of the two cases to be presented (figures 6.1 and 6.2), we show a frequency spectrum and a sequence of wave-number spectra $X(\underset{\sim}{k})$ for a frequency band $\Delta\omega$ as plots in the wave-number space $\underset{\sim}{k}$ at various frequencies. In these plots, the solid circles represent the limits of the deep-water dispersion relation (1.1) for infinitesimal waves corresponding to the limits of the frequency bands analyzed, whereas the broken circle corresponds to the (energy) centroidal frequency of the band.

All the waves analysed have wave lengths of the dominant wave less than twice the water depth at the tower (i.e. less than 24 m) hence, finite depth effects on the dispersion relation are negligible. Within the resolution of these contour plots, higher harmonics of the dominant waves are not observed, but they are observed in the laboratory experiments as will be seen below.

In figure 6.1 near the peak frequency, the energy is very concentrated and lies between the two-solid circles, indicating that the linear-dispersion relation (1.1) is obeyed for these waves which are near full development, $U/c_p = 1.5$. At higher frequencies, the energy density appears slightly inside the inner solid circle. This could be due to the local Stokes effects of finite-wave slope. As discussed in §2, such effects can cause a departure from the linear dispersion circle by up to about 20%. Figure 6.2, on the other hand, corresponds to younger waves ($U/c_p = 3.1$) i.e. stronger wind generation near the peak frequency. It can be seen that in this case there is evidence of amplitude (finite slope) dispersion just above the peak as well as at higher frequencies.

In a few cases (e.g. figure 6.3), it was observed that the energy density lies outside the larger-dispersion circle. This may be explained by the presence of forced waves according to the theory in §2. Actually, one should expect forced waves to be present much more regularly than the directional spectra show. We attribute this scarcity of evidence of forced waves in the directional spectrum to intermittency of the generation process. It was shown in §2 that on removal of the forcing, forced waves instantaneously revert to free waves of the same wave length but with a sudden shift in the phase, and hence, since the spectra represent averages over time, the free waves should (as observed) predominate in the spectra.

6.2 Laboratory Wave-Number Frequency Spectra

Wave data were also recorded in the wind-wave flume at CCIW using a 1/28th scale array of wave records in the same configuration as the tower. In no case was the wavelength of the waves at the spectral peak more than 1.15 times the water depth (1.1 m). Therefore, as for the field data, these laboratory waves are deep water waves. Wave-number spectra for a typical case (run no. 5) are shown in figure 6.4 at various frequencies. The frequency spectrum is narrow and the general features of the wave-number spectra resemble those in the lake with some very significant differences. Thus, for instance, whilst at the peak frequency (ω_p = 8.96) the wave energy is nearly on the linear-dispersion circle, for higher frequencies, the energy appears progressively inside the circle. As we will describe in detail in §10, this is a reflection first of amplitude dispersion and then, at $\omega/\omega_p > 1.8$, of the appearance of bound harmonics. In these plots the lowest positive contour is 12.5% of the peak so that the relatively small free energy cannot be seen in (e) and (f). The coexistence of free and bound energy is seen clearly in (d).

7. POLAR ANALYSIS

7.1 Introduction

In §4 and the appendix, we described how it is possible to obtain a representation of the three-dimensional directional-energy spectrum in the form

$$X(\underset{\sim}{k}) = \sum_{m=1}^{M} E_m \left\{ \sum_{\ell=1}^{L} W_\ell \, \delta(\underset{\sim}{k} - \underset{\sim}{k}_m - d\underset{\sim}{k}_\ell) \right\} \tag{7.1}$$

where

$$\sum_{\ell=1}^{L} W_\ell = 1, \quad (1 < L, M < 165) \tag{7.2}$$

and the $d\underset{\sim}{k}_\ell$ are vectors pointing to grid points clustered around $d\underset{\sim}{k}_\ell = 0$. For many purposes, (7.1) can be summarized adequately in the polar representation (2.25).

Because of the presence of noise at high wave-numbers in $X(\underset{\sim}{k},\omega)$, we cannot integrate over the entire range of k as implied by (2.25). Instead we make use of the fact that the energy in any frequency band clusters around a relatively narrow band of wave-numbers and proceed as follows:

(i) If Δ is the width of the band associated with the corresponding frequency bandwith $d\omega$

$$\Delta \approx \frac{\omega d\omega}{\pi g} \tag{7.3}$$

then we set all values of E_m to zero which do not satisfy

$$\left| \, |\underset{\sim}{k}_m| - k^* \, \right| \leq 2\Delta \tag{7.4}$$

where k^* is the radius of the wave-number circle through the $\underset{\sim}{k}_m$ with maximum associated energy. This procedure is necessary to stabilize estimates for the mean wave-number $\overline{k}(\theta)$ as described below.

(ii) We assume that fitting erros in E_1, E_2 are all perfectly correlated so that if

$$E_3 = E_1 + E_2$$

then

$$\sigma_3 = \sigma_1 + \sigma_2$$

where σ_1, σ_2, σ_3 are the standard deviations of the errors.

(iii) We then project the energy density E_m (positive values only) and the zeroth and first moments of the energy weighted by the standard-deviation estimates σ_m (say) obtained from the fitting procedure

$$M_{0_m} = \sigma_m E_m M_{1_m} = \sigma_m |\underset{\sim}{k}_m| E_m$$

on to a wave-number circle to obtain $F(\omega,\theta)$, $M_0(\theta)$ and $M_1(\theta)$.

(iv) These quantities are then binomially smoothed until the half-height width of the influence of a single E_m just exceeds 20°.

(v) The mean wave-number can then be obtained from

$$\overline{k}(\theta) = M_1(\theta)/M_0(\theta) \tag{7.5}$$

$F(\omega,\theta)$ and $\overline{k}(\theta)$ are the two main quantities of interest, and may be found presented in figure 7.1. Also plotted are estimates of the standard deviation of $F(\omega,\theta)$ (obtained in the same manner as the $F(\omega,\theta)$ were obtained but using σ_m instead of E_m) and similar graphs calculated using any negative values which may be present. These latter represent an independent estimate of the errors. We have the further check that the total positive energy resolved should be close to the energy content in the frequency band.

7.2 Parametric Representation

Since the frequency spectrum $\Phi(\omega)$ is most easily obtained, it is customary to represent the directional-frequency spectrum by:

$$F(\omega,\theta) = \Phi(\omega).\ h(\theta) \tag{7.6}$$

It follows from (2.26) and (2.30) that

$$\int_{-\pi}^{\pi} h(\theta)\, d\theta = 1 \tag{7.7}$$

The method of analysis adopted yields compact polar distributions of the energy. Therefore, it is preferable that the representations adopted for $h(\theta)$ retain this quality. Previous representations, notably the $\cos^{2s}(\theta/2)$ of Mitsuyasu et al. (1975) and later Hasselmann et al. (1980), were designed to represent directional spectra obtained in the form of a limited number of Fourier coefficients. These distributions are therefore not compact. In addition, double peaked distributions of $h(\theta)$ were occasionally observed (there are theoretical grounds for expecting double peaks, see §2). In these cases, $\cos^{2s}(\theta/2)$ would, of course, be totally inappropriate. In figure 7.2 will be found a typical polar

distribution with $\cos^{2s}(\theta/2)$ distributions superimposed. Also shown is the distribution described in §11. The polar representations of Mitsuyasu et al. (1975) and Hasselmann et al. (1980), both deduced from buoys, appear to broaden too quickly with increasing ω/ω_p. Possible reasons for this are discussed in §11.

A simple similarity argument is advanced here as the basis for a parametric representation of the polar directional distribution.

We consider only the high frequency side of the spectrum for which $U/c > 1$ and active generation is taking place. We also neglect any Stokes effect (a function of ω/ω_p where ω_p is the peak frequency) and nonlinear wave-wave interaction. Thus the energy balance is between the wave generation mechanism and the energy dissipation, related to the limited-wave slope.

$$\mu\ F(\omega,\theta) = D\ (\omega,\theta) \tag{7.8}$$

where μ is the fractional energy input rate due to the wind and D is the dissipation. We take μ to have a θ dependence given by Miles' (1957) theory

$$\mu \sim \left[\frac{U_{zz}}{U_z} \right]_{z=z_c} \tag{7.9}$$

where z is the vertical coordinate, U the wind velocity and z_c the height at which

$$U\ (z_c) \cos\theta = c \tag{7.10}$$

thus assuming

$$U(z) = \frac{u_*}{0.41}\ \ell n\ \left(\frac{z}{z_0} \right) \tag{7.11}$$

we have

$$\mu \sim \exp\left[\frac{-0.41\ c}{u_* \cos\theta}\right] \tag{7.12}$$

For the dissipation we assume that D is a function of the local energy density $F(\omega,\theta)$ and the speed difference in the direction of the waves at some height A.

$$U(A)\cos\theta - c(\omega) \tag{7.13}$$

Thus, from dimensional arguments, we have

$$D \sim F^{4/5}\ (U(A)\cos\theta - c)^{4/5} \tag{7.14}$$

and hence from (7.6)

$$F \sim (\cos\theta - \cos\theta_A)^4 \exp^{+5\ \ell n\ (A/z_0)\ \cos\theta_A/\cos\theta} \tag{7.15}$$

where θ_A is the half width and satisfies

$$U(A)\cos\theta_A = c \tag{7.16}$$

Note that the influence of g, the acceleration due to gravity on D is neglected since we assume that its effect is limited to specifying the total mean slope.

These arguments might seem reasonable, however the overriding physical objection to (7.12) is that it results in an unstable balance of energy and dissipation; increasing F lowers the dissipation relative to the generation.

Nevertheless, we still expect the spectral width to be governed by formulae such as (7.15) which provides an excellent family of curves of the type characteristic of observed and theoretical

directional spectra. That is, (7.15) may take on the bell shape of various observed cosine distributions or the double peak which has been suggested by Phillips (1957) on theoretical grounds and a variety of other symmetrical shapes. We have therefore fitted the observed $h(\theta)$ with functions $f(\theta)$ of the form

$$f(\theta) = A_0 \frac{(\cos(\theta - \bar{\theta}) - \cos\theta_A)^4}{(1 - \cos_A)^4} \exp^{+5L \cos\theta_A (1/\cos(\theta - \bar{\theta}) - 1)} \tag{7.17}$$

where the four parameters A_0, $\bar{\theta}$, θ_A, L (= $\ln A/z_0$) are chosen so as to minimize the "unconfidence" $\mathcal{U}$ where

$$\mathcal{U}(A_0, \bar{\theta}, \theta_A, L) = \int_{-M}^{M} \left[\frac{h(\theta) - f(\theta)}{\sigma(\theta)} \right]^2 d\theta \tag{7.18}$$

and $\sigma(\theta)$ is the standard deviation of $h(\theta)$ calculated as above. In figure 7.1 will also be found the distribution fitted from the family $f(\theta)$. An example of a double peaked $h(\theta)$ and corresponding fit may be found in figure 7.3.

The presence or otherwise of a double peak in the spectrum depends both on the parameter L and the width θ_A. Thus zero gradients of the shape functions occur at $\theta = 0°$ and

$$\frac{\cos\theta}{\cos\theta_A} = \frac{2L}{L^*} \left(1 \pm \sqrt{1 - \frac{L^*}{L}} \right) \tag{7.19}$$

where $L^* = 16/5$ is a critical value for L such that if $L < L^*$ no additional roots other than $\theta = 0$, occur whatever the value of θ_A. For $L > L^*$ the number of zeros depends exclusively on the width θ_A. For θ_A close to 90° two pairs of zeros will occur and there will be a triple peaked distribution. For θ_A in an intermediate range only

twin peaks will occur, and for θ_A even smaller only a single peak will be possible. In figure 7.4 will be found a plot of the various regions in the L, θ_A representation with examples of typical spectral shapes. It can be seen that this representation gives a considerable degree of flexibility in the polar distributions available for fitting to the experimental data.

8. THE FREQUENCY SPECTRUM

In this section we examine certain characteristics of the frequency spectrum. We restrict our attention to cases in which there was no swell. In fact, Lake Ontario is smaller than typical meteorological systems and the wave spectra are usually uni-modal with little or no evidence of swell.

Figure 8.1 illustrates the distribution of the data sets on a plot of r.m.s. wave height versus peak period in which it can be seen that the laboratory and field data are nearly contiguous in this sense. It is worth noting that the directional spectra were derived from 14 wave staffs, while the frequency spectrum for each case is an average of the 14 individual spectra from the separate staffs.

Kitaigorodskii's (1962) similarity argument on the scaling of fetch-limited spectra has provided the basis for a consistent description of several sets of field observations and tank experiments (Pierson and Moskowitz 1964, Mitsuyasu 1968a, 1969, Liu 1971, Hasselmann et al. 1973, Ramamonjiarisoa, 1973). The success of Kitaigorodskii's scaling law is strong support for the concept of the similarity of fetch development of the wind-generated gravity wave spectrum, which can be completely described by a length scale associated with the fetch, and a velocity scale associated with the source of energy - the wind. Such a description, however, is limited in its practical usefulness to situations in which the fetch is known and the wind is relatively constant along the fetch. In the general case of winds variable in speed and direction, a description of the parameters of the spectrum in terms of local conditions would be very valuable. Therefore, instead of the non-dimensional fetch $\tilde{x} = xg/U^2$, we have chosen to relate the spectral parameters to U_c/c_p, the ratio of the component of the 10 m wind speed in the direction of the waves at the peak of the spectrum to the phase speed of those waves.

In figure 8.2 we have collapsed the frequency spectra for all the cases on to axes normalized by the magnitude of the peak

spectral density and of the peak frequency. The spectra have been grouped into classes by the parameter U_c/c_p. The standard errors of the mean, in each band of width 0.1, are indicated at the top of the figure. The position of the vertical bar indicates the average value of ω/ω_p in each band. It appears that there is a pronounced narrowing of the spectra with increasing U_c/c_p. The smooth variation in width and otherwise smooth variation of the spectra support the idea that wind-generated spectra may be described using a similarity framework such as proposed by Kitaigorodskii (1962) and applied with dramatic effect by Hasselmann et al. (1973).

8.1 The Rear Face

It is generally agreed that wind-wave spectra have a very sharp cut-off at frequencies below the peak, i.e., on the forward face, and a somewhat more gently sloped rear face. Current practice in describing wind-wave spectra owes its origin to the pioneering work of Phillips (1958). He argued that the shorter waves on the rear face of the spectrum are limited in amplitude largely through breaking of their steepest members. Phillips' argument, based on dimensional considerations, suggests that the energy density of the rear face of the spectrum should be inversely proportional to frequency to the fifth power - the so-called ω^{-5} power law. He further argued that, although the wave energy in a wind-wave field may grow with time or down fetch, the growth should be largely by the development of the longer waves below the peak without much change to the shorter waves. That is, the rear face of the spectrum could be described by $\alpha\omega^{-5}$, where α is a universal constant. The first attempts to test Phillips' hypothesis (e.g. Burling 1959, Kinsman 1960) supported the idea of an "equilibrium range" on the rear face of the spectrum with an ω^{-5} behaviour. More recently, however, both the constancy of α and the ω^{-5} frequency dependence have been called into question (Longuet-Higgins 1969, Hasselmann et al. 1973, Misuyasu et al. 1975, Garrett 1969, Ramamonjiarisoa 1973, Toba 1973, Kitaigorodskii et al. 1975, Forristall 1981, Kahma 1981).

Longuet-Higgins (1969) demonstrated that α is related to the wave age. Hasselmann et al. (1973) in a careful study of fetch-limited waves related α to the non-dimensional fetch $\tilde{x} = xg/U^2$. In these studies the power law which described the rear face of the spectrum varied between -3.5 and -5.0. It would appear that not only is α not a constant but the frequency dependence of the rear face may also vary considerably.

Accordingly, as a starting point in describing our spectra we examined them to attempt to determine the characteristics of the rear face of the spectrum. In the "energy containing" region of the spectrum, i.e., spectral levels greater than 1% of the peak, the rear face of the spectrum is well described by an ω^{-4} power law. To illustrate the slope of the rear face the spectra have been multiplied by ω^4 and normalized by the average level of the spectral estimates multiplied by ω^4 in the frequency region $1.5\ \omega_p < \omega < 3.0\ \omega_p$ (see figure 8.3). It is clear than an ω^{-4} power law is a good description of the rear face of the spectrum in the energy containing region. For comparison ω^{-5} and ω^{-3} power laws are also shown. Although harmonic peaks are clearly evident in the largest U_c/c_p spectral group, the mean spectral level is in good agreement with the ω^{-4} line. Both the laboratory and field data support an ω^{-4} description of the rear face of the spectrum in the frequency region $1.5\ \omega_p < \omega < 3.5\ \omega_p$ of the wind-generated gravity wave spectrum. Although the result we have quoted is simply an empirical one, there is theoretical support for an ω^{-4} equilibrium range in the work of Zakharov and Filonenko (1967).

It is not our purpose here to try to reconcile our observations with the enormous literature of wave spectra which has gone before. We emphasize, however, that we have confined our attention to the energy containing region of the rear face of the wind-generated gravity wave spectrum, because it is here that a simple and accurate spectral description finds frequent and valuable practical application.

The establishment of a power law appropriate to the rear face of the wave spectrum is often troubled by the possibility of

Doppler shifting of the spectral estimates by currents (Kitaigorodskii et al. 1975). Tidal currents in Lake Ontario are insignificant in this context, and the wind-driven and thermal circulation produces upper layer currents which are generally less than 10 cm/s (Simons 1974, 1975). The field spectra have been analyzed in 15 frequency bands with lowest and highest centered on 0.044 Hz and 1.139 Hz respectively. Therefore the ratio of phase speeds to current speeds is 13 or greater and the calculations of Kitaigorodskii et al. (1975) indicate that the Doppler shift does not materially alter the slope of the rear face. Furthermore there is no reason to suppose that the direction of the currents and waves are correlated. In fact the waves tend to be offshore or onshore (prevailing wind directions) and the lake currents are inclined to be shore parallel (topography steered). Nonetheless, we have indicated (figure 8.3) the maximum distortion to the observed ω^{-4} slope based on Kitaigorodskii et al. (1975) for 10 cm/s currents with and against the waves. We have used their results for the cosine squared distribution since this is in reasonable agreement with the directional spread (§11) at high ω/ω_p where the Doppler shift might be important. It appears that the effect on the spectral slope of the ambient currents is not significant in these lake data, and of course does not exist in the laboratory tank data.

Doppler shifting due to surface wind drift may, in some instances, be an important factor. The combination of short waves and strong winds is particularly prone to this source of error, since the current is strongly sheared near the surface and is about 2.5% of the wind speed or 0.55 u_* (Wu 1975). In §10 we demonstrate that in strong surface shear the short waves appear to be advected at a speed corresponding to the current speed at a depth O(1/k). An approximate correction for the wind drift (field data) is indicated on figure 8.3 based on an average wind speed of 10 m/s and the wind drift profile inferred by Donelan (1978). It can be seen that this correction is only of importance in these field data for $\omega/\omega_p > 3$. Furthermore correcting for this source of error would make the spectral slope slightly more negative than ω^{-4} for $\omega > 3\ \omega_p$ and essentially

unchanged for $\omega < 3\ \omega_p$. Evidently an ω^{-4} power law provides an excellent description of the rear face of these lake spectra in the energy containing region $1.5\ \omega_p < \omega < 3\ \omega_p$.

The laboratory spectra show a tendency to increase slope above $\omega/\omega_p = 3.2$, which is probably due to wind drift currents. We will explore this further in §10. However we remark that it is difficult to assign a slope to the rear face of the spectrum of the strongly forced ($U/c_p > 9$) laboratory waves, because of the presence of pronounced harmonic peaks (see §10). Moreover we are attempting to find a general description for the spectra of natural waves, and are using the laboratory data only to extend the parameter space beyond that which can be realized with our field site. The rationale for this is that the broader parameter ranges thus achieved help us to discern trends which may otherwise be buried in the noise - sampling and geophysical variability - of the field data. At the same time we remain fully cognizant that in many instances the differences between the conditions of the laboratory and lake are sufficient to prevent close quantitative correspondence between them.

Inasmuch as the rear face of both the laboratory and field spectra falls off as ω^{-4} previous spectral shapes based on an ω^{-5} rear face, such as the Pierson-Moskowitz (1964) and JONSWAP (Hasselmann et al. 1973), are not appropriate. More recently, Huang et al. (1981) have proposed a spectral model in which the slope of the rear face is dependent on the "significant slope", an internal parameter of the wave field defined as the ratio of root-mean-square surface elevation to the wave length of the spectral peak. While the model of Huang et al. provides some flexibility in the slope of the rear face of the spectrum, it does not attempt to describe the peak enhancement independently - deemed so important in the JONSWAP data. Or alternatively, in describing the energy containing region about the peak of the spectrum, their model deviates considerably from the observed behaviour of the equilibrium region.

8.2 The Parameters of the Spectrum

Our spectra are characterized by relatively constant rear face slope (ω^{-4}) and pronounced peak enhancement (figure 8.3). Accordingly the JONSWAP spectral model, modified to account for the ω^{-4} rather than the ω^{-5} rear face, would seem a plausible candidate for describing these spectra. The modification consists of replacing ω^{-5} by $\omega^{-4}\,\omega_p^{-1}$:

$$\Phi(\omega) = \alpha g^2\,\omega^{-4}\,\omega_p^{-1}\exp\left\{-\frac{5}{4}\left(\frac{\omega_p}{\omega}\right)^4\right\}\cdot\gamma^{\exp\left\{\frac{-(\omega-\omega_p)^2}{2\sigma^2\,\omega_p^2}\right\}} \tag{8.1}$$

$$\sigma = \begin{cases}\sigma_a & \text{for} \quad \omega \leq \omega_p \\ \sigma_b & \text{for} \quad \omega > \omega_p\end{cases}$$

The five parameters of this model are: ω_p, α, γ, σ_a, σ_b. We retain the JONSWAP designations:

- ω_p is the frequency of the spectral peak.
- α is the equilibrium range (rear face) parameter.
- γ is the peak enhancement (over the Pierson-Moskowitz spectrum) factor.
- σ_a, σ_b are peak width parameters.

The dependence of the equilibrium range parameter α on U_c/c_p is shown in figure 8.4. $U_c = U\cos\theta$ is the component of the wind in the direction of travel of the waves at the spectral peak. The ratio U_c/c_p is a measure of the wind input and might be expected to affect α. In spite of the scatter in the field observations, there is a clear dependence of α on U_c/c_p. The field data suggest the following relationship between α and U_c/c_p:

$$\alpha = 0.006 \left(\frac{U \cos \theta}{c_p} \right)^{0.55} \tag{8.2}$$

Kahma (1981) argues strongly in favour of an ω^{-4} rear face based on accelerometer buoy data from the Gulf of Bothnia. His spectra are based on Toba's (1973) formulation and have an equilibrium range parameter which, converted to the form of α in (8.1), has the linear wind speed dependence indicated on figure 8.4 for the range of Kahma's data. Evidently, Kahma's α is not inconsistent with our data for the range in U/c_p of his data. However it cannot be comfortably extrapolated to cover the wider range of our data.

It is also apparent from figure 8.4 that the laboratory and field data are drawn from different populations. The sudden decrease in α from the field trend (extrapolated) suggests a basic field/laboratory change in the mechanisms of generation or dissipation of the short waves on the rear face. The most obvious change to the generating process is the constraint on the lateral variation of the wind vector imposed by the tank walls. This would be expected to reduce the directional spread of the "saturated" waves simply because the mean wind meandering has been arrested. However there may be an additional reduction in the generation rate because of the reduced efficiency of mechanisms such as that hypothesized by Stewart (1974). With increasing wind, the wavelengths, group speeds, decay times and distances all increase thereby widening the area of influence of breaking at the side walls of obliquely propagating waves. This tends to narrow the directional spread and hence reduce α. As the winds are increased further the rapid increase of the wind input overcomes the side wall effects and α increases quickly.

Another possible reason for the initial decrease of the laboratory α values is the effect of wind drift on limiting the amplitude of the waves at breaking. Banner and Phillips (1974) have shown that the wave amplitudes are reduced by $(1 - q/c)^2$ where q, the

wind drift, is approximately 0.025 U. For the waves on the rear face at $\omega = 2\omega_p$, this reduces to $(1 - 0.05\ U/c_p)^2$. Initially this has the effect of reducing α with increasing U/c_p. However, eventually the waves become too long for their breaking amplitude to be greatly modified by the thin shear layer at the surface and the effect of strengthened wind input dominates causing α to increase again.

When the spectra are normalized with respect to the equilibrium range (figure 8.3), systematic changes in the height of the peak with respect to the parameter U_c/c_p are manifest. At very low values of U_c/c_p the peak is actually below the equilibrium range in $\omega^4\Phi(\omega)$ coordinates. In the terminology of JONSWAP (Hasselmann et al. 1973), the "peak enhancement parameter" γ is graphed in figure 8.5. A systematic increase of γ with U_c/c_p is evident. This contrasts markedly with the JONSWAP result (Hasselmann et al. 1973) in which the values of γ derived from individual spectra were scattered over a range of 6 with no significnt correlation with non-dimensional fetch. At values of U_c/c_p less than unity, γ seems to be fairly constant at 2.2. However the peak value of the spectrum at full development ($U_c/c_p = 0.83$) differs from Pierson and Moskowitz (1964) by less than 40% because the equilibrium range parameter (figure 8.4) is only 0.0054 at $U_c/c_p = 0.83$ compared to the constant Pierson-Moskowitz value of 0.0086. For the field data, the peak enhancement factor may be described by:

$$\gamma = \begin{cases} 2.2 & \text{for } 0.83 < \dfrac{U_c}{c_p} < 1 \\ 2.2 + 7.7 \log_{10} \left(\dfrac{U_c}{c_p} \right) & \text{for } 1 \leq \dfrac{U_c}{c_p} < 6 \end{cases} \qquad (8.3)$$

The laboratory data show a sharp increase in γ to a maximum at $U_c/c_p = 11$ followed by a sharp decrease at higher values of U/c_p. Visual observations of the intensity of wave breaking in the tank suggest the following general interpretation. Increasing the

rate of wind input raises the level of the spectrum generally. Energy accumulates most rapidly near the peak possibly because wind input is strongest there and the nonlinear wave-wave interaction processes are too weak to transfer energy to lower frequencies at the rate it is being absorbed by the wind. Eventually the energy density near the peak is so large that wave breaking acts strongly to limit the growth near the peak. The growth of the less steep waves on the rear face continues (and is perhaps enhanced by the splashing caused by the breaking of the larger waves) and results in an increasing α, but a decreasing γ, since γ is, in effect, a measure of enhancement of the peak over the equilibrium range extended to the peak. Presumably at very high values of U/c_p both α and γ, being limited by frequent breaking, will approach constancy.

Supporting evidence for this interpretation is given by the behaviour of the bound harmonics (§10). At values of U/c_p above 9 the energy in the bound harmonics of the peak surpasses that in the free waves at the same frequency. This implies rapid steepening of the waves near the peak of the spectrum as U/c_p is increased beyond 9.

The spectral width parameters σ_a and σ_b (figures 8.6 and 8.7) show no pronounced dependence on U/c_p. In both cases most of the estimates fall between 0.1 and 0.2. We have taken 0.15 as representative of both σ_a and σ_b. Some of the scatter of the estimates plotted in figures 8.6 and 8.7 may be due to sampling variability.

8.3 Non-Dimensional Fetch and Energy

Using the dispersion relation from linear theory for the waves near the peak of the spectrum, U_c/c_p is related to the JONSWAP non-dimensional frequency $\tilde{\omega} = \omega_p U/g$ by:

$$\frac{U_c}{c_p} = \tilde{\omega} \cos \phi$$

where ϕ is the angle between the wind and the mean propagation direction of the waves at the peak of the spectrum.

Figure 8.8 shows the dependence of non-dimensional fetch $\tilde{x}$ on U_c/c_p over five orders of magnitude in $\tilde{x}$. Field and laboratory data are nearly contiguous, but a power law (solid line) fitted to the field data clearly does not represent the laboratory results. The laboratory data fall on a line (dotted) which is displaced upward and to the right of the power law representing the field data. Phillips (1977) has remarked that the laboratory and field data summarized by Hasselmann et al. (1973) do not necessarily conform to the same similarity law and fitted a power law (shown dashed) to the field data only. The laboratory wind speeds are the equivalent neutral profile wind speeds at 10 m height using the measured friction velocities. Had we used the wind speed at a lower height, commensurate with the shorter wave lengths of the laboratory waves, the laboratory points would have been in closer agreement with the extrapolated field line of figure 8.8. However, the opposite trend would have occurred in figure 8.9, thereby demonstrating that no wavelength related choice of U(z) can reconcile the laboratory and field data in terms of Kitaigorodskii's (1962) theory.

The change in spectral energy density following the waves is described by the radiative transfer equation (Hasselmann et al. (1973):

$$\frac{\partial \Phi}{\partial t} + \overline{v}_i \frac{\partial \Phi}{\partial x_i} = I + W + D$$

where $\overline{v}_i$ is the group velocity averaged over direction, and the right hand side consists of three sources: wind input I, wave-wave interaction W and dissipation D.

For the conditions of their fetch-limited data Hasselmann et al. (1973) estimate that near the peak the sources are dominated by

wind input and wave-wave interaction; dissipation is important only at higher frequencies. However, in the much steeper laboratory data it seems unlikely that dissipation near the peak can be considered negligible. In fact, at high values of U/c_p visual observation suggests that the waves near the peak of the spectrum are being dissipated by wave breaking. Evidently, the wave-wave interaction processes are too weak to transport the rapid wind input to lower frequencies; there is a pile up of energy near the peak and the dissipation is increased there. The net effect is that the peak frequency is higher than it would be if wind input and wave-wave interaction dominated the source function. Higher frequency, or lower phase speed c_p, has the effect of moving the laboratory points to the right in figures 8.8 and 8.9.

Figure 8.9 relates non-dimensional variance $\tilde{\varepsilon}$ $(=\overline{\zeta^2}g^2/U_c^4)$ to U_c/c_p. The field data seem to be in excellent agreement with a power law dependence (solid line) on U_c/c_p. Here again the laboratory data deviate from the line, but the disagreement with the field data occurs at somewhat higher values of U_c/c_p than in figure 8.8.

In figure 8.9 we have indicated the range of U/c_p covered by the JONSWAP data (Hasselman et al. 1973). Over this range their data is sufficiently scattered to cover the solid lines suggested by our data in both figures 8.8 and 8.9. In other words, the results of both sets of observations (JONSWAP and this work) are consistent. However, the lines fitted by Hasselmann et al. to the JONSWAP data appear to have been biased away from those fitted to our data by the inclusion of laboratory data in the same similarity framework.

8.4 Comparison with Other Spectra

In figure 8.10 we compare the JONSWAP (Hasselmann et al. 1973) and Pierson-Moskowitz (1964) spectra with the spectra represented by (8.1). Two values of U/c_p (4 and 0.83) are shown corresponding to non-dimensional fetches of 10^2 (fetch-limited) and

10^5 (fully-developed). The values of wind speed and fetch appropriate to these spectra (ω_p = 2.5) are respectively 15.6 m/s and 2.5 km (fetch-limited) and 3.2 m/s and 104 km (fully-developed). The Pierson-Moskowitz spectrum applies only to full development, and it is encouraging that the spectrum of (8.1), derived from fetch-limited data only and extrapolated to full development, is in good agreement with the Pierson-Moskowitz. At the other end of the scale of strongly fetch-limted spectra, the JONSWAP spectrum is in reasonable agreement with (8.1). However, the JONSWAP spectrum, extrapolated to full development, retains its enhanced peak and is therefore unable to relax to the broader peaked fully-developed spectrum. The differences between the JONSWAP spectrum and (8.1) hinge on the choice of the power law for the rear face of the spectrum. Figure 8.3 amply establishes the choice of ω^{-4} for these data, and the much-reduced scatter in α and γ relative to the JONSWAP results, coupled with the smoother transition from fetch-limited to fully-developed conditions, attests to the appropriateness of the spectral description of (8.1).

8.5 Equilibrium Level Versus Wind Speed

Although for most engineering purposes, knowledge of the spectrum in the energy containing region ($1/2 < \omega/\omega_p < 3$) is sufficient, the rapid growth of remote sensing of the ocean surface has spawned a need for the spectral behaviour at short wave lengths (less than 1 metre). Pierson (1981) describes the use of a satellite scatterometer for estimating wind speeds over the ocean. The excellent correlation, which he has obtained between ship-borne and scatterometer estimates of wind speed, suggests a strong dependence on wind speed of the energy in the very short gravity waves (2.5 cm). While the scatterometer responds to wavelengths somewhat shorter than those included in our field measurements, the changes in energy level

of the rear face of our spectra with wind speed may give some indication of the behaviour of the shorter waves.

More direct, but perhaps less well documented, evidence for the wind speed dependence of the short gravity waves can be drawn from the normalized radar cross section σ_0. Wright (1968) has shown that σ_0 is proportional to the wave spectral density of the Bragg scatterers. For L-band radar (1.2 GHz) the surface wavelengths are about 25 cm. Weissman et al. (1979) have obtained a reasonable correlation between wind speed to the power 0.58 and σ_0 during a hurricane, in which the waves would be almost certainly fetch-limited. Jones and Schroeder (1978) in a review article cite σ_0 dependencies on wind speed for L-band radar with power laws ranging from -0.3 to +1.54.

The rear face of the spectrum (8.1) is described by:

$$\Phi(\omega) = \alpha g^2 \omega^{-4} \omega_p^{-1}; \qquad \omega > 2\omega_p$$

substituting for α from (8.2):

$$\Phi(\omega) = 0.016\, g^{1.45} \omega_p^{-0.45} \omega^{-4} U_c^{0.55} \tag{8.4}$$

Thus, for a fixed peak frequency ω_p, the energy density at a given frequency ω increases approximately as the square root of the wind speed component ($U_c = U \cos \phi$). In terms of U_c/c_p (8.4) can be written:

$$\Phi(\omega) = 0.038\, g\, \omega^{-4} \left(\frac{c_p}{U_c} \right)^{.45} U_c \tag{8.5}$$

Except during storms, open ocean conditions tend to approach full development with $0.83 \leq U/c_p < 1$. Thus, under these conditions, σ_0 might be expected to be linearly proportional to wind speed.

Evidently the available data on the radar cross section in the short gravity wave region are not supplemented by sufficient information on the wave field to allow testing of the relationship between σ_0 and Φ (ω). However, the evidence which does exist appears to be consistent with the spectral form given here (8.1).

The fetch-limited result (8.4) reveals that, for a fixed wind speed, the energy density at a given frequency increases with increasing peak period T_p or increasing fetch. Since the spectral levels in the equilibrium region reflect a balance between wind input, dissipation and wave-wave interaction, any of these are possible candidates for an explanation of this result. In particular, the spectral form of nonlinear wave-wave interaction (Hasselmann et al. 1973, Dungey and Hui 1979) indicates that as the peak moves to lower frequencies the rate of energy egress from the shorter waves is lessened. The mechanism of attenuation of short waves by wind drift and longer wave orbital velocities (Phillips and Banner 1974) would also tend to produce this effect, since the mechanism weakens as the long waves develop thereby becoming less steep. It is also possible that the wind input to a particular frequency on the rear face of the spectrum could be affected by its position in the spectrum; in particular, its closeness to the peak.

Relation (8.5) suggests that a linear dependence of wind speed on σ_0, based on normal oceanic conditions, might underpredict the wind speed in severe storms where U_c/c_p might be appreciably greater than 1. See, for example, the huricane data of Weissman et al. (1979).

By contrast, the energy density in the equilibrium range of the JONSWAP fetch-limited spectrum depends on $U^{2/3}$ decreases with increasing fetch and, if extrapolated to full development, is independent of wind speed.

9. WAVE DIRECTION VERSUS WIND DIRECTION

Both in the execution of steady-state fetch-limited experiments and in the application of fetch-limited formulae in hindcasting, it is common practice to assume that the mean wave propagation direction agrees with the wind direction. That this cannot be true in general is evident from the fact that waves are not strictly locally generated, but instead are the net result of their development along the entire upwind fetch. If, therefore, the gradient of fetch about the wind direction is large one might reasonably expect the wave direction to be biased towards long fetch, where the reduced generating force of the lower wind component ($U \cos \theta$) is more than balanced by the longer fetch over which it acts. In figure 9.1 the observed mean direction of the waves near the peak of the spectrum is plotted against average wind direction. The straight line (dashed) is the line of perfect agreement with the wind direction. When the fetch gradient is small - wind directly offshore (-120°) or along the long axis of the lake (75°) - the wave and wind directions agree. Otherwise, the discrepancies can be as much as 50°. Certainly such differences call into question the validity of hindcasting techniques which disregard them.

Initial attempts to use Kitaigorodskii's scaling law for non-dimensional frequency with fetch in the wind direction produced a much poorer correlation than that of figure 8.8. This supports the view that, unless the wind is blowing directly offshore from a straight shoreline, more appropriate parameters for similarity scaling are the fetch and wind component in the wave direction rather than the wind direction. The similarity relation of figure 8.8 may be written in terms of the peak period T_p:

$$T_p = 0.54\, g^{-0.77}\, U^{0.54}\, (\cos \theta)^{0.54}\, x^{0.23} \qquad (9.1)$$

where x is the fetch in the wave propagation direction.

Since the energy density at the peak of the spectrum is roughly proportional to T^5_p (Phillips 1977, figure 4.8), it is clear that the direction (θ) which yields the largest value of T_p from (9.1) will be the direction of approach of the waves at the peak of the spectrum.

For any wind speed U such that the waves are fetch-limited, the right-hand side of (9.1) ($\cos\theta . x^{0.426}$) may be maximized to yield the offwind angle θ of approach of the peak of the spectrum. Running averages of the geometric fetch at one degree increments over various windows from ±0 to ±30° were computed and used to deduce the peak wave approach direction. The sensitivity to width of averaging window was not large as demonstrated in the inset to figure 9.1 for window widths of 0 and 60 degrees. The best agreement (solid line in figure 9.1) with the observed wave approach direction was achieved with window width of 30°, i.e. ±15 degrees on either side of θ.

10. PHASE SPEED

Attempts to assess the behaviour of natural waves using laboratory tanks often run into some difficulty with the excess of steepness of laboratory tank waves over natural waves. This comes about because strong wind forcing is necessary to produce a reasonable spectrum of gravity waves in the short fetches (<30 m) possible in most laboratory tanks. The presence of harmonics can be seen in the power spectra and the dispersion relation is typically as described by Ramamonjiarisoa (1974). Spectra of natural wind waves, on the other hand, do not show pronounced harmonic peaks. In this regard, we were able to employ the longer fetch possible with our tank to produce waves which were reasonable facsimiles of natural waves. Compare the log-log frequency spectra of figure 10.2 and the dispersion relation of figure 10.1 for the natural waves of run 128173 (U/c_p = 3.6) with those of the laboratory run 3 (U/c_p = 8.5). On the basis of these two figures only, one would be inclined to group laboratory run 3 with the natural waves rather than with the steeper laboratory waves of runs 5, 7 and 30 (U/c_p = 11.8, 15.9 and 16.5 respectively). It appears that laboratory experiments in large tanks can produce results which are contiguous with observations in nature in some respects, though not all (see §8).

In this section we explore the dispersion relation of waves in the laboratory and in the field. We make use of the greater statistical reliability and accuracy of the laboratory measurements to assess directly the significance of bound harmonics of the steep waves near the peak. Extending these results to the field, we attempt to provide a coherent picture of the dispersion relation for wind-generated waves in field or laboratory.

10.1 'Average' Phase Speed

Having gained access to the wave-number frequency spectrum $X(\underset{\sim}{k}, \omega)$, we are able to examine the phase speed characteristics of

wind-generated gravity waves in a direct way. The phase speed of any frequency component is defined by $c(\omega) = \omega/k$. Therefore, we may examine the average phase speed of any frequency component, ω_1 by obtaining an average wave-number $\bar{k}_{(\omega_1)}$ from $X(\underset{\sim}{k}, \omega_1)$

$$\bar{k}(\omega_1) = \frac{\iint k\ X\ (\underset{\sim}{k},\omega_1)\ dk\ d\theta}{\iint X\ (\underset{\sim}{k},\omega_1)\ dk\ d\theta} \tag{10.1}$$

Calculations of the phase speed performed in this way are shown in figure 10.1. They are in ascending order of U/c_p. The lowest two are derived from field data, the rest from laboratory data. The hyperbola (solid line) represents the dispersion relation given by linear theory: $c = (g/k)^{1/2}$. At the lowest value of U/c_p the wave field is almost fully developed and the waves at the peak are in obedience of the linear dispersion relation. However, at somewhat higher frequencies than the peak, the measured phase speeds are in excess of the theoretical. In all but the lowest value of U/c_p the measured phase speeds near and above the peak are in excess of the theoretical phase speed. The deviation from the theoretical value increases steadily with U/c_p, until at the highest values of U/c_p the phase speed at twice the peak frequency ω_p is about equal to the phase speed at the peak. As already noted in §6.2, this behaviour is due to the presence of bound harmonics as reported previously by Ramamonjiarisoa (1974), Lake and Yuen (1978) and Mitsuyasu et al. (1979). Plant and Wright (1980), on the other hand, find that their observed deviations from the linear dispersion relation were best accounted for by Doppler shift due to wind drift.

Komen (1980) has calculated the expected phase speed changes based on a balance of free and bound waves. His results are qualitatively similar to figure 10.1.

Apart from the work of Plant and Wright (1980), previous laboratory phase speed measurements have been based on two-point correlations of surface intersecting wave gauges. Longuet-Higgins (1977) has pointed out that the apparent deviation of the measured phase speed from the theoretical curve could be due to the offwind

propagation of various wave components such that their downwind phase speed was constant. This leads to a bimodal directional distribution, much as in Phillips (1957) resonance theory, in which the energy is greatest at angles $\theta = \pm\cos^{-1}(c/V)$; where V is the wind speed or phase speed of the waves at the spectral peak in the theories of Phillips and Longuet-Higgins respectively. The validity of this theory cannot be checked from two-point correlations and, in fact, some assumption about the directional spread is prerequisite for interpreting the observed phase speeds (Mitsuyasu et al. 1979). Our method is free of these uncertainties since we obtain the full three-dimensional wave-number - frequency spectrum, from which the average wave-number in any frequency band, and thus the average phase speed, may be obtained.

In strongly forced laboratory situations as in run 5, the energy observed in the neighbourhood of $\omega = 2\omega_p, 3\omega_p, 4\omega_p, \ldots$ is largely due to higher harmonics bound to the dominant wave near the peak frequency ω_p. The balance between such bound harmonics and free waves will be explored further in this section. Thus the second harmonic of the dominant wave ω_p would show up in the wave-number spectrum for frequency $2\omega_p$ at about* 1/2 of the radius of the linear dispersion circle, whereas the third harmonic would show up in the wave-number spectrum for frequency $3\omega_p$ but at about 1/3 of the radius of the circle, etc. For the bound harmonics the phase speed at $\omega = 2\omega_p, 3\omega_p, \ldots$, is the same as that at the peak c_p. However, since the spectrum is not a delta spike at ω_p, but rather a narrow spectrum with most of the energy concentrated in a frequency band $\Delta\omega$ around ω_p, the effects of higher harmonics of the components in the frequency band will lead us to the conclusion that the phase speed must be almost equal to c_p in the frequency bands $2\Delta\omega$ around $2\omega_p$, $3\Delta\omega$ around $3\omega_p$, ... etc. All these theoretical predictions are

---

* Actually the bound energy in the nth harmonic would appear at 1/n the radius of the nonlinear dispersion circle corresponding to (2.8) since the harmonics travel at the speed of their fundamental which itself, by virtue of the existence of harmonics, is in obedience of (2.8) rather than (1.1).

indeed observed experimentally for high values of U/c_p. While this explanation is similar to those offered by Phillips (1977), it should be pointed out that his explanation is not valid for frequencies between ω_p and $2\omega_p - \Delta\omega$, and between $2\omega_p + \Delta\omega$ and $3\omega_p - 3/2\Delta\omega$, etc. For these frequencies, the departure from the dispersion circle must be due to the local effects of finite-wave slope (as discussed in §2.1) which can be up to about 20% in wave-number or 10% in phase speed, in agreement with observations (figure 10.1). Combining both effects of higher harmonics and of local Stokes' effect, theory predicts that the curve of average phase speed versus frequency for $\omega > \omega_p$ is wavy, but as ω increases it will tend to a relatively constant level near c_p if the bound harmonics contain much more energy than the free waves at these frequencies. This occurs when $\omega/\omega_p \geq \omega_p/\Delta\omega - 1/2$ in strongly forced cases and is clearly confirmed by laboratory experiments for large values of U/c_p (figure 10.1).

For historical perspective we have opened this section with a look at average phase speeds. Observations of phase speeds in both natural and laboratory conditions have given rise to questions regarding the dispersive nature of wind waves. Should we regard the wave field at $\omega > 1.5\ \omega_p$ as non-dispersive on the basis of observations such as those reported above? Observations of average phase speeds are somewhat ambiguous because, if bound waves do exist, averages over the wave-number plane or two-point correlations include the effect of two dynamically quite distinct sets of waves. Fortunately in our case we can, in principle, restrict our attention to regions of the wave-number plane containing only free waves or any of the several bound harmonics.

10.2 Phase Speed of Free Waves

In figure 10.3 we examine the phase speed of the free waves only. This is done by obtaining an average wave-number over a band of wave-numbers limited at low wave-number by the arithmetic mean of the expected free wave-number ($k_f = \omega^2/g$) and the expected second harmonic wave-number ($k_2 = \omega^2/2g$) and limited at high wave-number by a

band of equal width. The effects of amplitude dispersion are now clear. The almost fully-developed case (U/c_p = 1.0) shows no sign of amplitude dispersion below ω/ω_p = 1.3. Above this there is a moderate increase in the phase speed above the theoretical curve. With increasing U/c_p the effects of amplitude dispersion are noticeable near the peak and above. On the assumption that the waves are distorted in accordance with Stokes' theory[1] (§2.), the maximum amplitude dispersion corresponding to the Stokes' steepness limit (ak = 0.44) is 10%. At the highest values of U/c_p the waves at frequencies just above the peak approach the phase speed appropriate to the maximally steep Stokes' waves. It is interesting to note that at the highest value of U/c_p the phase speed near the peak shows less evidence of amplitude dispersion than in the laboratory runs at somewhat lower U/c_p. It is possible that widespread breaking of the waves near the peak reduces the steepness of these waves. This interpretation is consistent with the behaviour of γ, the peak enhancement factor §8.2 and the calculations of Longuet-Higgins and Cokelet (1976) which show that waves are maximally steep somewhat before breaking.

10.3 Phase Speed of Bound Harmonics

One can also determine the dispersion relation of the bound harmonics. To avoid contamination of the average wave-number of the second harmonic the region in wave-number space considered was bounded below by the arithmetic mean of the expected wave-number of the second and third harmonics ($k_n = \omega^2/ng$) and above by the arithmetic mean of the expected wave-number of the second harmonic and of the free wave at that frequency. It was possible to resolve the average wave-number for the second harmonic in the laboratory runs with high values of U/c_p only. These are shown in figure 10.4. The lower hyperbola is,

---

[1] Support for this is provided by Lake and Yuen (1978) who have shown good agreement between the ratio of spectral amplitudes of harmonic and fundamental and the predictions of Stokes' (1880) theory.

as before, the theoretical linear dispersion relation; the upper hyperbola is the locus of speeds twice as great as the lower and is the speed at which bound second harmonics would travel if trapped on waves of half the frequency on the lower curve. The bars correspond to limits of the band of averaging and the dashed line would result from a uniform distribution of energy within the band; i.e. white noise. At frequencies below 2.0 H_z we cannot effectively separate second and third harmonic contributions to the energy density. Therefore, lower frequencies do not appear in figure 10.4. At the highest frequencies the points approach the white noise result. Between these two extremes, however, the phase speeds very definitely support the idea that these are second harmonics of the free waves of figure 10.3. The open circles are taken from the measured phase speeds of figure 10.3 transposed to twice the frequency. They represent the speed at which the bound harmonics must travel to be consistent with the measurements of figure 10.3. While it is possible that wind drift could affect the measured phase speed, it will not affect the comparison between figures 10.3 and 10.4 discussed above.

10.4 Amplitude Dispersion and Doppler Shift of Laboratory Waves

It is, of course, impossible to generate wind waves without also producing a strongly sheared current near the surface. The presence of such a current has been used by some researchers (Lake and Yuen, 1978; Mitsuyasu et al., 1979; Plant and Wright, 1980) to explain part of the excess speed of measured waves above the linear theory. In addition Plant and Wright (1980) have pointed out that the wind itself will increase the propagation speed of the waves a small but measureable amount. We recognize that some effect of both current and wind forcing must be present in our data. However, since our laboratory waves are somewhat longer that those discussed in previous work yet our wind speeds and currents are similar, these effects would be less pronounced in our data. Nonetheless, in the following we assess the effects of currents.

The ratio of the energy in the bound wave to the free wave is graphed versus ω/ω_p in figure 10.5 for the laboratory data. It

is clear that with increasing U/c_p the energy in the second harmonic waves begins to dominate the spectrum above $\omega/\omega_p = 1.9$ and the shape of the peak of the spectrum - forward face sharper than rear - is reflected in the energy of the second harmonic. In figure 10.6 the ratio of energy in the second harmonic to that in the free waves is graphed versus U/c_p for various values of ω/ω_p. From this it would seem that at values of U/c_p in excess of 9 evidence for bound harmonics will appear in the power spectra and the dispersion relation at values of ω/ω_p in the neighbourhood of 2.1. Such values of U/c_p occur only fleetingly in nature except on small ponds. Thus the theoretical dispersion relation with some amplitude dispersion is generally adequate to describe natural wind-generated wave spectra and laboratory tank spectra for which $U/c_p < 9$.

We now turn our attention to the question of how much amplitude dispersion is appropriate. Since we have access to the energy in the bound harmonics, we may compare this to the energy in the corresponding free wave (fundamental) and, in a Stokian model, thereby establish the slope of the fundamental wave. Figure 10.7 shows the result of this calculation for the laboratory data. The steepness increases steadily above the peak and begins to approach the theoretical limit at $\omega/\omega_p = 1.5$. Beyond this there is insufficient resolution of the wave-number spectra to determine the energy in the second harmonic which would be found at $\omega/\omega_p > 3.0$. We know that the spectrum falls off to infinitesimal amplitudes at $0.6 < \omega/\omega_p < 0.8$ (see figure 8.2) so that the extrapolation (dashed lines) towards low ω/ω_p values is probably in order.

These steepness estimates allow us to compute the Stokes' phase speeds for the free waves and to compare them with the observed phase speeds of figure 10.3. The difference (measured phase speed c_m minus Stokes' phase speed $c_s = g/\omega[1 + (ak)^2 + 1/2(ak)^4]^{1/2}$) is further adjusted by the correction given by Plant and Wright (1980) due to the air flow over the waves, c_a. The Stokes' correction is positive and can account for up to 10% of the linear theory, the air flow adjustment c_a is negative and between 1 and 3% in all cases.

The difference $(c_m - c_s - c_a)$ varies between -4% and +10% and is probably due to a combination of experimental error and differential advection of the wave components by sheared current.

In the laboratory tank the wind-driven current profile has been found to scale with the surface friction velocity and the total depth (Donelan 1977). Therefore in figure 10.8 we examine the difference $(c_m - c_s - c_a)_k$ normalized by the surface friction velocity u_* versus the wavelength $\lambda = 2\pi/k$ to total depth ratio. Although the data are somewhat scattered, there is a definite trend from slow upwind advection of the longer wavelengths $\lambda/H > 0.8$ to downwind advection of the shorter wavelengths, which when extrapolted to vanishing wavelengths suggests a surface advection of approximately $15u_* \approx 0.02$ U. Calculations by Stewart and Joy (1974) suggest that the waves are advected by the mean current at a depth corresponding to some fraction of a wavelength depending on the current profile. Matching the wind-driven current profile obtained by Donelan (1977) from the same tank as in the present experiment, it would appear that the current at depth $z = 1/k$ is reflected in the residual wave advection speed after amplitude dispersion and wind forcing have been accounted for. The advection velocity from the theory of Stewart and Joy (1974) can be calculated from a known velocity profile. Thus in the region above the change of sign of the velocity gradient, the profile measured by Donelan (1977), is reasonably well represented by:

$$\frac{U}{u_*} = -1.8 + 16.8\, e^{18.6\, z/H} \qquad (10.2)$$

From which, following Stewart and Joy (1974)

$$\frac{U_w}{u_*} = \left[-1.8 + \frac{16.8}{1 + 1.18\,\frac{\lambda}{H}} \right] \qquad (10.3)$$

This theoretical wave advective current is graphed (solid line) in figure 10.8. It is clear that the calculations of Stewart and Joy (1974) are inappropriate in this situation. Possibly the effects of wave breaking, omitted from their theory, serve to deepen the effect of the currents on these waves.

10.5 Amplitude Dispersion of Field Waves

Lacking sufficient resolution at high frequencies in the field directional spectra, we are unable to compute the Stokes' distortion from the relative magnitudes of free waves and harmonics. Instead, having gained confidence from the consistent picture provided by the laboratory results, we will do the calculations in reverse order for the field data. That is, having first removed the calculated effects of wind forcing c_a (0.28/k) and drift current U_w (-1/k), the residual measured phase speed excess will be taken to be due to amplitude dispersion, plotted (figure 10.9) and used to estimate the slope (figure 10.10). The drift current profile is computed using (10.2) based on the field measurements by Donelan (1977) at the same site. Figures 10.9 and 10.10 are summaries of the 18 field cases in which the directional spectra were well resolved to at least $\omega/\omega_p = 2.2$. The are grouped by U/c_p. The two higher U/c_p curves show a consistent picture of appreciably steep waves in the region near the peak ($0.9 < \omega/\omega_p < 2.0$). For the lower U/c_p case the steepness rises to nearly 0.3; in the other case (U/c_p = 2.9) the steepness rises to nearly 0.4.

Figures 10.9 and 10.10 show the phase speeds and steepness both with and without correction for the assumed drift current and wind forcing. In the steady state these effects are proportional to u_*. The almost fully-developed case with small u_* is hardly affected by these corrections. On the other hand, the moderately generated case has its phase speed excess and concomittant steepness reduced to zero near $\omega/\omega_p = 2.1$, while the strongly generated case with large u_* appears to be overcorrected. Quite possibly the drift

currents have been overestimated. It may be that the steady-state profile assumed for the drift current is in error. The spin up time for the Ekman boundary layer is of the order of half a pendulum day or about 17 hours for Lake Ontario, which is generally longer than the duration of the wind system prior to the wave measurements. The matter cannot be resolved without coincident wave and current profile measurements, but it seems probable that the correct values lie between the corrected and uncorrected curves for each U/c_p in figures 10.9 and 10.10. In any case, near the spectral peak $0.8 < \omega/\omega_p < 1.6$, the estimates of ak are not greatly affected by the drift current. Here we find that the moderately and strongly developed cases are more or less uniformly steep, while the nearly fully-developed case reaches its maximum steepness at about twice the peak frequency.

The lowest value of U/c_p (= 1.1) represents nearly fully-developed waves. The steepness at the peak, where there is very little direct wind input and wave-wave interaction effects are not strong in this case (Dungey and Hui, 1979) is negligible. However, at $\omega/\omega_p \approx 2.2$ the steepness increases to a value somewhere between the maxima of the other two curves. Evidently near full development the wind input at frequencies somewhat above the peak is relatively large compared to that of the peak. If wind input determines the maximum steepness then there should be a consistent relationship between maximum steepness and local U/c. Figure 10.11 supports this idea and indicates that under generation conditions somewhere in the spectrum there are quite steep waves ak > 0.25 even when the spectrum is near full development. It seems likely that the wind input is concentrated here, and as the wind picks up the area of maximal steepness moves towards the peak. In §11 we shall explore some aspects of the directional distribution which are consistent with the above observations. Figure 10.10 suggests that, except for the nearly fully-developed case ($U/c_p = 1.1$), the steepness drops off markedly above $\omega = 1.8\ \omega_p$. This is consistent with the idea of peak enhancement (figure 8.3) in which the spectral levels at a particular frequency can be largest when that frequency is the peak frequency.

This occurs when the peak enhancement factor γ exceeds $e^{5/4} = 3.49$. The values of γ corresponding to the three curves of figure 10.10 are, in order of increasing U/c_p, 2.4, 3.7 and 5.8.

The spectral levels of frequencies above the peak are only weakly fetch dependent, therefore one may regard them as the result of a balance between the source terms: wind input, wave-wave interaction and dissipation.

10.6 Root Mean Square Slope

The root mean square (rms) slope, defined as rms surface elevation times wave-number of energy peak, is tabulated in Table 10.1. If the spectrum were a delta spike these rms slopes would correspond to $ak/\sqrt{2}$ values. In this context the ak values deduced from the phase speed based on Stokes model are a factor of 5 larger. Furthermore, the ak values for all strongly generated cases ($U/c_p >$ 2) in field and laboratory approach the theoretical limit in the energy containing region. If the energy containing waves show amplitude dispersion corresponding to maximum steepness, why then is the rms slope relatively small? One possible explanation is that the wave energy at any given frequency is intermittent in time, or that the surface is disturbed, not by an infinite sum of infinitesimally steep uncorrelated sinusoids, but by short groups of steep waves of various frequencies propagating independently. This might be thought of in terms of a random collection of "Stokes" groups which sum to yield the observed spectrum.

At U/c_p values above 2 we find that the energy containing waves are individually maximally steep, yet increasing the generation rate (U/c_p) yields a corresponding increase in the rms slope (Table 10.1) and the peak enhancement factor (figure 8.5) increases until finally limited by rapid breaking - all of this unaccompanied by much change in the steepness of the energy containing waves as reflected in the amplitude dispersion (figures 10.7 and 10.10). If the surface is

TABLE 10.1. RMS SLOPES OF FIELD DATA

Year	Symbol	U	ω_p	$\overline{\zeta^2}$	U/c_p	Significant Slope	rms Slope
	Units	m/s	rad/s	cm^2		%	
1976	Run						
	305093	7.2	2.13	173	1.57	0.97	0.061
	305094	7.1	1.99	161	1.45	0.82	0.051
	339063	7.2	2.20	216	1.61	1.15	0.073
	339064	7.6	2.13	222	1.65	1.10	0.069
	342163	8.6	2.27	126	1.97	0.94	0.059
	342164	8.7	2.27	130	1.70	0.95	0.060
	356123	11.6	2.15	368	2.52	1.44	0.090
	356124	11.5	2.09	379	2.44	1.38	0.087
	362053	6.0	1.77	165	1.08	0.65	0.041
	362054	5.7	1.78	142	1.03	0.61	0.038
1977	006003	5.7	2.32	87	1.34	0.81	0.051
	006004	5.5	2.32	80	1.29	0.78	0.049
	119013	6.7	2.26	91	1.55	0.79	0.050
	119014	7.0	2.26	102	1.61	0.84	0.053
	128173	15.4	2.27	220	3.55	1.24	0.078
	128174	15.2	2.31	213	3.61	1.26	0.079
	128203	13.3	1.95	281	2.64	1.03	0.065
	128204	12.7	2.15	294	2.76	1.29	0.081

composed of a collection of maximally steep 'Stokes" groups then these observations could only result from an increase in length or frequency of such groups having carrier frequencies in the energy containing region of the spectrum. Figure 10.12 is a collection of time series of surface elevation for various U/c_p values, in which the ordinate is in slope units, i.e., surface elevation times theoretical wave-number of the spectral peak k_p $(= \omega_p^2/g)$*, and the time axis is normalized by the peak frequency ω_p. It is immediately apparent that, apart from the nearly fully-developed case $(U/c_p = 1.1)$, the largest waves have comparable slopes approaching the Stokes limit of 0.4. Since the spectrum falls off rapidly with increasing frequency, these steepest waves are closely identified with the spectral peak. The striking difference between the various cases is that as U/c_p is increased the rate of occurrence of maximally steep waves increases until at high U/c_p most of the energy is due to such waves. At the other limit $(U/c_p = 1.1)$, we see that the steepness of the largest waves (still the waves at the spectral peak) is only about 0.2, in keeping with the earlier deductions from measured phase speed (figure 10.10).

*The use of the theoretical value rather than the measured k_p accentuates the steepness of the steepest waves since amplitude dispersion yields $k_p < \omega_p^2/g$.

11. DIRECTIONAL DISTRIBUTIONS OF WAVE ENERGY

11.1 Introduction

Although a full description of the sea surface spectrum is most directly stated in terms of the wave-number frequency or three-dimensional spectrum $X(\underset{\sim}{k},\omega;\ \underset{\sim}{x},t)$, traditionally and for computational simplicity the polar or frequency direction spectrum $F(\omega,\theta;\ \underset{\sim}{x},t)$ (defined by Eq. 2.25) finds most frequent use in application to wave forecasting and engineering calculations. So much so that F is often called the directional spectrum. Here we distinguish between the derived frequency direction spectrum $F(\omega,\theta)$ and the wave-number frequency spectrum $X(\underset{\sim}{k},\omega)$ which is the basic product of our experimental method. The description of the sea surface in terms of the polar spectrum F implies a known or assumed dispersion relation, $\omega = G(k)$ allowing a one-to-one correspondence between frequency and wave-number magnitude, so that in any observed frequency band the spectral energy is taken to fall on a corresponding wave-number band leaving only the direction of travel θ to be specified. Generally, the linear theory dispersion relation (1.1) is assumed and the description of the spectral energy evolution becomes:

$$\frac{\partial F}{\partial t} + v_i \frac{\partial F}{\partial x_i} = I + W + D \qquad (11.1)$$

where $v_i = d\omega/dk_i = (g/2\omega).(k_i/k)$ is the deep water group velocity under the assumption of the linear theory dispersion relation. On the right hand side are the source functions: wind input I, nonlinear interaction, W and dissipation D.

We have seen that the linear theory dispersion relation, while not strictly applicable especially near the peak, is not a bad

approximation in general for natural waves. However, we have shown that amplitude dispersion according to Stokes' theory improves the approximation. The important slope parameter ak has been shown (§10) to be a function of U/c_p and ω/ω_p. Therefore, one may now replace the assumption of the linear theory dispersion (1.1) with the more accurate approximation (2.8) provided U/c_p is known. In §8 we have described the frequency spectrum; in §10 we have described the dispersion relation; we now turn our attention to a description of the directional distribution of wave energy in terms of the spreading function, $h(\theta)$.

In this section we will concern ourselves entirely with the description of natural (field) directional spectra. Two examples of the two-dimensional directional spectrum are shown in figures 11.1 and 11.2 for quite different vaues of U/c_p; 1.5 and 3.1 respectively. These are derived from the wave-number spectra of figures 6.1 and 6.2 respectively in the manner described in §7.1. The ordinates are not in relative scale but the frequency spectrum $\Phi(\omega)$ is shown in figures 6.1 and 6.2. A measure of the level of confidence of the polar spectrum is given by the dashed line. This is the nominal standard deviation of $F(\omega_n,\theta)$ obtained from the original standard deviations of the point energy density distribution E_m by averaging in the same way as $F(\omega_n,\theta)$ has been obtained from E_m. The implied assumption is therefore that the errors are perfectly correlated and

$$\mathrm{Var}\ (a + b) = [\ \sqrt{\mathrm{Var}(a)} + \sqrt{\mathrm{Var}(b)}\ ]^2 \tag{11.2}$$

rather than

$$\mathrm{Var}\ (a + b) = \mathrm{Var}(a) + \mathrm{Var}(b). \tag{11.3}$$

Note that the first assumption is the more conservative of the two.

The polar spectra are predominantly unimodal and tend to be more or less symmetrical about their peaks. The most obvious features are the difference between wave propagation direction and wind direction near the peak and the directional broadening with increasing frequency above the peak. The first has been discussed in §9 and

figures 11.1 and 11.2 demonstrate that with increasing frequency the mean wave direction becomes more and more closely aligned with the wind - a reflection of the short relaxation time of the short waves and hence their insensitivity to the distant fetch distribution. The second has been noticed by previous authors (Longuet-Higgins et al. 1963, Mitsuyasu et al. 1975, Hasselmann et al. 1973, Hasselmann et al. 1980) and attempts have been made to parameterize the spreading function in various ways. Currently, perhaps because most published directional spectra have been obtained from pitch-roll buoys, the most popular parametric description is based on the $\cos^{2s}(\theta/2)$ form first suggested by Longuet-Higgins et al. 1963. Unfortunately, attempts to tie down the behaviour of the s parameter have led to disagreement rather than concensus in spite of the fact that the best known attempts to parameterize s have all been based on floating buoys. In the following we will explore the behaviour of s and compare our results with previous work. Finding that $\cos^{2s}(\theta/2)$ does not describe our results adequately we will propose another description. In order to investigate the shape variability of our polar spectra without forcing them into a pre-selected mold, the two-parameter (L, θ_A) fit described in §7.2 was applied to the individual polar spectra (dotted line in figures 11.1 and 11.2). The tabulated L, θ_A pairs could then be used to reconstruct the best fit spectra for comparison with favoured models.

11.2 L and θ_A Dependence

In figures 11.3a, b and c may be found scatter plots of the L and θ_A dependence for values of ω/ω_p in the ranges of 0.90 to 1.1, 1.1 to 1.25 and 1.25 to 2.

Figure 11.3a indicates that for frequencies near the peak, there is a remarkable grouping of the shape parameters along the line

$$L = \frac{(\theta_A - 45°)}{25} \qquad 45 < \theta_A < 70° \qquad (11.4)$$

There are no instances of double or triple peaks in this data and the fitting bounds ($\theta_a < 90°$, $L > -1.39$) are not approached. This set of shapes may therefore be regarded as a reliable guide to the energy distribution near the peak frequency. The position along this line is probably due to the frequency variation within the band $0.9<\omega/\omega_p<1.1$ and may be determined by relating the s_2 parameter to the half height widths ($\theta_{1/2}$) implied by L and θ_A. For $L = 0$, $\theta_A = 45°$ the half height width is 17.5° while for $L = 1$, $\theta_A = 70°$, the half height width is 31°. These values correspond to s parameters of 29.6 and 9.4 respectively.

However, to a lesser extent in figure 11.3b and to a greater in figure 11.3c the distribution of shape paraemters lies in a wide band between $L = 5$, $\theta_A = 55°$ and $L = 0.1$, $\theta_A = 90°$ say. The implied shape distributions are either relatively narrow with double peaks ($\theta_{1/2} = 52.5°$, $s_2 = 3.2$) or wide with single peaks ($\theta_{1/2} = 32.8°$, $s_2 = 8.3$).

This variation and scatter in the results is felt to be due to the reduction in resolution of the analysis method for these large values of ω/ω_p (for which the energy content is small and the wave-number generally large).

The occurrence of double and triple peaks in these data is therefore not felt to be statistically significant, and indeed examination of individual polar plots indicates that double peaks are often fitted due to the skewness of the energy distribution.

11.3 The s Parameter

Mitsuyasu et al. (1975) were the first to present a reasonably comprehensive set of estimates for s_1 using measurements obtained from a cloverleaf buoy. They presented a plot of s against U/c and showed that although there was good clustering for points on the rear face of the spectrum the points on the front face did not cluster.

Subsequently, Hasselmann et al. (1980) using measurements made from a pitch-roll buoy confirmed this behaviour, but also showed that, when plotted against the relative frequency, the front face

($\omega/\omega_p < 1$) could also be made to cluster. This result, that the width distribution of the spectrum is apparently independent of the wind strength, was attributed by Hasselmann et al. to the dominance of wave-wave interaction over wave generation effects, a point which we will discuss further in §11.6.

Their estimates for s_1 were obtained using the first two Fourier coefficients for $F(\omega_n, \theta)$ as follows

$$F(\omega_n, \theta) = \Phi(\omega_n)\left(\frac{1}{2} + a_1 \cos\theta + b_1 \sin\theta\right) \tag{11.5}$$

$$r_1 = \sqrt{a_1^2 + b_1^2} \tag{11.6}$$

$$s_1 = \frac{r_1}{(1 - r_1)} \tag{11.7}$$

The Fourier coefficients a_1 and b_1 were obtained from the spectrum of the two orthogonal wave slopes:

$$\begin{aligned} \eta_x &= \iint F(\omega, \theta)\, k \cos\theta \, d\theta \, d\omega \\ \eta_y &= \iint F(\omega, \theta)\, k \sin\theta \, d\theta \, d\omega \end{aligned} \tag{11.8}$$

and the assumption of the linear dispersion relation

$$\omega^2 = gk$$

Note that a delta function distribution for

$$F(\omega, \theta) = \Phi(\omega)\, \delta(\theta - \bar{\theta}) \tag{11.9}$$

yields $r_1 = 1$ and $s_1 = \infty$, thus for narrow distributions s_1 is very sensitive to the width.

In figure 11.4 may be found our results for s, which we denote s_2, calculated in the same way from the first two Fourier coefficients of the observed polar energy distribution. However, the linear dispersion relation has not been used to derive the polar spectrum. The parameter s_2 shows the same sort of dependence on ω/ω_p as noted by Hasselmann et al. (1980) and the separate curves, grouped according to U/c_p, indicate that smaller s_2 values (wider spreads) are associated with higher U/c_p values. Since for a given spectrum ω/ω_p is proportional to U/c, this amounts to a dependence on U/c as reported by both Mitsuyasu et al. (1975) and Hasselmann et al. (1980). The fitted lines to both forward and rear spectral faces given by Hasselmann et al. (1980) are indicated on figure 11.4. While the dependence on ω/ω_p is qualitatively similar, Hasselmann et al. (1980) report generally smaller values of s_2, corresponding to broader spectra. Note that their data fall within the range $1 < U/c_p < 2$, so that comparison of their regression lines with the top curve of figure 11.4 is appropriate. In this range of U/c_p the results of Mitsuyasu et al. (1975) and Hasselmann et al. (1980) are in mutual agreement and suggest generally broader spectra than those reported here (figure 11.4). We attribute this difference to the use by Hasselmann et al. (1980) and Mitsuyasu et al. (1975) of the linear dispersion relation which amounts to replacing $F(\omega, \theta)$ by $F_0(\omega, \theta)$ (see §2). Near the peak their values of s are about 9 while ours are about 27. Thus the values of r_1 corresponding to these two values are: Hasselmann et al. (1980) $r_1 = 9/10 = 0.90$; present analysis, $r_2 = 27/28 = 0.964$. This implies a 6.6% underestimate by Hasselmann et al. (1980) producing a factor of 3 change in s. Such an underestimate would arise if the true dispersion relation were

$$\omega^2 = gk(1 + \varepsilon) \tag{11.10}$$

where ε is positive as shown in §10. Their assumption of $\varepsilon = 0$ results in a^1 and b^1 being underestimated by a factor of $1/(1 + \varepsilon)$.

In terms of the phase speed, a 6.6% underestimate of r corresponds to a 3.5% increase in phase speed above the value assumed by Hasselmann et al. (1980). From figure 10.9 we see that such values near the peak are quite characteristic of the observed dispersion relation in the range of U/c_p between 1 and 2.

Evidently the value of s is quite sensitive to the assumed dispersion relation and the effect of amplitude (Stokes) dispersion is to broaden the spectra calculated on the assumption of the linear dispersion relation. It is also possible that the information contained in only the first few Fourier coefficients is insufficient to describe narrow directional spectra.

In order to test the appropriateness of various models of directional spread we have reduced the rather cumbersome and untidy set of directional spectra to a set of (L, θ_A) pairs based on a least squares fit of our quite flexible test model to the observed spreading functions. In practice one's interest in the directional spread is generally focussed on the 'energy containing' region. That is, the peak value and width at, say, half height are of more interest than the width of the tails of the spreading function. We may compute a value of s (which we will call s_3) which matches the half-height half-width $\theta_{1/2}$ of the test (L, θ_A) model with that of the Mitsuyasu type spreading function:

$$\cos^{2s_3}\left(\frac{\theta_{1/2}}{2}\right) = 0.5 \qquad (11.11)$$

where $\theta_{1/2}$ is the angle at which the height of the test model is one half its central height.

The estimates of s_3 obtained in this way (figure 11.5) are much less scattered than those of s_2. Furthermore, the stratification with U/c_p has disappeared, leaving the spreading function dependent only on ω/ω_p. The reduced scatter implies that the half-height width is a more stable description of the spreading than the first Fourier coefficients. The reason for this is probably that the half-height width is determined by the energy containing, and thus

less noisy, part of the distribution; whereas the first Fourier coefficients are affected by the entire distribution. Possibly the tails of the directional spread are more influenced by changes in U/c than the peak. In principle, energy from the wind will enter the distribution out to $\theta = \cos^{-1} c/U$; while the peak of the directional spread, at least on the rear face of the frequency spectrum, is limited by dissipative processes and wave-wave interaction, i.e. processes less sensitive to U/c.

A further check of the appropriateness of the $\cos^{2s}(\theta/2)$ spreading function is graphed in figure 11.6. This figure compares the peak value of the test (L,θ_A) model (abscissa) with the peak of the $\cos^{2s}(\theta/2)$ distribution (ordinate). The peaks are consistently too high by about 10%. Based on this data set, it would seem that the $\cos^{2s}(\theta/2)$ spreading function is consistently in error in estimating the wave energy in the peak direction.

11.4 The $\cos^{2m}\theta$ Spreading Function

The property of the $\cos^{2s}(\theta/2)$ distribution, that it is non-negative over the complete range of θ, is not necessary to describe the present data set wherein there were no measured polar distributions more than π in total width. If, indeed, previously reported wider distributions for wind-generated seas are really a consequence of inadequate angular resolution of the detection method, then the physically more appealing $\cos^{2m}\theta$ distribution might be more appropriate. On the edges of the distribution, where the energy density is quite low, wave-wave interaction cannot be important and it is difficult to imagine any input from the wind at angles greater than $\cos^{-1} c/U$ from the mean wind direction. Of course fluctuations in wind direction could broaden the distribution, but these are generally of the order of ±10° for the steady wind conditions being considered here.

Apart from the question of which type of distribution ($\cos^{2s}(\theta/2)$ or $\cos^{2m}\theta$) is the more physically appealing, they are not significantly different in terms of goodness of fit to the data. Appropriate choices of s and m render them virtually indistinguishable. Thus the $\cos^{2m}\theta$ distribution suffers from the same peakiness complaint as the $\cos^{2s}(\theta/2)$ (see figure 11.7).

11.5 The $\text{Sech}^2(\beta\theta)$ Spreading Function

The failure of the various cosine distributions to model the observed polar distributions accurately has led us to consider yet another. The three-dimensional evolution of freely-propagating, second-order Stokes gravity wave groups (Hui & Hamilton, 1979, Hui, 1980) indicates that an envelope soliton group propagating around the main wave direction is described by a hyperbolic secant. The distribution of wave energy in the direction transverse to the main wave direction behaves therefore like sech^2. Since the envelope solitons survive interactions (Hui, 1979, 1980, Zhakarov, 1968), it seems not unreasonable to assume that the wave field consists of only (envelope) soliton groups. Then the directional distribution of the waves observed at a given point about the main wave direction must follow approximately a $\text{sech}^2(\beta\theta)$ distribution, at least for small θ.

This suggestion from theory led to the testing of a spreading function for the distribution of energy (amplitude squared) of the form $\text{sech}^2(\beta\theta)$. The hyperbolic secant squared shape is preserved and the width of the spectral spread is determined by the parameter β. The dependence of β on ω/ω_p, from fitting to the half-height width of the test model, is graphed on logarithmic axes in figure 11.8. Here again, as in figure 11.5, the data for various values of U/c_p collapse onto a single average curve. In fact, in this sense there is little to choose between the $\cos^{2s_3}(\theta/2)$ and the $\text{sech}^2(\beta\theta)$ distributions. However, a comparison of the peak values of the test model with the peak values of the $\text{sech}^2(\beta\theta)$ distribution (figure 11.9) indicates that the $\text{sech}^2(\beta\theta)$ distribution

models the peak of the spreading function rather more faithfully than the various cosine distributions (figures 11.6 and 11.7). In fact, the average overestimate of the wave energy in the peak direction is now only 2% for the $\text{sech}^2\ (\beta\theta)$ distribution rather than 10% for the $\cos^{2s}\ (\theta/2)$ distribution.

Of course, the $\text{sech}^2\ (\beta\theta)$ distribution extends beyond $\pm\pi/2$ and as already remarked our observed polar spectra were contained within this angular region. However, values of β were generally larger than 1.3 so that at $\pm\pi/2$ the spreading function is less than 7% of its peak value and less than 4% of the energy is outside of the range $-\pi/2 < \theta < \pi/2$. The narrowness of the spectra and the rapid (exponential) drop-off of the spreading function can be conveniently employed in treating the $\text{sech}^2\ (\beta\theta)$ distribution for numerical modelling or engineering calculations since little error is introduced in using the limits $\pm\infty$ rather $\pm\pi$ and the advantages of integrability are considerable.

In figure 11.8 the dashed lines are a convenient representation of β:

$$\beta = 2.44 \left(\frac{\omega}{0.95\ \omega_p}\right)^{+1.3} \quad ; \quad 0.56 < \frac{\omega}{\omega_p} < 0.95$$

$$\beta = 2.44 \left(\frac{\omega}{0.95\ \omega_p}\right)^{-1.3} \quad ; \quad 0.95 < \frac{\omega}{\omega_p} < 1.6 \qquad (11.12)$$

$$\beta = 1.24 \qquad \text{otherwise}$$

The range of directional spread given by (11.12) is illustrated in figure 11.10. From the narrowest to the widest our wind-generated spectra expand by about a factor of 2.

11.6 Dependence on ω/ω_p

Hasselmann et al. (1980) have previously noted that the spreading function is more sensitive to ω/ω_p than to U/c. They argue that this implies that nonlinear interactions are more important than direct wind input in establishing the spectral shape. Our observations strengthen and extend theirs in that we find that the spreading function is adequately described by ω/ω_p alone in the U/c_p and ω/ω_p ranges of $1 < U/c_p < 4$; $0.8 < \omega/\omega_p < 1.6$. However, we caution against the use of this result to establish which of the three source functions, wind input, nonlinear interactions and dissipation, is dominant in establishing the spectral shape of the rear face. It seems likely that all three source functions will depend on both U/c and ω/ω_p since, as we have shown, steepness is affected by both of these and all three source functions are steepness dependent.

In view of the dominance of ω/ω_p in the description of the spreading function it would not be suprising to find that its effect is felt in the frequency spectrum as well. In fact, the broadening of the directional spectrum away from the peak tends to whiten the frequency spectrum. This is, in effect, the behaviour of the rear face noted in §8. Recall that the rear face of the frequency spectrum was shown to depend on

$$\omega^{-4}\,\omega_p^{-1} \cdot \alpha\left(\frac{U}{c_p}\right) = \omega^{-5} \cdot \frac{\omega}{\omega_p} \cdot \alpha\left(\frac{U}{c_p}\right)$$

This empirical result could be realized by simple dimensional considerations if the peak frequency and wind speed are included in the list of relevant parameters: Φ_R, g, U, ω, ω_p; where Φ_R (ω) is the energy density on the rear face of the spectrum. Appropriate non-dimensional groups of these parameters are: $\Phi_R\,\omega^5/g^2$, ω/ω_p, U/c_p and the spectrum is of the form:

$$\Phi_R(\omega) = g^2 \omega^{-5} \cdot G\left(\frac{\omega}{\omega_p}, \frac{U}{c_p}\right)$$

The measurements described in §8 reveal that:

$$G\left(\frac{\omega}{\omega_p}, \frac{U}{c_p}\right) = \frac{\omega}{\omega_p} \cdot \alpha\left(\frac{U}{c_p}\right)$$

11.7 The Directional Spread of the Forward Face

It has been reported (Mitsuyasu et al. 1975 and Hasselmann et al. 1980) that the spectra tend to be most narrow near the peak frequency. While this is true of our data as well (figures 11.1 and 11.2), we note that the maximum in our β or s values (figures 11.4 and 11.8) is displaced slightly but distinctly to the low frequency side of the peak frequency at about $\omega/\omega_p = 0.95$. In other words, the narrowest spreads occur on the forward face of the frequency spectrum. As mentioned in §2, Hasselmann et al. (1973) first showed that the growth of the forward face of the wind-wave spectra can be attributed to nonlinear wave-wave interactions; a conclusion that was further substantiated by the analytical calculations of Dungey and Hui (1979) for narrow spectra. This implies that the shape (and hence the angular spreading) of the three-dimensional wave spectrum $X(\underset{\sim}{k}, \omega)$ for $\omega < \omega_p$ must be predominantly determined by the energy transfer due to nonlinear wave-wave interactions, the (direct) energy input from the wind and the energy loss due to whitecapping being relatively unimportant in this region. Systematic calculations by Dungey and Hui show that the energy transfer rate of a typical narrow wind-wave spectrum is of the shape given in figure 11.11. It is seen that there is a highly concentrated energy gain at wave-number slightly below k_p and in the mean wave direction. This may be responsible for the smallest angular spread occurring at a frequency slightly below the peak frequency since wind input, perhaps due to random pressure fluctuations (Phillips 1957), would broaden the spectrum somewhat away from the area of strong nonlinear transfer. Some support for this

explanation is provided by the numerical calculations of Sell and Hasselmann (1972) reported in Hasselmann et al. (1973) for the mean JONSWAP spectrum, in which the positive peak of the nonlinear transfer occurs at about $\omega/\omega_p = 0.95$ or just where we observe the narrowest directional distributions.

12. CONCLUDING REMARKS

Based on the idea of Barber (1963), a numerical method has been developed for computing the three-dimensional wind-generated wave spectrum X ($\underset{\sim}{k}$, ω) from an array of wave staffs. Essentially, the method applies the known array transfer function to the observed wave-number spectrum to reveal the actual wave-number spectrum. Wave records were obtained from a tower in Lake Ontario, commanding fetches of 1.1 km to 300 km, and from the CCIW wind-wave flume at fetches of 50 m. The array consisted of 14 wave staffs and extended over 28 m in the lake and 1 m in the laboratory. Based on the analysis of 84 steady-state runs from the lake and 7 from the laboratory, covering a range of wind speed to peak wave speed ratio (U/c_p) of from 0.8 to 17, the following general conclusions are drawn.

The rear face or equilibrium range of the frequency spectra in both field and laboratory conditions is well described by an ω^{-4} ω_p^{-1} law for $1.5 < \omega/\omega_p < 3.5$. Accordingly, a new (modified JONSWAP) parametric spectral distribution is proposed, and the new equilibrium range and peak enhancement parameters (α and γ) are found to be functions of U/c_p. The ω^{-4} ω_p^{-1} = $\omega^{-5} \cdot (\omega/\omega_p)$ law is shown to follow from dimensional considerations.

One consequence of this spectral shape is that the energy density of the waves at a fixed frequency in the equilibrium range (wavelengths of 6 cm to 10 m for these data) will depend on wind speed to a power between 0.55 and 1.0 as conditions change from strongly generating to full development.

The peak wave and wind directions are often quite different and the difference was correlated with the fetch gradient in the wind direction. An empirical formula based on a similarity argument is given which explains the observed difference between wave and wind directions. The formula can be used as a predictive tool in deducing steady-state wave directions from meteorological records.

In general, the observed phase speeds under natural conditions are slightly in excess of the linear dispersion relation

for infinitesimal amplitude waves. The excess is satisfactorily explained by the amplitude dispersion effects of the Stokes' wave. Significant energy was detected in the bound harmonics of the laboratory waves. Within the accuracy of these measurements bound harmonics could not be detected in the field data, although they must exist to produce the observed amplitude dispersion. From the laboratory data it was demonstrated that the ratio of the energy in the bound harmonics to the free waves at twice the peak frequency increases with U/c_p. Beyond $U/c_p = 9.0$ it exceeds unity, i.e. bound harmonics dominate the spectrum near $\omega/\omega_p = 2$.

The angular spreading of wave energy is found to be smallest at a frequency ω_s slightly less than the peak frequency ω_p. The spreading increases both as ω increases and decreases from ω_s. The spreading is best described by $\text{sech}^2\ (\beta\theta)$ in which β is found to depend solely on ω/ω_p.

Emerging from this is a rather tidy description of the wind-generated wave spectrum, in which the energy level at any frequency depends on the position of that frequency in the spectrum (ω/ω_p) and on the intensity of wind input U/c, while the directional spreading is related only to ω/ω_p.

We reproduce here our description of the wind-generated deep water directional spectrum in a form amenable to immediate application in wave forecasting and engineering design calculations:

$$F\ (\omega,\theta) = \frac{1}{2}\,\Phi\ (\omega)\ \beta\ \text{sech}^2\ \beta\ \{\theta - \bar{\theta}\ (\omega)\} \tag{12.1}$$

where $\bar{\theta}$ is the mean wave direction and

$$\beta = \begin{cases} 2.61\ \left(\frac{\omega}{\omega_p}\right)^{+1.3} & ; \quad 0.56 < \frac{\omega}{\omega_p} < 0.95 \\ 2.28\ \left(\frac{\omega}{\omega_p}\right)^{-1.3} & ; \quad 0.95 < \frac{\omega}{\omega_p} < 1.6 \\ 1.24 & ; \quad \text{otherwise} \end{cases} \tag{12.2}$$

The frequency spectrum is:

$$\Phi(\omega) = \alpha\, g^2\, \omega^{-5} \left(\frac{\omega}{\omega_p}\right) \exp\left\{ -\frac{5}{4} \left(\frac{\omega_p}{\omega}\right)^4 \right\} . \gamma^{\exp\left\{-22\left(\frac{\omega}{\omega_p} - 1\right)^2\right\}} \tag{12.3}$$

$$\alpha = 0.006 \left(\frac{U_c}{c_p}\right)^{0.55} \tag{12.4}$$

where U_c is the component of the average 10 m wind in the mean direction of the waves at the peak of $\Phi(\omega)$.

$$\gamma = \begin{cases} 2.2 & ; \quad 0.83 < \dfrac{U_c}{c_p} < 1 \\ 2.2 + 7.7 \log_{10} \left(\dfrac{U_c}{c_p}\right) & ; \quad 1 \leq \dfrac{U_c}{c_p} < 6 \end{cases} \tag{12.5}$$

Finally, the third order Stokes' dispersion relation has been verified:

$$\omega^2 = gk \left\{ 1 + (ak)^2 \right\} \tag{12.6}$$

where the U/c_p and frequency-dependent values of ak may be gleaned from figure 10.10.

APPENDIX

DETAILS OF THE DIRECTIONAL SPECTRUM ANALYSIS METHOD

Algorithm for Choosing Inversion Points

The algorithm for choosing the locations $\underset{\sim}{k}_m$ of (4.7), at which the energy is assumed to lie, is based on the transfer function $M(\underset{\sim}{k})$ having a strong maximum value at $\underset{\sim}{k} = 0$. Thus we proceed as follows:

1. The raw energy is calculated using (4.10) at 41 x 57 equally spaced points in $-\pi < k_x, k_y < \pi$.
2. We find a list of at most 25 locations $\underset{\sim}{k}_\ell$, at which $\xi(\underset{\sim}{k})$ rises to within 75% of its maximum value. It would seem reasonable that there is directional energy at these points because of the nature of $M(\underset{\sim}{k})$.
3. A least squares fit is performed to explain the observed $\xi(\underset{\sim}{k})$.
4. If less than 92.5% of the variance of $\xi(\underset{\sim}{k})$ is explained then further searches are made until either a total of 100 points are used or 92.5% is explained.
5. Since the order of performing the fitting may influence the values of E_m, a refit is then performed (in batches not exceeding 50 points) to eliminate this bias. This step adds considerably to the computation time required.

Note that in this algorithm no use is made of any dispersion relation.

Technique for Least Squares Fitting

Performing the differentiations of (4.8) we obtain the equations

$$\sum_{\ell=1}^{N_E} E_\ell \, \overline{M(\underset{\sim}{k} - \underset{\sim}{k}_m) \, M(\underset{\sim}{k} - \underset{\sim}{k}_\ell)} = \overline{\xi(\underset{\sim}{k}) \, M(\underset{\sim}{k} - \underset{\sim}{k}_m)} \tag{A.1}$$

where the overbar denotes the appropriate average over D and N_E is the number of fitting locations. These m simultaneous equations may be used to obtain estimates for the E_ℓ; however, the calculations of the product terms

$$M(\underset{\sim}{k} - \underset{\sim}{k}_m) \, M(\underset{\sim}{k} - \underset{\sim}{k}_\ell) \tag{A.2}$$

would be exceedingly lengthy if calculated directly. We are able to demonstrate the equivalence of (A.1) with (4.10), considerably shortening the necessary calculations. Thus we note that

$$\exp(i \, \underset{\sim}{k}.\underset{\sim}{r}) = \begin{cases} 1 & \underline{r} = 0 \\ 0 & \underline{r} = \text{integer vector} \end{cases} \tag{A.3}$$

whence using

$$M(\underset{\sim}{k}) = \sum_\ell \exp(-i \, \underset{\sim}{k}.\underset{\sim}{r}) \tag{A.4}$$

we obtain

$$\overline{M(\underset{\sim}{k} - \underset{\sim}{k}_m) \, M(\underset{\sim}{k} - \underset{\sim}{k}_\ell)} = \sum_s \sum_t \exp(i \, \underset{\sim}{k}_m.\underset{\sim}{r}_s + i \, \underset{\sim}{k}_\ell.\underset{\sim}{r}_s) \, \overline{\exp(-i \, \underset{\sim}{k}.(\underset{\sim}{r}_s + \underset{\sim}{r}_t))}$$

$$= M(\underset{\sim}{k}_\ell - \underset{\sim}{k}_m) \tag{A.5}$$

similarly

$$\xi(\underset{\sim}{k})\ M(\underset{\sim}{k} = \underset{\sim}{k}_m) = \sum_s \sum_t \exp(i\ \underset{\sim}{k}_m . \underset{\sim}{r}_t)\ \overline{\exp(-i\ \underset{\sim}{k}.(\underset{\sim}{r}_s + \underset{\sim}{r}_t))\ (\underset{\sim}{r}_s)}$$

$$= \xi(\underset{\sim}{k}_m) \tag{A.6}$$

and (A.1) is equivalent to (4.10) or

$$\sum_m E_m\ M(\underset{\sim}{k}_n - \underset{\sim}{k}_m) = \xi(\underset{\sim}{k}_n). \tag{A.7}$$

<u>Confidence Limits</u>

In common with other least squares fitting methods, confidence limits can be derived from the coefficients of the inverse matrix C^{nm} (say), where

$$E_m = C^{nm}\ \xi(\underset{\sim}{k}_n) \tag{A.8}$$

or

$$\sum_n M(\underset{\sim}{k}_n - \underset{\sim}{k}_m)\ C^{nr} = \delta_{rm} \tag{A.9}$$

However, as will become apparent, the degree of freedom is not that associated with the 2337 points at which $\xi(\underset{\sim}{k}_n)$ is calculated but rather the 165 values at which ρ is known. Thus the $\rho(r_i)$, $i = 1 \ldots 165$ are perturbed by independent complex random variables ε^i of zero mean and width,

$$E_x\ (\varepsilon^i\ \varepsilon^{*j}) \begin{cases} = \sigma^2, & i = j \\ = 0, & i \neq j \end{cases} \tag{A.10}$$

where E_x is the expected value. These errors ε^i, which represent the sources of unexplained variance induce errors σ_m (say) in the E_m, where from (A.8) and (A.9)

$$\delta^n \delta^\ell = C^{mn} C^{\ell r} \{ \sum_i \varepsilon^i \exp(-i \underset{\sim}{k}_m . \underset{\sim}{r}^i) \} \{ \sum_j \varepsilon^j \exp(-i \underset{\sim}{k}_r . \underset{\sim}{r}^j) \} \quad (A.11)$$

Now using

$$\sum_j \varepsilon^j \exp (-i \underset{\sim}{k}_r . \underset{\sim}{r}^j) = \sum_j \varepsilon^{*j} \exp (i \underset{\sim}{k}_r . \underset{\sim}{r}^j) \quad (A.12)$$

where * denotes the complex conjugate (since ξ is always real) we obtain

$$E_x (\delta^n \delta^\ell) = \sigma^2 C^{\ell n} \quad (A.13)$$

Thus knowing the inverse matrix and σ^2 we can obtain directly the variances of the estimates for the E_m. Now we observe residual errors in $\xi(\underset{\sim}{k})$

$$\gamma(\underset{\sim}{k}) = \xi(\underset{\sim}{k}) - \sum E_m M(\underset{\sim}{k} - \underset{\sim}{k}_m) \quad (A.14)$$

where E_m is given by A.7. Whence

$$E_x \overline{(\gamma(\underset{\sim}{k})^2)} = E_x [\sum_i \rho^i \rho^{i*} - \sum_n E_n \xi(\underset{\sim}{k}_n)] = \sigma^2 (N_\rho - N_E) \quad (A.15)$$

Where N_ρ is the number of locations at which ρ is estimated (165) and N_E is the number of fitting locations. This equation can be used to estimate σ^2 from the residual errors and hence give estimates for the variances of E_m.

Modification at High Frequencies

As will be appreciated from (A.15) we cannot choose $N_E \geq N_\rho$, thus we are limited to 164 (in fact we use no more than 100) independent parameters to describe the directional spectrum. For wave-numbers bigger than 0.4 π however we have to consider progressively coarser arrays of possible locations $\underset{\sim}{k}_\ell$ representing $E(\underset{\sim}{k})$ in the form

$$E = \sum_{m=1}^{N_E} E_m \sum_i W_i \, \delta(\underset{\sim}{k} - \underset{\sim}{k}_m - \underset{\sim}{s}_i)$$

where the locations are grouped around $\underset{\sim}{k}_m$ with associated weights W_i (see Table A.1). The weights are chosen so that unit values of E_m at all the available locations $\underset{\sim}{k}_m$ will result in energy density in D or rather unit delta functions at all the 2337 points of the underlying grid.

Possibilities for Improvement

In the present method of calculating $\xi(\underset{\sim}{k})$, no allowance has been made at the higher frequencies for the relatively greater accuracy with which $\rho(\underset{\sim}{r})$ is known at smaller separations $\underset{\sim}{r}$ than for large separations. This is because after the arguments of Hamilton, Hui and Donelan (1979) the correlation function decays quickly with $\underset{\sim}{r}$ giving greater prominence to the underlying errors.

Thus weights should be applied to the $\rho(\underset{\sim}{r})$ decreasing with $\underset{\sim}{r}$. These weights will in turn imply a smoother masking function $M(\underset{\sim}{k})$. If the energy is then represented with shape functions $S(\underset{\sim}{k})$ say (analogous to the delta functions used here) which have dimensions comparable to the resolution implied by the $M(\underset{\sim}{k})$, then the fitting functions implied by

$$\xi(\underset{\sim}{k}) = \sum_m E_m \int S(\underset{\sim}{k}^*) \, M(\underset{\sim}{k}_m - \underset{\sim}{k}^*) \, d^2 \underset{\sim}{k}^*$$

will be even smoother than the already smoothed $M(\underset{\sim}{k})$. Hence the fitting process might become extremely sensitive. These arguments also hold in part for the unweighted $\rho(\underset{\sim}{r})$ used here, and this is why we have used the perhaps intuitively unattractive delta functions as shape functions. For the weighted $\rho(\underset{\sim}{r})$ there is however the additional point that the simplified form of the product

$$\overline{M(\underset{\sim}{k} - \underset{\sim}{k}_m)\, M(\underset{\sim}{k} - \underset{\sim}{k}_n)}$$

no longer holds, instead we have

$$\overline{M(\underset{\sim}{k} - \underset{\sim}{k}_m)\, M(\underset{\sim}{k} = \underset{\sim}{k}_n)} = M_2\,(\underset{\sim}{k}_m - \underset{\sim}{k}_n)$$

where M_2 is the masking function associated with weights $W_2(\underset{\sim}{r})$ say which are the square of the weights used for the $M(\underset{\sim}{k})$

$$M(\underset{\sim}{k}) = \sum W\,(\underset{\sim}{r}_n)\, \exp\,(-i\, \underset{\sim}{k}.\underset{\sim}{r}_n)$$

$$M_2(\underset{\sim}{k}) = \sum W^2\,(\underset{\sim}{r}_n)\, \exp\,(-i\, \underset{\sim}{k}.\underset{\sim}{r}_n)$$

The necessity for calculating separate $M(\underset{\sim}{k})$ and $M_2(\underset{\sim}{k})$ for each frequency will also increase either the computation or the storage requirements appreciably. We are therefore of the opinion that in the light of present knowledge the method of analysis adopted has been a reasonable compromise between what would be ideal and what would seem practicable.

TABLE A-1

SMOOTHING LEVELS AND WEIGHTS

LEVEL	FREQUENCIES		WEIGHTS (unnormalized)
0	1-7		*
	0.044 to 0.513 Hz	Field	* 1 *
	0.176 to 2.051 Hz	Laboratory	*
1	8,9		* 1 *
	0.591 to 0.670 Hz	Field	1 4 1
	2.363 to 2.676 Hz	Laboratory	* 1 *
2	10,11,12		1 * 1
	0.748 to 0.904 Hz	Field	1 4 6 4 1
	2.988 to 3.613 Hz	Laboratory	* 6 10 6 *
			1 4 6 4 1
			1 * 1
3	13,14,15		1 1
	0.982 to 1.139 Hz	Field	1 4 6 4 1
	3.926 to 4.551 Hz	Laboratory	1 * 11 16 11 * 1
			1 4 11 24 32 24 11 4 1
			6 16 32 64 32 16 6
			1 4 11 24 32 24 11 4 1
			1 * 11 16 11 * 1
			1 4 6 4 1
			1 1

Note: "*" indicates the nearest available location for additional energy.
Unit energy at all available locations will give a uniform energy distribution.

REFERENCES

Airy, G. B., 1845. "Tides and Waves". Art. 192 in Encyc. Metrop.

Banner, M. L. and Phillips, O. M., 1974. "On Small Scale Breaking Waves". J. Fluid Mech., 65, pp. 647-657.

Barber, N. F., 1963. "The Directional Resolving Power of an Array of Wave Recorders". Ocean Wave Spectra, Englewood Cliffs, N. J., Prentice-Hall Inc., pp. 137-150.

Barnett, T. P. and Kenyon, K. E., 1975. "Recent Advances in the Study of Wind Waves". Rep. Prog. Phys. 38, pp. 667-729.

Birch, K. N., Harrison, E. J. and Beal, S., 1976. "A Computer-Based System for Data Acquisition and Control of Scientific Experiments on Remote Platforms". Proc. Ocean' 76 Conf., Washington, D. C.

Borgman, L. E., 1979. "Directional Wave Spectra from Wave Sensors". In Ocean Wave Climate, Plenum Press, New York, pp. 269-300.

Brooke Benjamin, T., 1967. "The Instability of Periodic Wavetrains in Nonlinear Dispersive Systems". Proc. Roy. Soc. A, 299, pp. 59-75.

Burling, R. W., 1959. "The Spectrum of Waves at Short Fetches". Dtsch. Hydrogr. Z, 12, pp. 45-64, 96-117.

Cartwright, D. E. and Smith, N. D., 1964. "Buoy Techniques for Obtaining Directional Wave Spectra". Trans. 1964 Buoy Technology Symposium, Marine Technology Soc., Washington, D. C.

Cote, L. J., Davis, J. O., Marks, W., McGough, R. J., Mehr, E., Pierson, W. J. Jr., Ropek, J. F., Stephenson, G. and Vetter, R. C., 1960. "The Directional Spectrum of Wind-Generated Sea as Determined from Data Obtained by the Stereo Wave Observation Project". Meteor. Pap. NYU, College of Engineering, 2, No. 6, 88 pp.

Davis, R. E. and Regier, L., 1977. "Methods for Estimating Directional Wave Spectra from Multi-element Arrays". J. Mar. Res. 35, pp. 453-477.

Der, C. Y. and Watson, A. S., 1977. "A High-Resolution Wave Sensor Array for Measuring Wave Directional-Spectra in the Nearshore Zone". Proc. Ocean'77 Conf., Los. Angeles, Calif.

Donelan, M. A., 1978. "Whitecaps and Momentum Transfer". In Turbulent Fluxes Through the Sea Surface, Wave Dynamics and Prediction, Plenum Press, pp. 273-287.

Dungey, J. C. and Hui, W. H., 1979. "Nonlinear Energy Transfer in a Narrow Gravity-Wave Spectrum". Proc. Roy. Soc. Lond. A, 368, pp. 239-265.

Ewing, J. A., 1969. "Some Measurements of the Directional Wave Spectrum". J. Mar. Res., 27, pp. 163-171.

Fontanel, A. and DeStaerke, D., 1980. "Spectres directionnels de vagues en mer du Nord. Images du radar de SEASAT. Climatologie de la mer, Conference internationale, Paris, 363-383.

Forristall, G. Z., 1981. "Measurements of a Saturated Range in Ocean Wave Spectra". J. Geophys. Res., 86, C9, pp. 8075-8084.

Forristall, G. Z., Ward, E. G., Cardone, V. J. and Borgman, L. E., 1978. "The Directional Spectra and Kinematics of Surface Gravity Waves in Tropical Storm Delia". J. Phys. Oceanogr., 8, pp. 888-909.

Fox, M.J.H., 1976. "On the Nonlinear Transfer of Energy in the Peak of a Gravity-Wave Spectrum". Proc. Roy. Soc. Lond. A, 348, pp. 467-483.

Garrett, J., 1969. "Some New Observations on the Equilibrium Region of the Wind-Wave Spectrum". J. Mar. Res., 27, pp. 273-277.

Garrett, J., 1970. "Field Observations of Frequency Domain Statistics and Nonlinear Effects in Wind-Generated Ocean Waves". Thesis, University of British Columbia, 176 pp.

Gill, G. C., 1975. "Development and Use of the Gill UVW Anemometer". Boundary-Layer Meteorol., 8, pp. 475-495.

Hamilton, J., Hui, W. H. and Donelan, M. A., 1979. "A Statistical Model for Groupiness in Wind Waves". J. Geophys. Res., 84, C8, pp. 4875-4884.

Hasselmann, K., 1962. "On the Nonlinear Energy Transfer in a Gravity Wave Spectrum. Part 1". J. Fluid Mech., 12, pp. 481-500.

Hasselmann, K., 1963a. "On the Nonlinear Energy Transfer in a Gravity Wave Spectrum. Part 2". J. Fluid Mech. 15, pp. 273-281.

Hasselmann, K., 1963b. "On the Nonlinear Energy Transfer in a Gravity Wave Spectrum. Part 3". J. Fluid Mech., 15, pp. 385-398.

Hasselmann, D. E., Dunckel, M. and Ewing, J. A., 1980. "Directional Wave Spectra Observed During JONSWAP 1973". Jour. Phys. Oceanogr. 10, pp. 1264-1280.

Hasselmann, K., Barnett, T. P., Bouws, E., Carlson, H., Cartwright, D. E., Enke, K., Ewing, J. A., Gienapp, H., Hasselmann, D. E., Kruseman, P., Meerburg, A., Müller, P., Olbers, D. J., Richter, K., Sell, W., and Walden, H., 1973. "Measurements of Wind-Wave Growth and Swell Decay during the Joint North Sea Wave Project (JONSWAP)". Dtsch. Hydrogr. Z., A8 (Suppl.), No. 12.

Holthuijsen, L. H., 1981. "The Directional Energy Distribution of Wind Generated Waves as Inferred from Stereophotographic Observations of the Sea Surface". Thesis, Delft University of Technology, Report No. 81-2.

Huang, N. E., Long, S. R. and Bliven, L. F., 1981. "On the Importance of Significant Slope in Empirical Wind-Wave Studies". J. Phys. Oceanogr., 10, pp. 569-573.

Huang, N. E., Long, S. R., Tung, C.-C., Yuen, Y. and Bliven, L. 1981. "A Unified Two-Parameter Wave Spectral Model for a General Sea State". J. Fluid Mech., 112, pp. 203-224.

Hui, W. H., 1979. "Exact Envelope-Soliton Solutions of a Two-Dimensional Nonlinear Wave Equation". J. Appl. Math. and Physics (ZAMP) 30, pp. 929-936.

Hui, W. H., 1980. "Three-Dimensional Nonlinear Evolution of Water Waves". In Nonlinear Partial Differential Equations in Engineering and Applied Science, (Ed) Sternberg, R. L., Kalinowski, A. J. and Papadakis, J. S., pp. 167-187.

Hui, W. H. and Hamilton, J., 1979. "Exact Solutions of a Three-Dimensional Nonlinear Schrödinger Equation Applied to Gravity Waves". Journal of Fluid Mechanics, 93, pp. 117-133.

Hui, W. H., and Tenti, G., 1982. "A New Approach to Steady Flows with Free Surfaces". J. Appl. Math. and Physics (ZAMP), 33, pp. 569-589.

Irani, G. B. Gotwols, B. L. and Bjerkaas, A. W., 1981. "Ocean Wave Dynamics Test: Results and Interpretations". Report STD-R-537, The Johns Hopkins University, Applied Physics Laboratory.

Jones, W. L. and Schroeder, L. C., 1978. "Radar Backscatter from the Ocean: Dependence on Surface Friction Velocity". Boundary-Layer Meterol., 13, pp. 133-149.

Jones, W. L., Schroeder, L. C., Boggs, D. H., Bracalente, E. M., Brown, R. A., Dome, G. J, Pierson, W. J. and Wentz, E. J., 1982. "The SEASAT A Satellite Scatterometer: The Geophysical Evaluation of Remotely Sensed Wind Vectors Over the Ocean". J. Geophys. Res., 87, C5, pp. 3297-3317.

Kahma, K. K., 1981. "A Study of the Growth of the Wave Spectrum with Fetch". J. Phys. Oceanogr., 11, pp. 1503-1515.

Kinsman, B., 1960. "Surface Waves at Short Fetches and Low Wind Speed - a Field Study". Chesapeake Bay Inst., Johns Hopkins University, Tech. Report No. 19.

Kinsman, B., 1961. "Some Evidence on the Effect of Nonlinearity on the Position of the Equilibrium Range in Wind-Wave Spectra". J. Geophys. Res., 66 (8), pp. 2411-2415.

Kitaigorodskii, S. A., 1962. "Applications of the Theory of Similarity to the Analysis of Wind-Generated Wave Motion as a Stochastic Process". Bull. Acad. Sci., USSR Geophys. Ser. 1, pp. 105-117.

Kitaigorodskii, S. A., Krasitskii, V. P. and Zaslavskii, M. M., 1975. "On Phillips' Theory of Equilibrium Range in the Spectra of Wind-Generated Grvity Waves". J. Phys. Oceanogr., 5, pp. 410-420.

Komen, G. J., 1980. "Nonlinear Contributions to the Frequency Spectrum of Wind-Generated Water Waves". J. Phys. Oceanogr.

Korvin-Kroukovsky, B. V., 1967. "Further Reflections on Properties of Sea Waves Developing Along a Fetch". Dtsch. Hydrogr., Z, 20, 7.

Lake, B. M. and Yuen, H. C., 1978. "A New Model for Nonlinear Wind Waves. Part 1. Physical Model and Experimental Evidence". J. Fluid Mech., 88, pp. 33-62.

Liu, P. C., 1971. "Normalized and Equilibrium Spectra of Wind Waves in Lake Michigan". J. Phys. Oceanogr., 1, 249.

Longuet-Higgins, M. S., 1969. "On Wave Breaking and the Equilibrium Spectrum of Wind-Generated Waves". Proc. Roy. Soc. Lond. A, 310, pp. 151-159.

Longuet-Higgins, M. S., 1976. "On the Nonlinear Transfer of Energy in the Peak of the Gravity-Wave Spectrum: A Simplified Model". Proc. Roy Soc. A., 347, 311-328.

Longuet-Higgins, M. S., 1977. "Some Effects of Finite Steepness on the Generation of Waves by Wind". In A Voyage of Discovery, Pergamon Press, pp. 393-403.

Longuet-Higgins, M. S., Cartwright, D. E. and Smith, N. D., 1963. "Observations of the Directional Spectrum of Sea Waves Using the Motions of a Floating Buoy". Ocean Wave Spectra, Englewood Cliffs, N.J., Prentice-Hall, Inc., pp. 111-136.

Longuet-Higgins, M. S. and Cokelet, E. D., 1976. "The Deformtion of Steep Surface Waves: I, A Numerical Method of Computation". Proc. Roy. Soc. Lond. A, 350, pp. 1-26.

McLeish, W., Ross, D., Shuchman, R. A. Teleki, P. G. Hsiao, S. V., Shemdin, O. H. and Brown, W. E. Jr., 1980. Synthetic Aperture Radar Imaging of Ocean Waves: Comparison with Wave Measurements". J. Geophys. Res., 85, C9, pp. 5003-5011.

Miles, J. W., 1957. "On the Generation of Surface Waves by Shear Flows". J. Fluid Mech. 3, pp. 185-204.

Mitsuyasu, H., 1968. "On the Growth of the Spectrum of Wind Generated Waves, I." Rep. Res. Inst. Appl. Mech., Kyushu Univ., 16, pp. 459-482.

Mitsuyasu, H., 1969. "On the Growth of the Spectrum of Wind Generated Waves, II." Rep. Res. Inst. Appl. Mech., Kyushu Univ., 17, pp. 235-248.

Mitsuyasu, H., Tasai, F., Suhara, T., Mizuno, S., Ohkuso, M., Honda, T. and Rikiishi, K., 1975. "Observations of the Directional Spectrum of Ocean Waves Using a Cloverleaf Buoy". J. Phys. Oceanogr., 5, pp. 750-760.

Mitsuyasu, H., Kuo, Y.-Y. and Masuda, A., 1979. "On the Dispersion Relation of Random Gravity Waves, Part 2. An experiment". J. Fluid Mech. 92, pp. 731-749.

Pawka, S. S., Hsiao, S. V., Shemdin, O.H. and Inman, D. L., 1980. "Comparisons Between Wave Directional Spectra from SAR and Pressure Sensor Arrays". J. Geophys. Res., 85, C9, pp. 4987-4995.

Phillips, O. M., 1957. "On the Generation of Waves by Turbulent Wind". J. Fluid Mech., 2, pp. 417-445.

Phillips, O. M., 1958. "The Equilibrium Range in the Spectrum of Wind-Generated Waves". J. Fluid Mech., 4, pp. 426-434.

Phillips, O. M., 1960. "On the Dynamics of Unsteady Gravity Waves of Finite Amplitude, Part I". J. Fluid Mech., 9, pp. 193-217.

Phillips, O. M., 1977. The Dynamics of the Upper Ocean. 2nd Edition, Cambridge University Press, Cambridge, 336 pp.

Phillips, O. M. and Banner, M. L., 1974. "Wave Breaking in the Presence of Wind Drift and Swell (1974)". J. Fluid Mech., 66, pp. 625-640.

Pierson, W. J., 1981. "The Variability of Winds Over the Ocean". In Spaceborne Synthetic Aperture Radar for Oceanography. Johns Hopkins University Press, pp. 56-74.

Pierson, W. J. and Moskowitz, L., 1964. "A Proposed Spectral Form for Fully Developed Wind Seas Based on the Similarity Theory of S. A. Kitaigorodskii". J. Geophys. Res., 69, pp. 5181-5190.

Plant, W. J. and Wright, J. W., 1980. "Phase Speeds of Upwind and Downwind Travelling Short Gravity Waves". J. Geophys. Res., 85, C6, pp. 3304-3310.

Ramamonjiarisoa, A., 1973. "Sur l'évolution des spectres d'énergie des vagues de vent a fetchs courts". Mémoires Soc. Roy. Sci. Liège, Ser. 6, 6, 47-66.

Ramamonjiarisoa, A., 1974. "Contribution a l'étude de la structure statistique et des méchanismes de génération des vagues de vent". Thesis, Université de Provence (Inst. Méch. Stat. de la Turbulence, no. A.O. 10023).

Regier, L. A. and Davis, R. E., 1977. "Observation of the Power and Directional Spectrum of Ocean Surface Waves". J. Mar. Res., 35, pp. 433-451.

Rikiishi, K., 1978. "A New Method for Measuring the Directional Wave Spectrum, I. Description". J. Phys. Oceanogr., 8, pp. 508-517.

Rikiishi, K., 1978. "A New Method for Measuring the Directional Wave Spectrum. II. Measurements of the Directional Spectrum and Phase Velocity of Laboratory Wind Waves". J. Phys. Oceanogr., 8, pp. 518-529.

Schuler, D. L., 1978. "Remote Sensing of Directional Gravity Wave Spectra and Surface Currents Using Microwave Dual-Frequency Radar", Radio Science, 13, pp. 321-331.

Sell, W. and Hasselmann, K., 1972. "Computations of Nonlinear Energy Transfer for JONSWAP and Empirical Wind Wave Spectra". Rep. Inst. Geophys., Univ. Hamburg.

Simons, T. J., 1974. "Verification of Numerical Models of Lake Ontario, I. Circulation in Spring and Early Summer". J. Phys. Oceanogr., 4, pp. 507-523.

Simons, T. J., 1975. "Verification of Numerical Models of Lake Ontario, II. Stratified Circulations and Temperature Changes". J. Phys. Oceanogr., 5, pp. 98-110.

Stewart, R. W., 1974. "The Air-Sea Momentum Exchange". Boundary-Layer Meteorology, 6, pp. 151-167.

Stewart, R. H. and Joy, J. W., 1974. "HF Radio Measurements of Surface Currents". Deep-Sea Res., 21, pp. 1039-1049.

Stokes, G. G., 1847. "On the Theory of Oscillatory Waves". Trans. Camb. Phil. Soc., 8, pp. 441-455.

Sturm, G. V. and Sorrell, F. Y., 1973. "Optical Wave Measurement Technique and Experimental Comparison with Conventional Wave Height Probes". Appl. Optics, 12, pp. 1928-1933.

Sutherland, A. J., 1967. "Spectral Measurments and Growth Rates of Wind-Generated Water Waves". Stanford University, Dept. of Civil Eng. Tech. Rep. No. 84, 64 pp.

Toba, Y., 1973. "Local Balance in the Air-Sea Boundary Processes, III. On the Spectrum of Wind Waves". J. Oceanogr. Soc. Japan, 29, pp. 209-220.

Trizna, D. B., Bogle, R. W., Moore, J. C. and Howe, C. M., 1980. "Observation by H. F. Radar of the Phillips Resonance Mechanism for Generation of Wind Waves". J. Geophys. Res., 85, C9, pp. 4946-4956.

Tyler, G. L.,Teague, C. C., Stewart, R. H., Peterson, A. M., Munk, W. H. and Joy, J. W., 1974. "Wave Directional Spectra from Synthetic Aperture Observations of Radio Scatter". Deep-Sea Res., 21, pp. 989-1016.

Webb, D. J., 1978. "Nonlinear Transfers Between Sea Waves". Deep Sea Res., 25, pp. 279-298.

Weismann, D. E., King, D. B. and Thompson, T. W., 1979. "Relationship Between Hurricane Surface Winds and L-Band Radar Backscatter from the Sea Surface". J. Appl. Meteor. 18, pp. 1023-1034.

Whitham, G. B., 1967. "Nonlinear Dispersion of Water Waves". J. Fluid. Mech., 27, pp. 399-412.

Whitham, G. B., 1974. "Linear and Nonlinear Waves". John Wiley and Sons, New York, 636 pp.

Wright, J. W., 1968. "A New Model for Sea Clutter". IEEE Trans. on Antennas and Propagation, AP-16, pp. 217-223.

Wu, J., 1975. "Wind-Induced Drift Currents". J. Fluid Mech., 68, pp. 49-70.

Wu, J., 1977. "Directional Slope and Curvature Distributions of Wind Waves". J. Fluid Mech., 79, pp. 463-480.

Zakharov, V. E., 1968. "Stability of Periodic Waves of Finite Amplitude on the Surface of a Deep Fluid". Soviet Physics J. Appl. Mech. Tech. Phys., 4, pp. 190-194.

Zakharov, V. E., Filonenko, N. N., 1967. "Energy Spectrum for Stochastic Oscillations of the Surface of a Liquid". Soviet Physics-Doklady, 11, pp. 881-883.

ACKNOWLEDGEMENTS

We are indebted to the following members of the staff of the Canada Centre for Inland Waters for support during the preparation, realization and analysis of this experiment: M. Dick and M. Skafel (Management), E. Harrison, H. Savile, W. Gibson, S. Watson, C. Der, B. White, S. Beal, A. Pashley and J. Ford (Engineering), M. Pedrosa, J. Diaz and M. Larocque (technical), J. Carew, B. Macdonald, J. Roe and H. Don (logistics and diving), D. Beesley (data collection and archiving), B. Jones (typing), P. McColl (draughting).

FIGURES

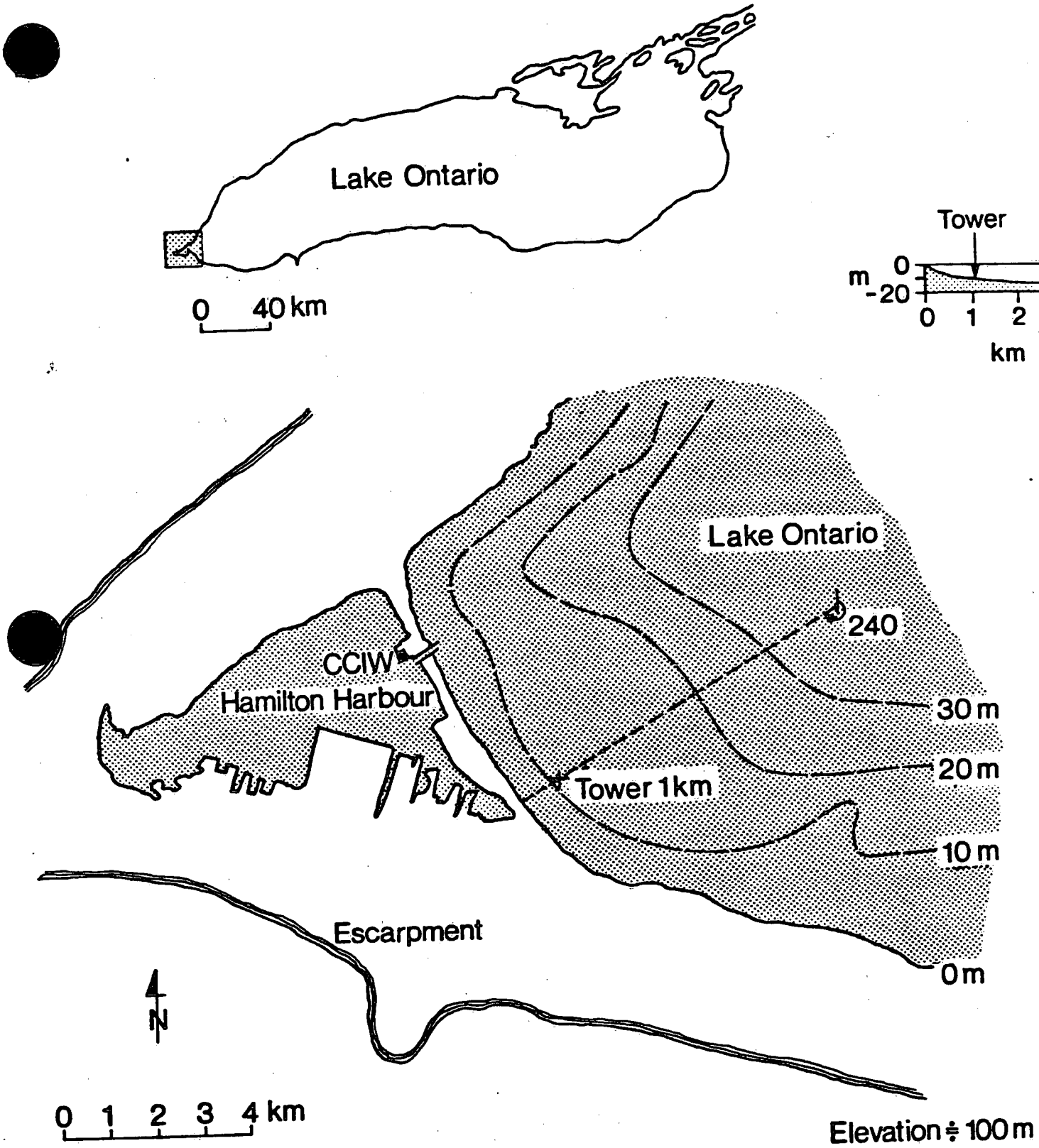

3.1 Map showing the location of the research tower in Lake Ontario and the shore-normal profile in the vicinity of the tower.

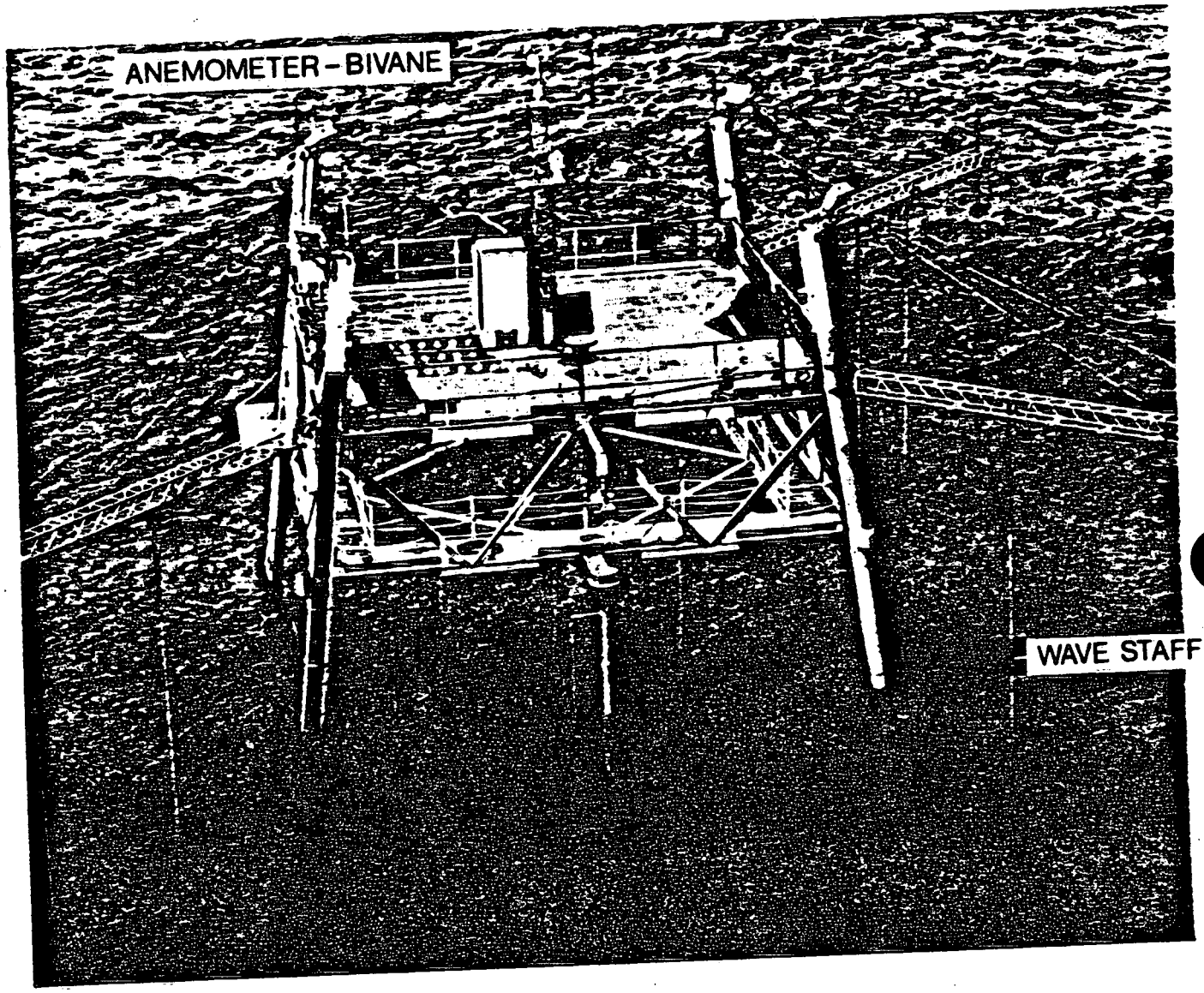

3.2 Photograph of the research tower. The wave staffs can be seen suspended from the tower itself and from its extensions in three directions. Meterological instruments are mounted on a mast at the centre and the measuring and communications devices are housed in the box at the foot of the mast.

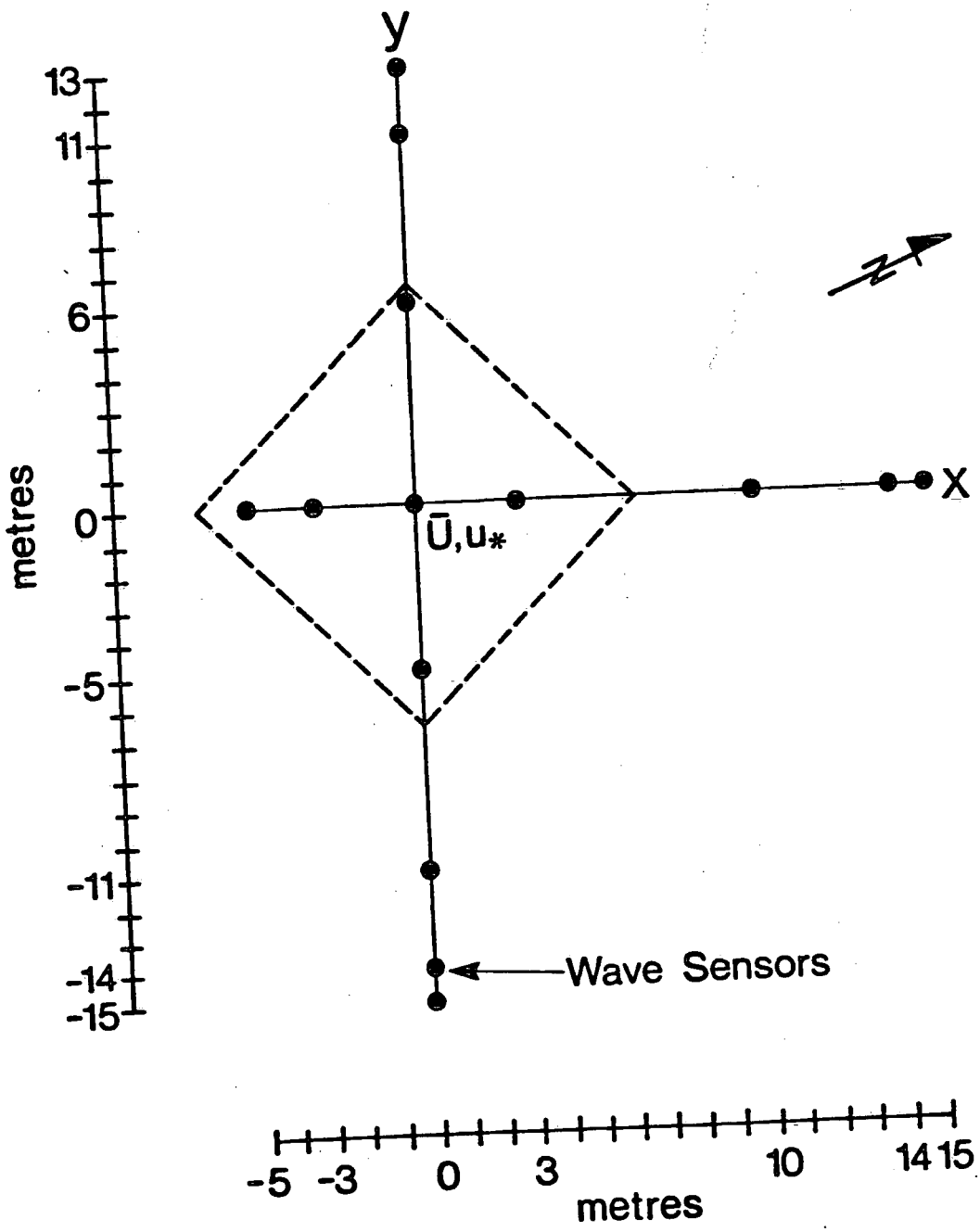

3.3 Location of wave staffs in the array

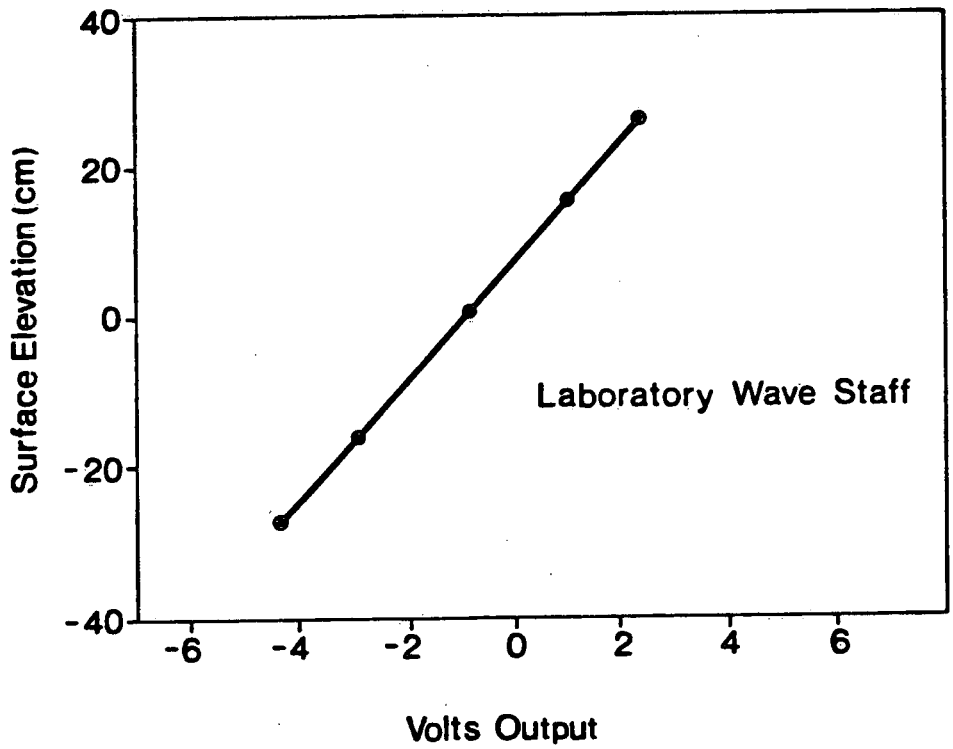

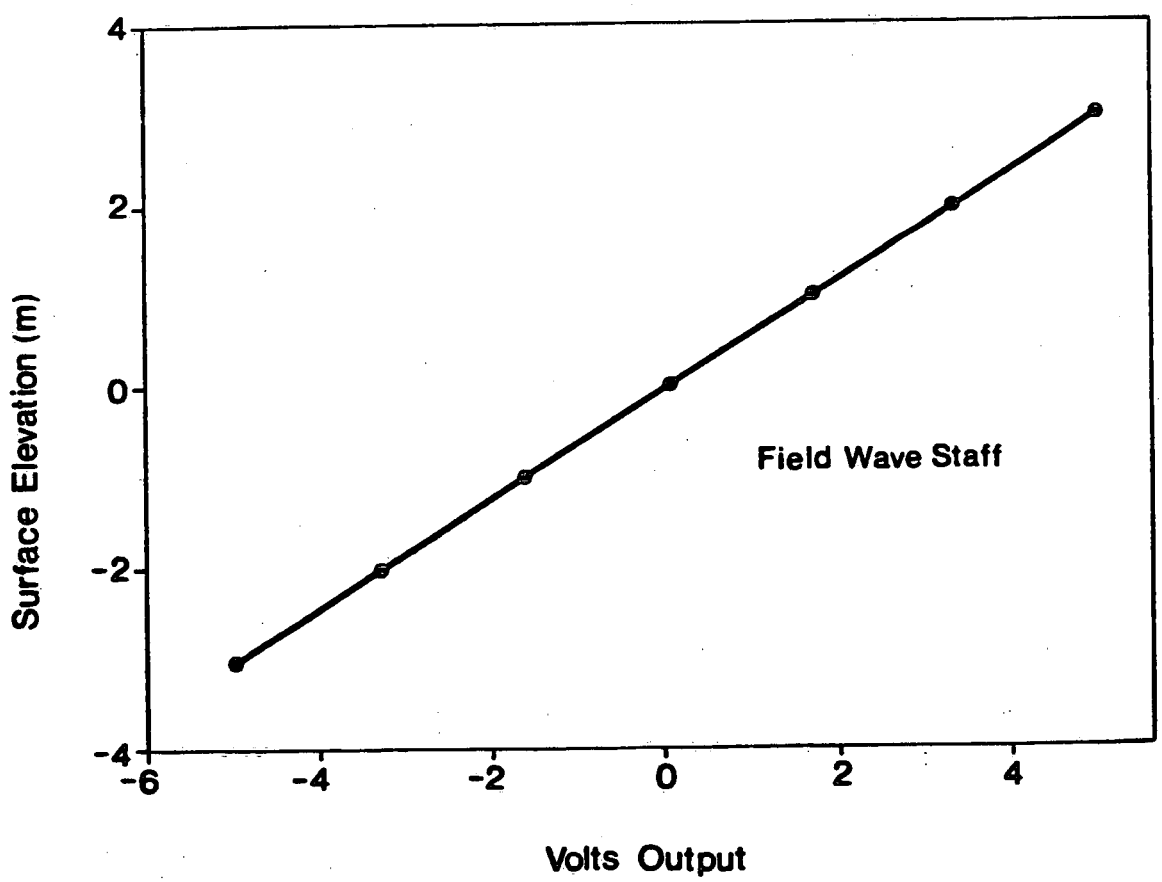

3.4 Typical calibrations of field and laboratory wave staffs.

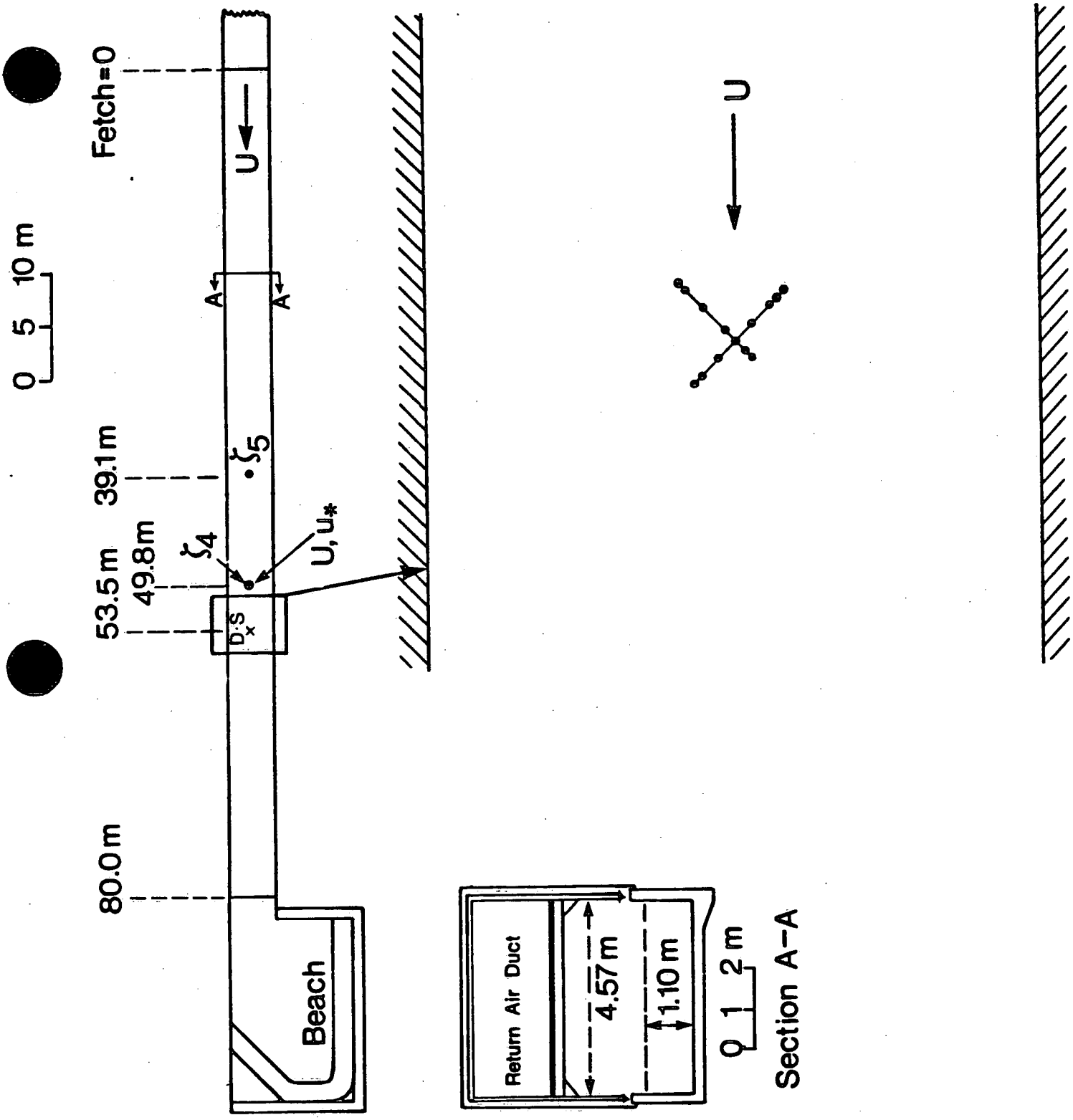

3.5 Plan of the wind-wave flume. The location of the directional wave array is indicated by an X labelled "D.S.". The lower part of the figure shows an enlargement of the directional array and its orientation in the flume.

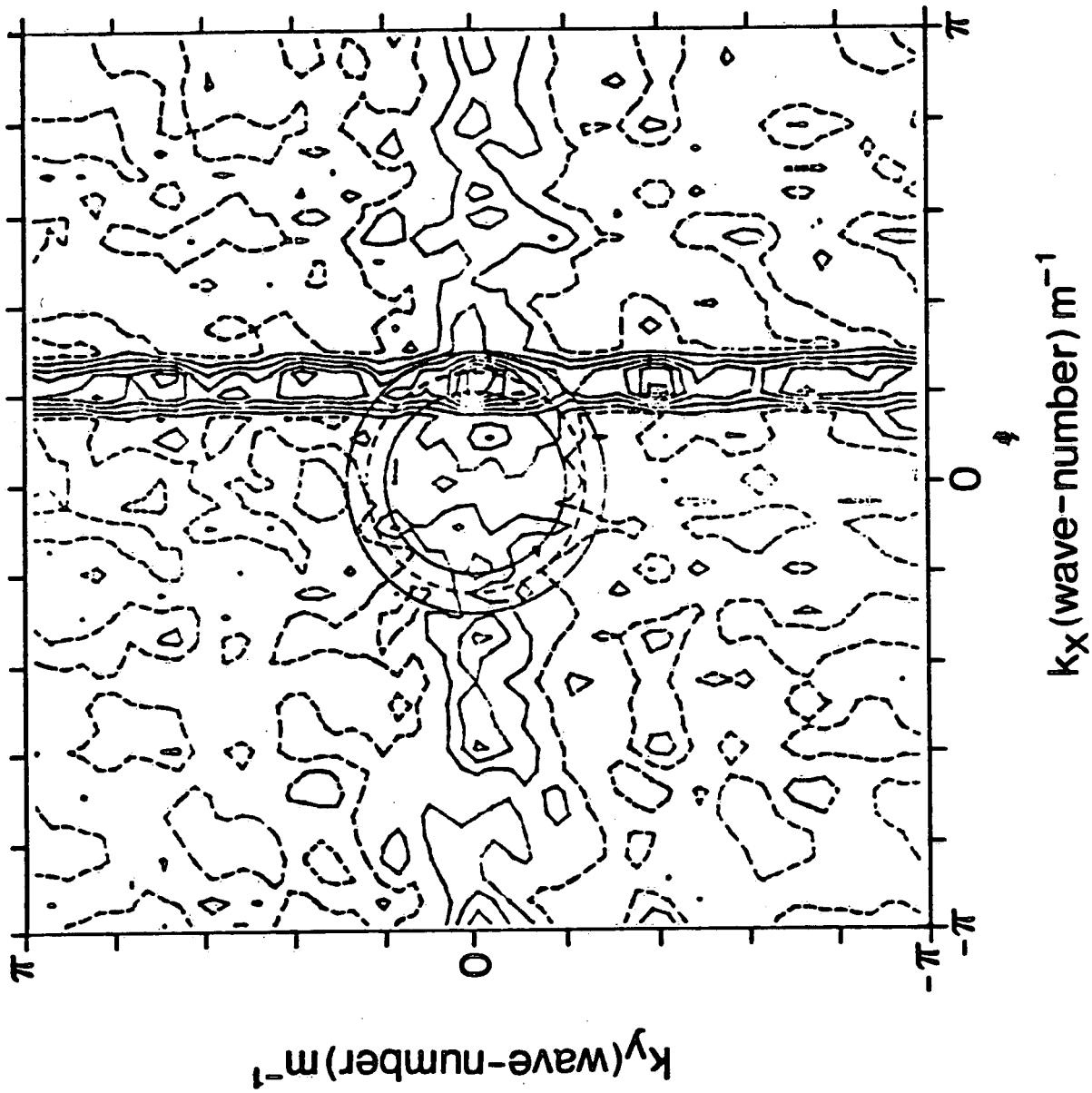

4.1 A typical "raw" or observed wave-number spectrum $\xi(\underset{\sim}{k})$ at $\omega_0 = 2.7$. The contour lines indicate the distribution of wave energy in the wave-number plane. The sign of the contours corresponds to: (———) positive, (—— —— ——) zero, (------) negative, and the contour interval is 1/8th of the maximum value. The full circles represent the limits of the deep water dispersion relation corresponding to the edges of the frequency band analysed, while the broken circle corresponds to the energy-weighted mean frequency of that band.

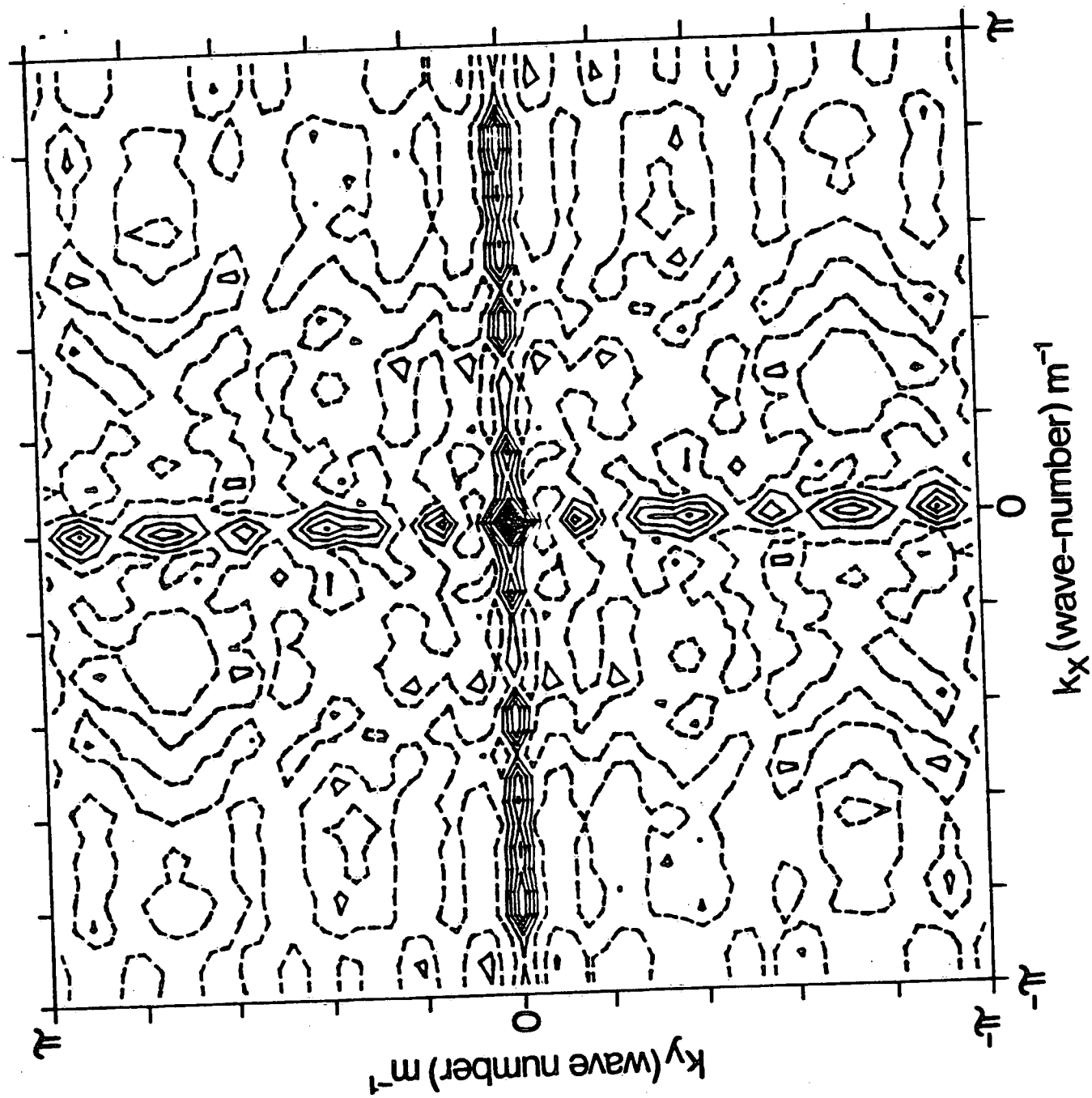

4.2 The transfer function of the 14 staff array of figure 3.3.

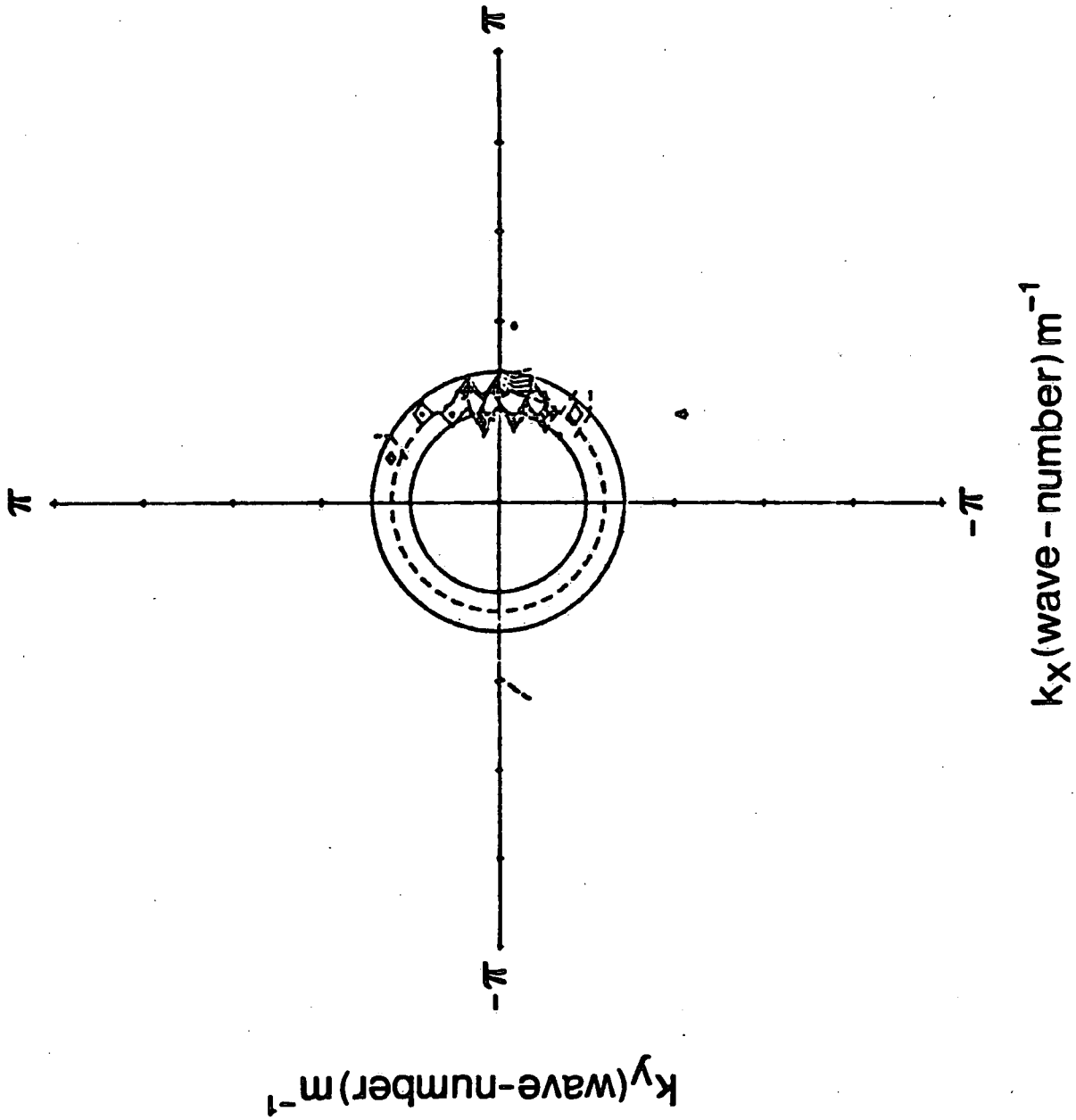

4.3 The "detected" wave-number spectrum X ($\underset{\sim}{k}$) corresponding to the raw spectrum of figure 4.1.

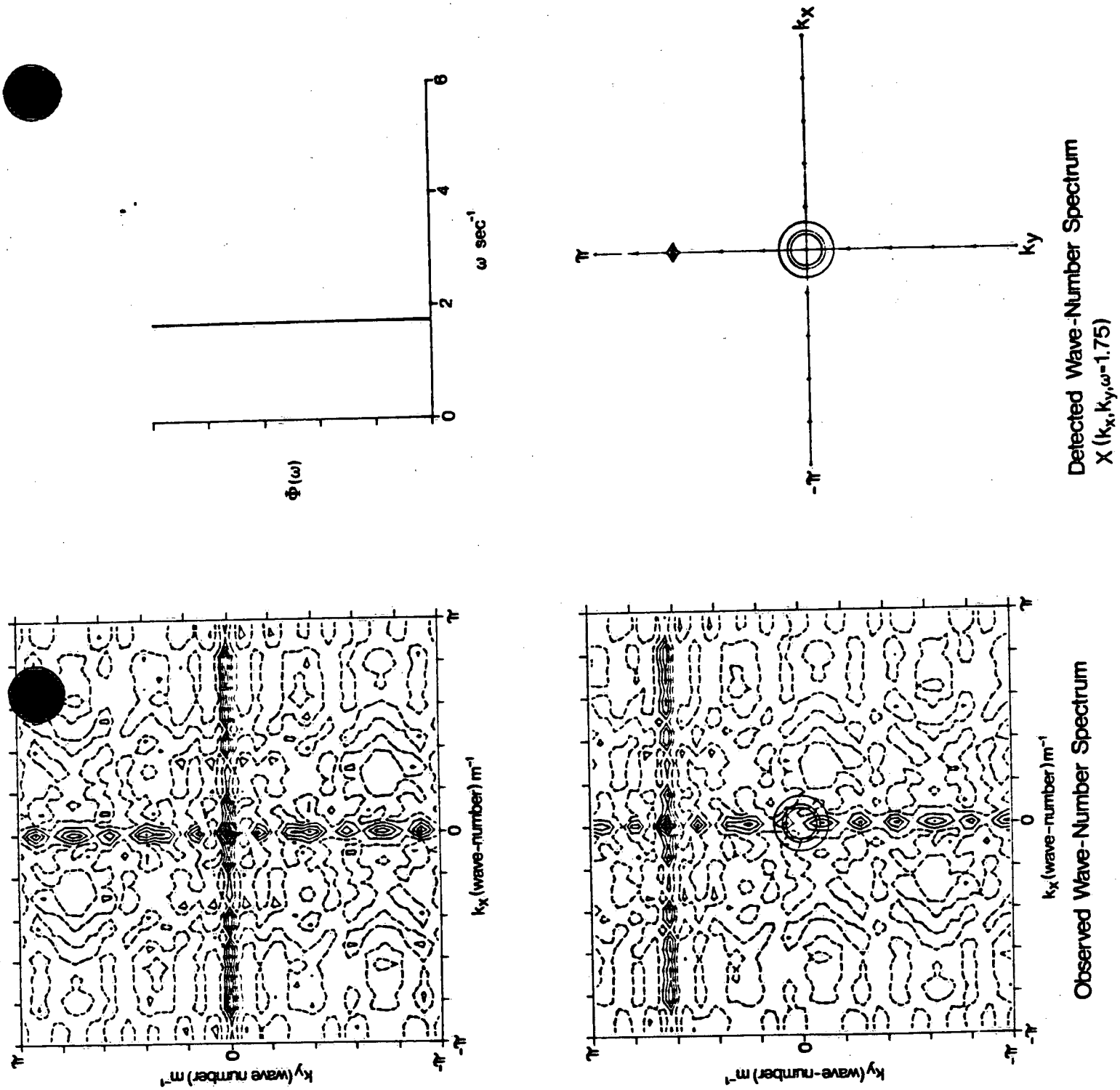

4.4 A composite figure showing the stages in the process of recovering the detected wave-number spectrum $\tilde{X}(k)$. The panels are in counter-clockwise sequence from top-right. In this case the data are simulated and correspond to a monochromatic infinite crested wave train travelling along the y axis. The circles correspond to the dispersion relation (1-1) which does not apply to the simulated data.

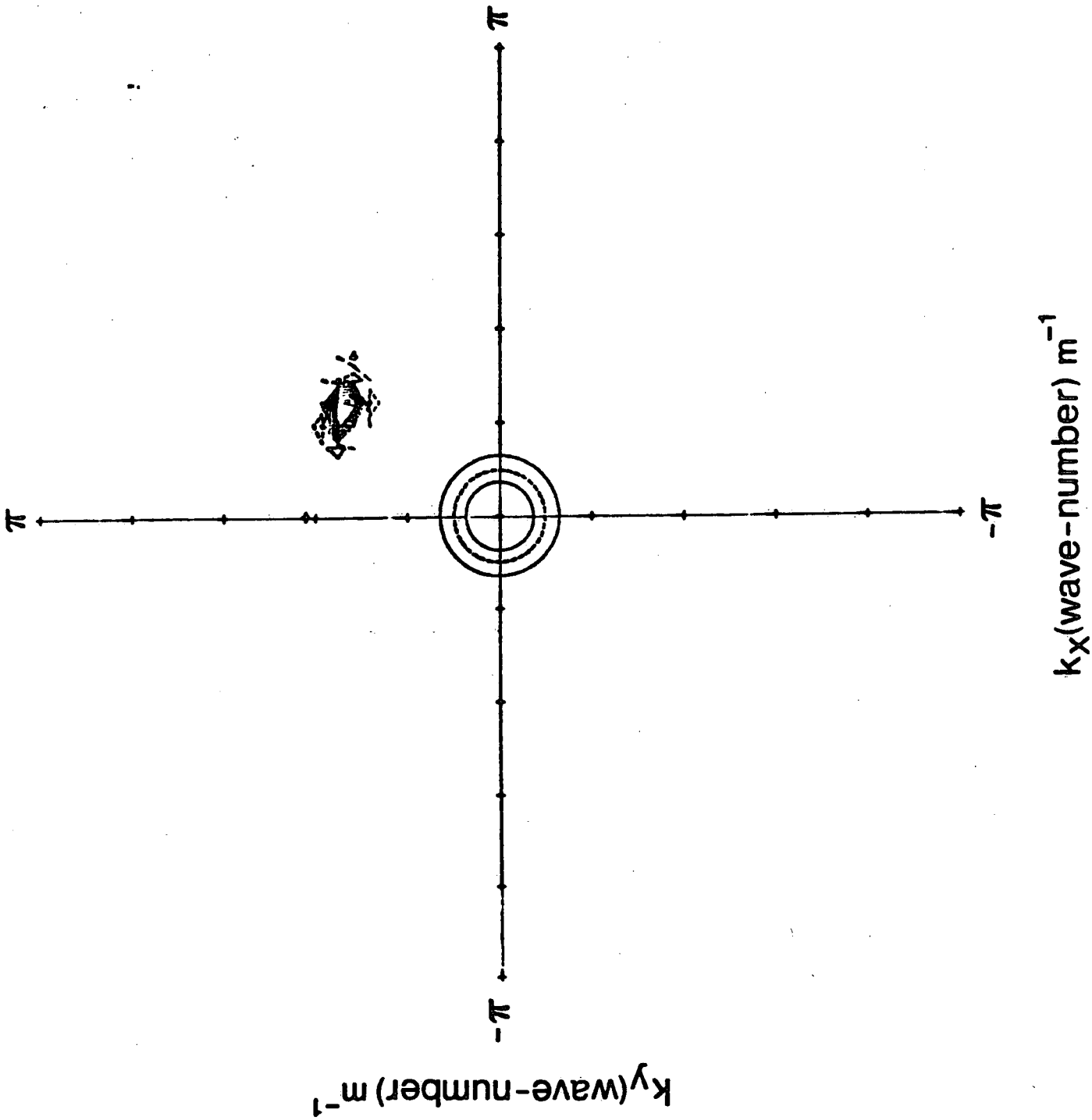

4.5 The detected wave-number spectrum corresponding to a simulated monochromatic infinite crested wave train. The wave-number of this delta function spectrum falls between the grid points described by (4.11), consequently some smearing of the detected spectrum results.

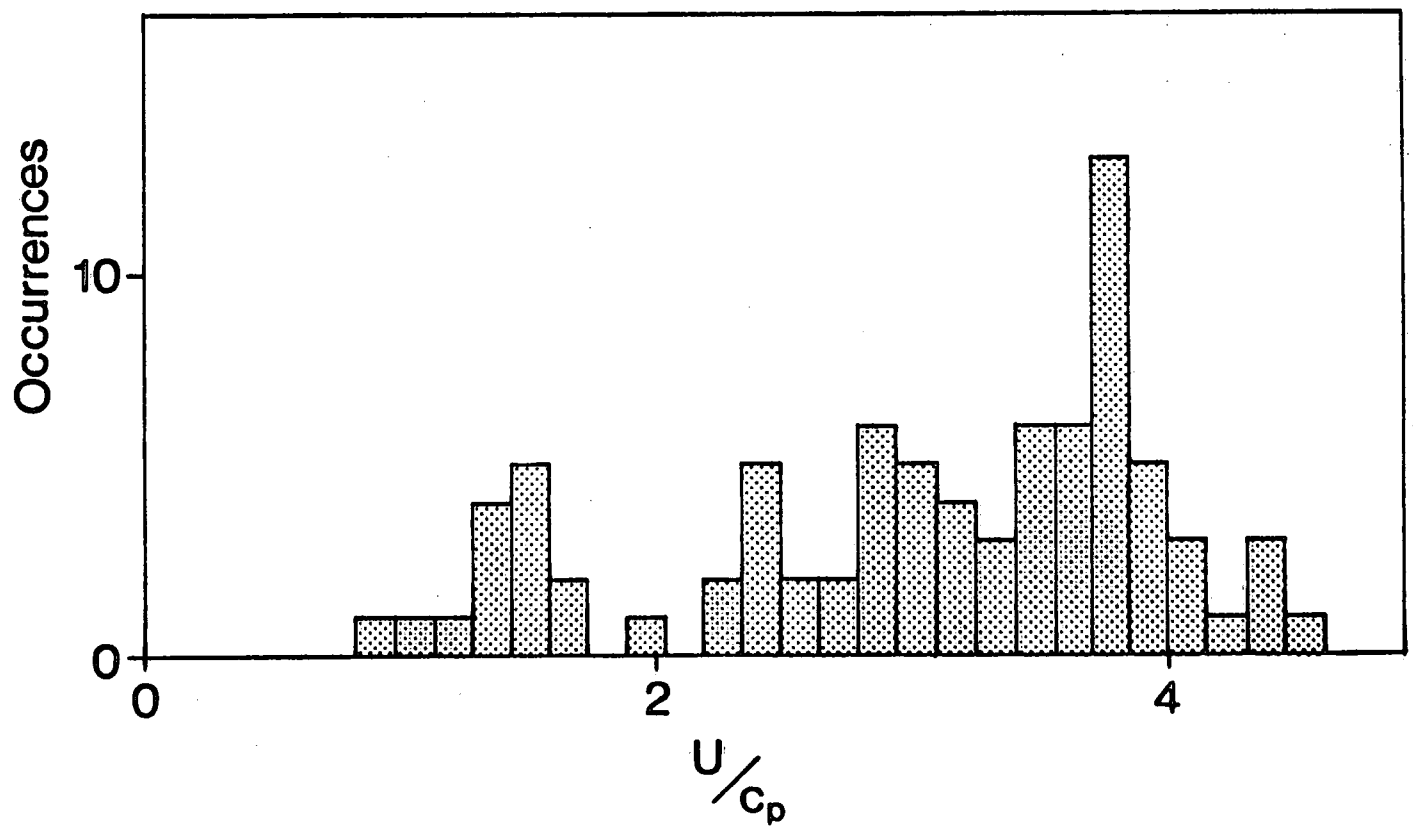

5.1 Histogram of occurrrences of field runs in classes of U/c_p (inverse wave age).

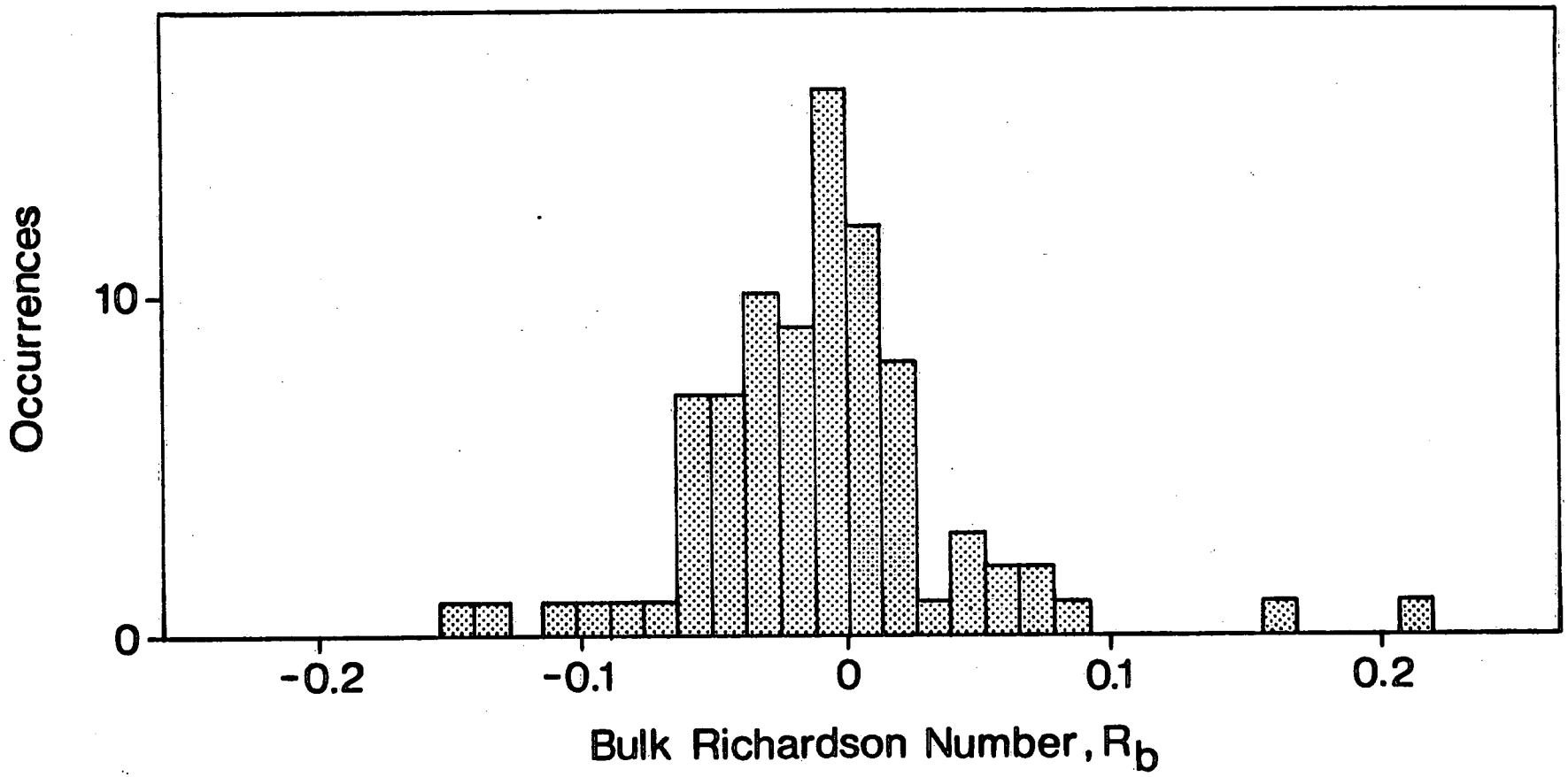

5.2 Histogram of occurrences of field runs in classes of R_b (bulk Richardson number).

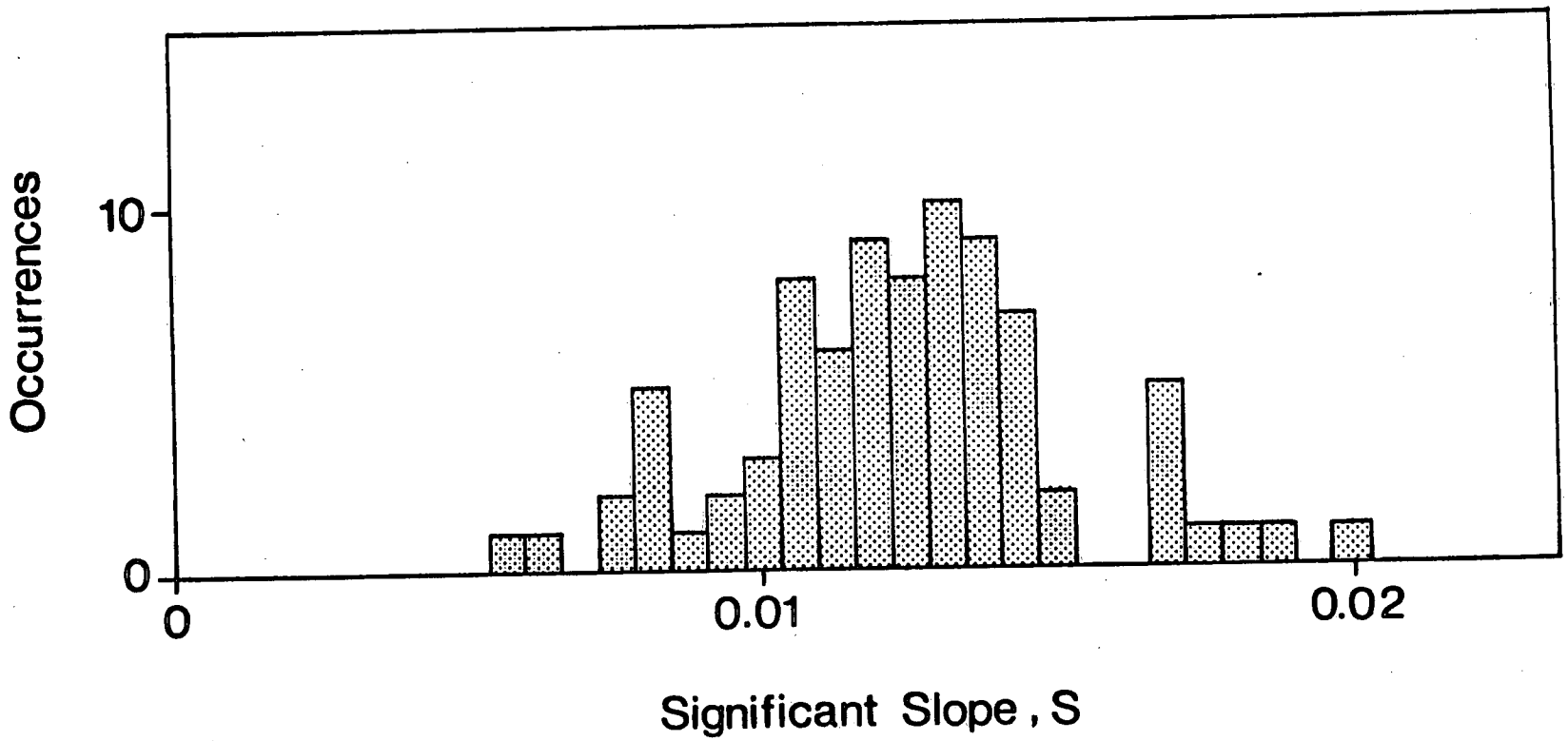

5.3 Histogram of occurrences of field runs in classes of s (significant slope).

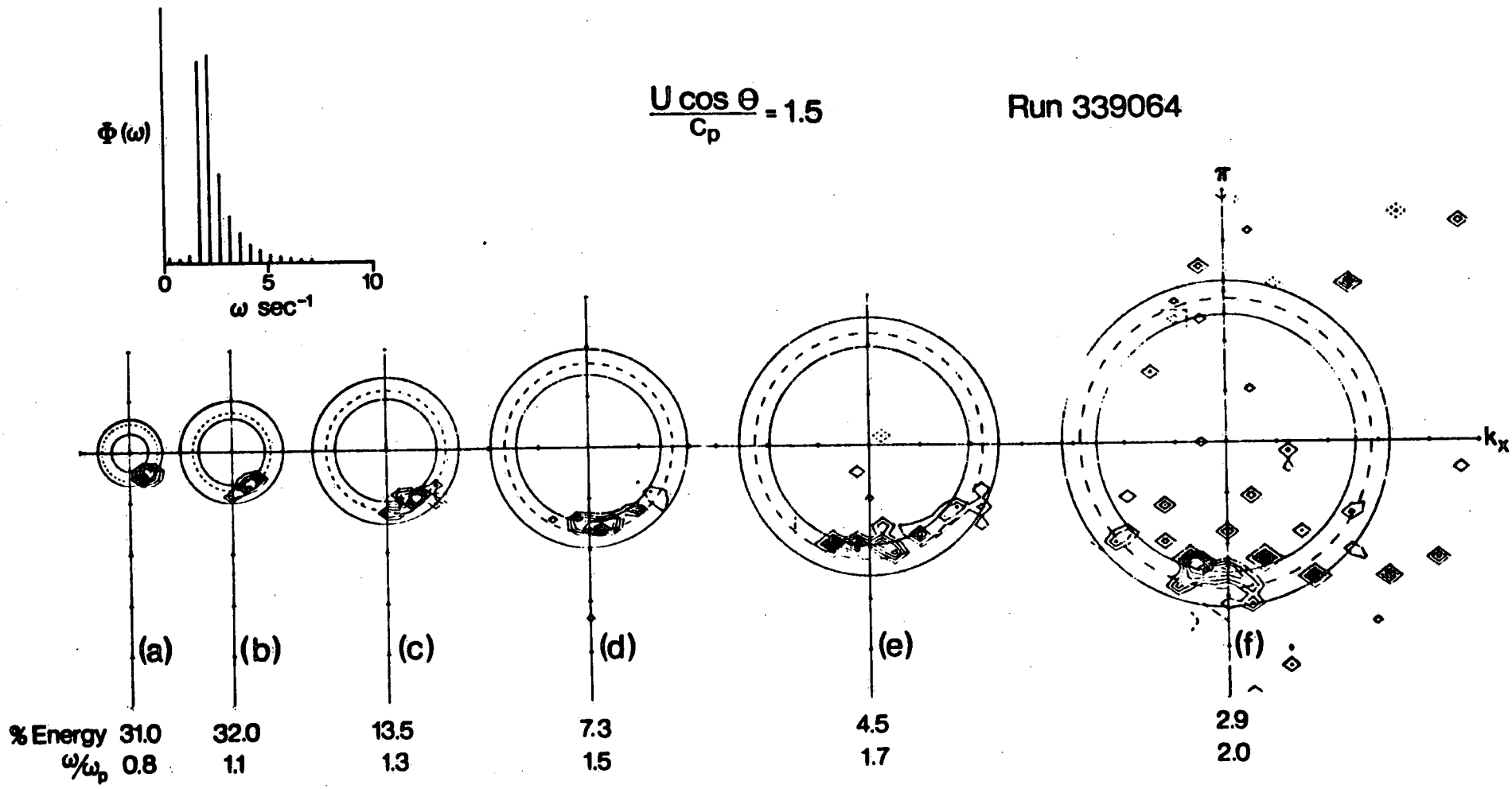

6.1 Wave-number spectra $X(\underset{\sim}{k},\omega)$, (2.21) for a relatively mature spectrum of field waves. The percent energy in each frequency band is indicated. Note that the energy falls within the dispersion circles near the peak, but moves inwards at higher frequencies.

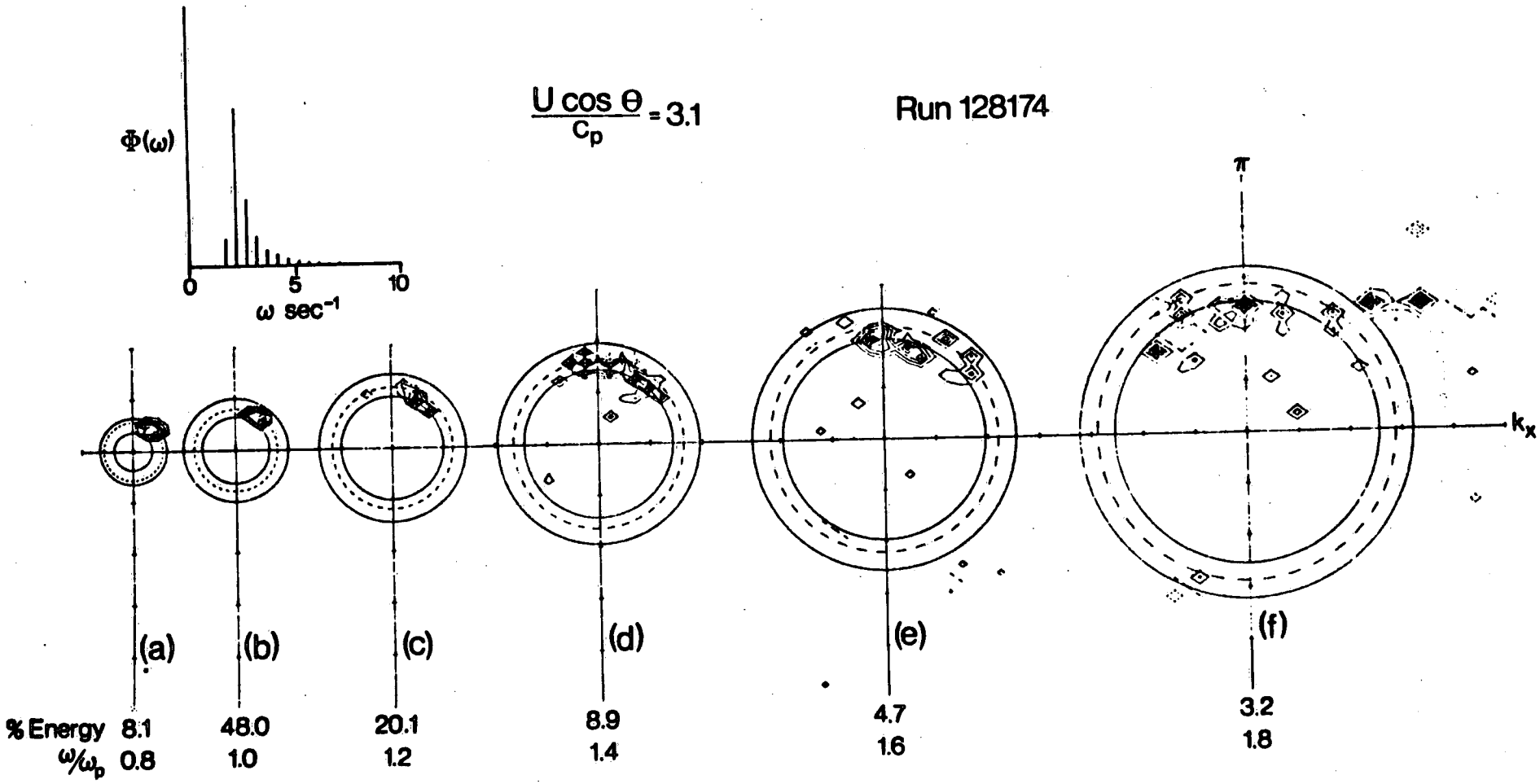

6.2 Wave-number spectra for a relatively young spectrum of field waves. Note that the energy contours are closer to the centre than in figure 6.1

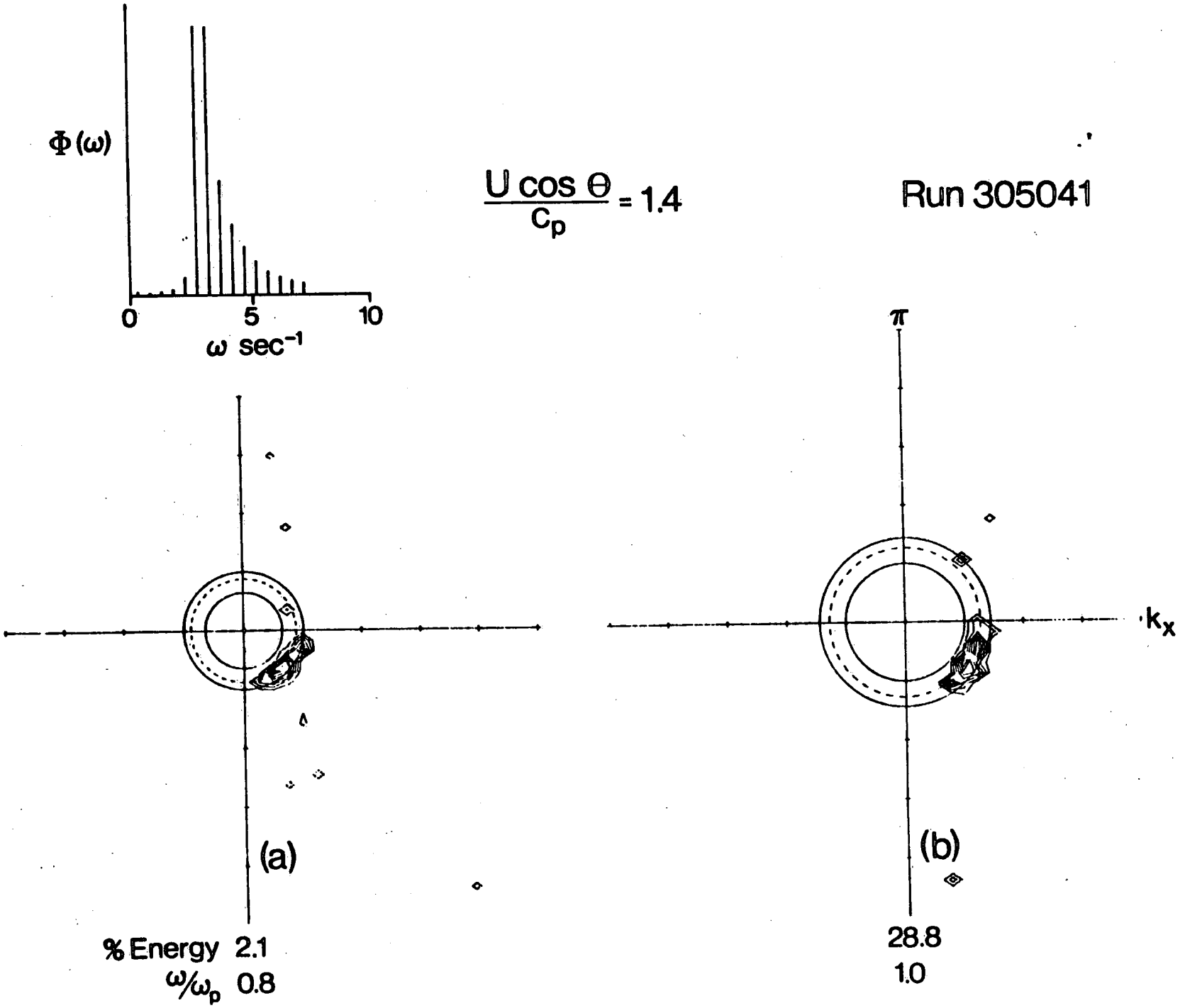

6.3 Wave-number spectra in which the energy density tends to larger wave-numbers than are consistent with the linear dispersion relation. These are evident for wind forced waves.

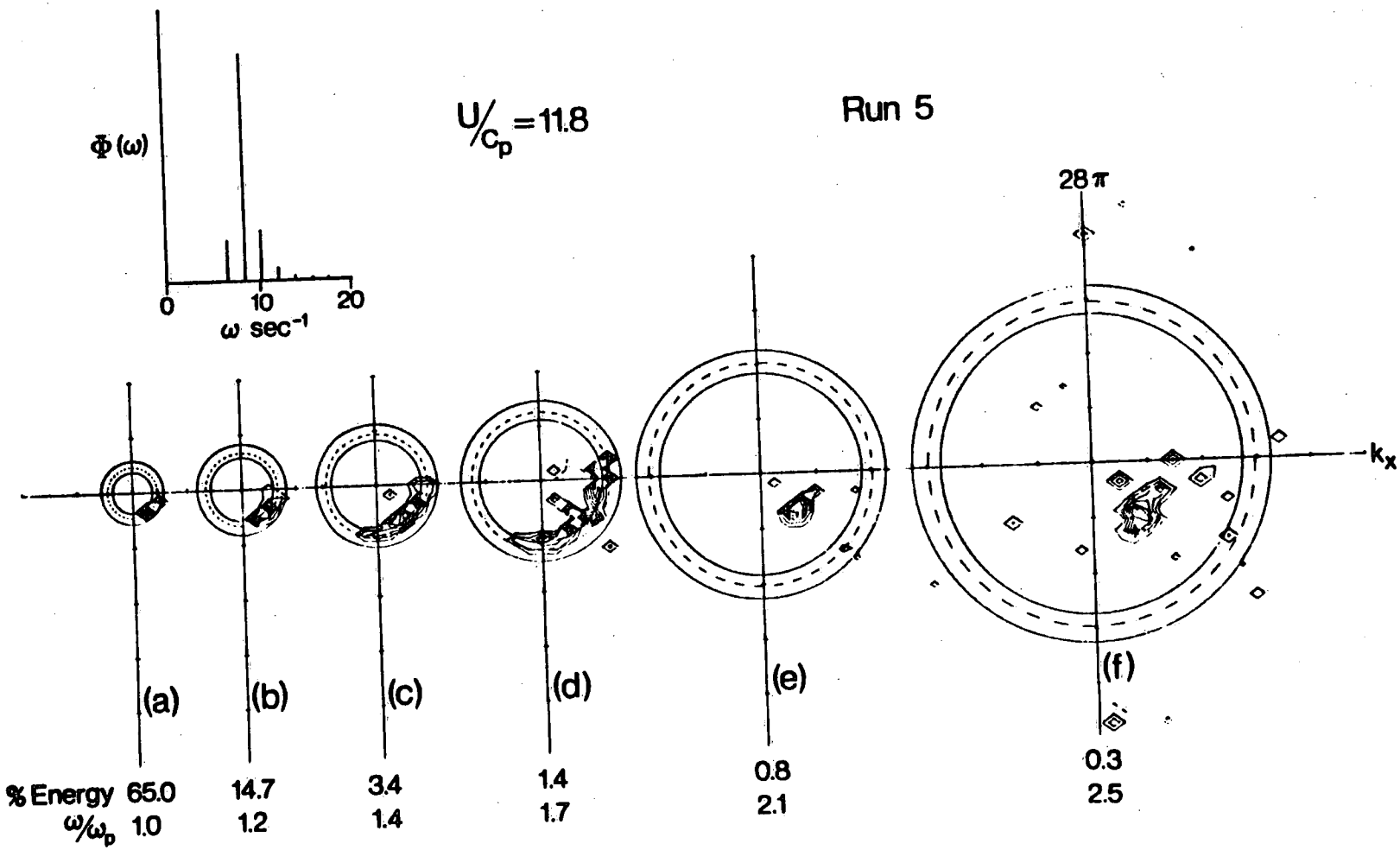

6.4 Wave-number spectra for very young laboratory waves. Evidence for bound harmonics can be seen in (d), (e) and (f).

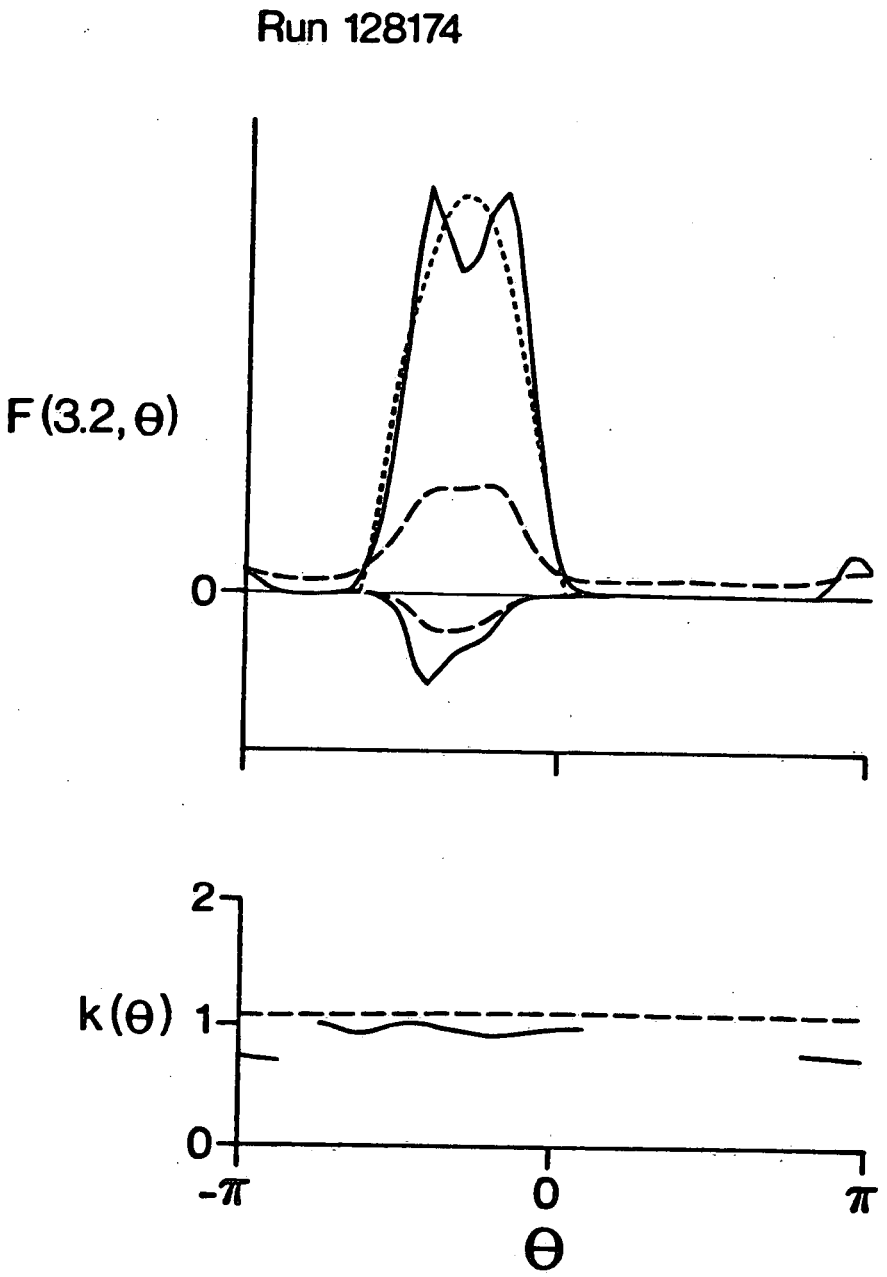

7.1 The top part of the figure is the directional spectrum corresponding to the wave-number spectrum of figure 6.2(d). (———) the detected directional spectrum; (------) the parametric fit described in §7.2; (— — —) the estimated standard deviation of the directional spectrum.

The lower part of the figure is the average wave-number deduced from the wave-number spectrum of figure 6.2 (d). The horizontal dashed line corresponds to the linear dispersion relation (1.1) for the frequency of this band $\omega = 3.2$.

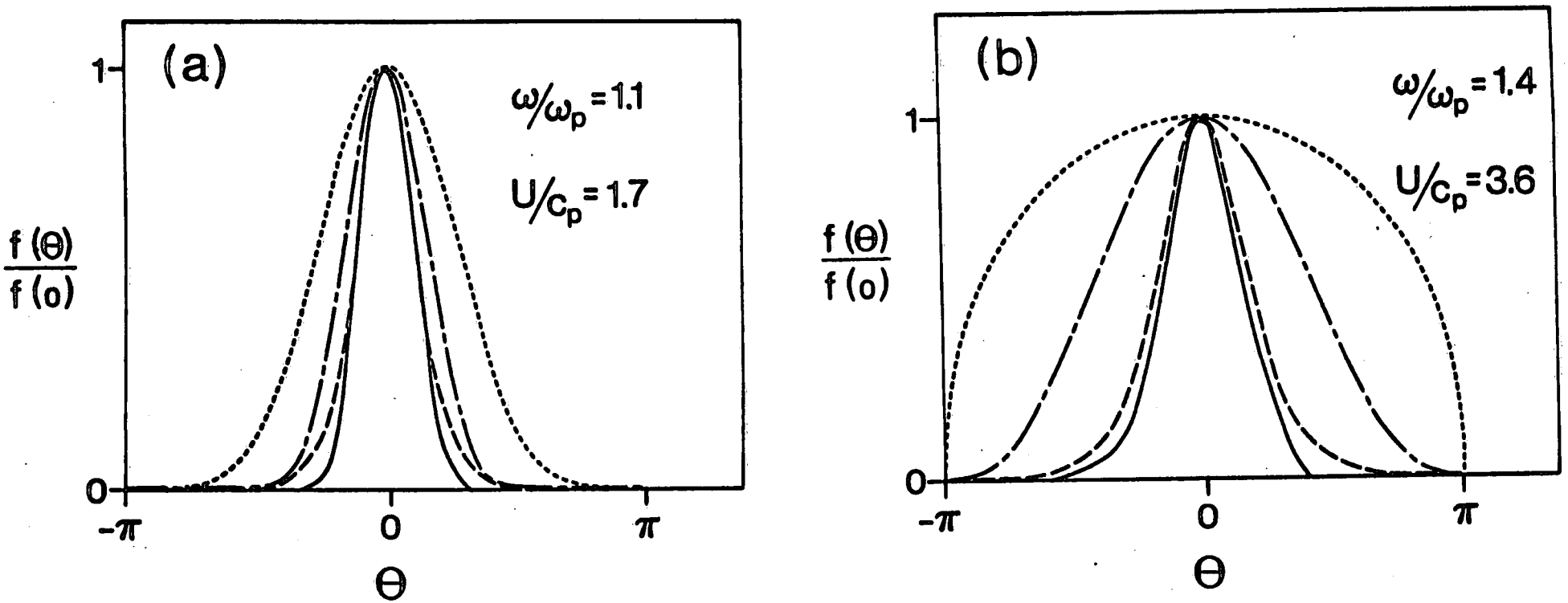

7.2 Typical directional spectra (———) with polar representations due to Mitsuyasu et al., 1975 (-----); Hasselmann et al., 1980 (— - — -); this paper, $\text{sech}^2(\beta\theta)$ §11 (— — —).

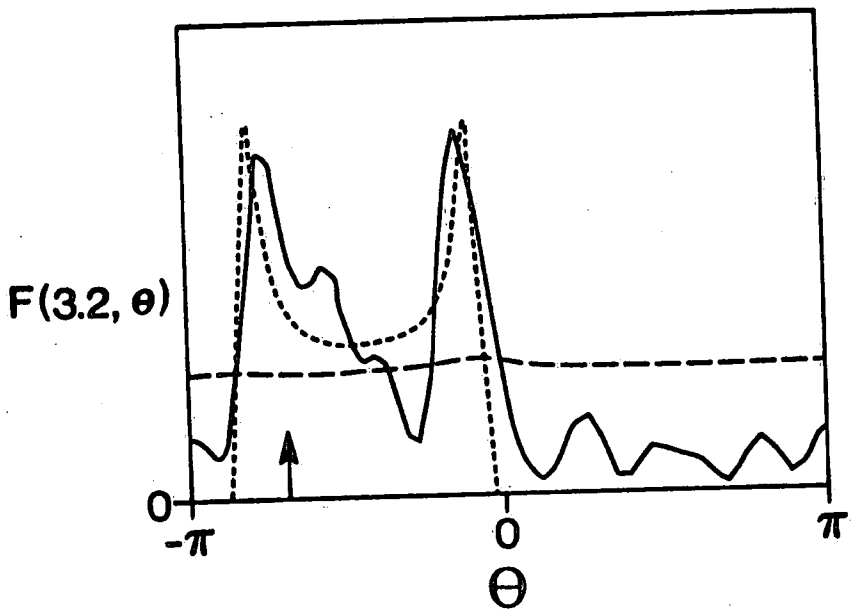

7.3 A directional spectrum and parametric fit showing distinct double peaks. The run number is 303172, the wind speed was 7.7 m/s and the wind direction is indicated by an arrow.

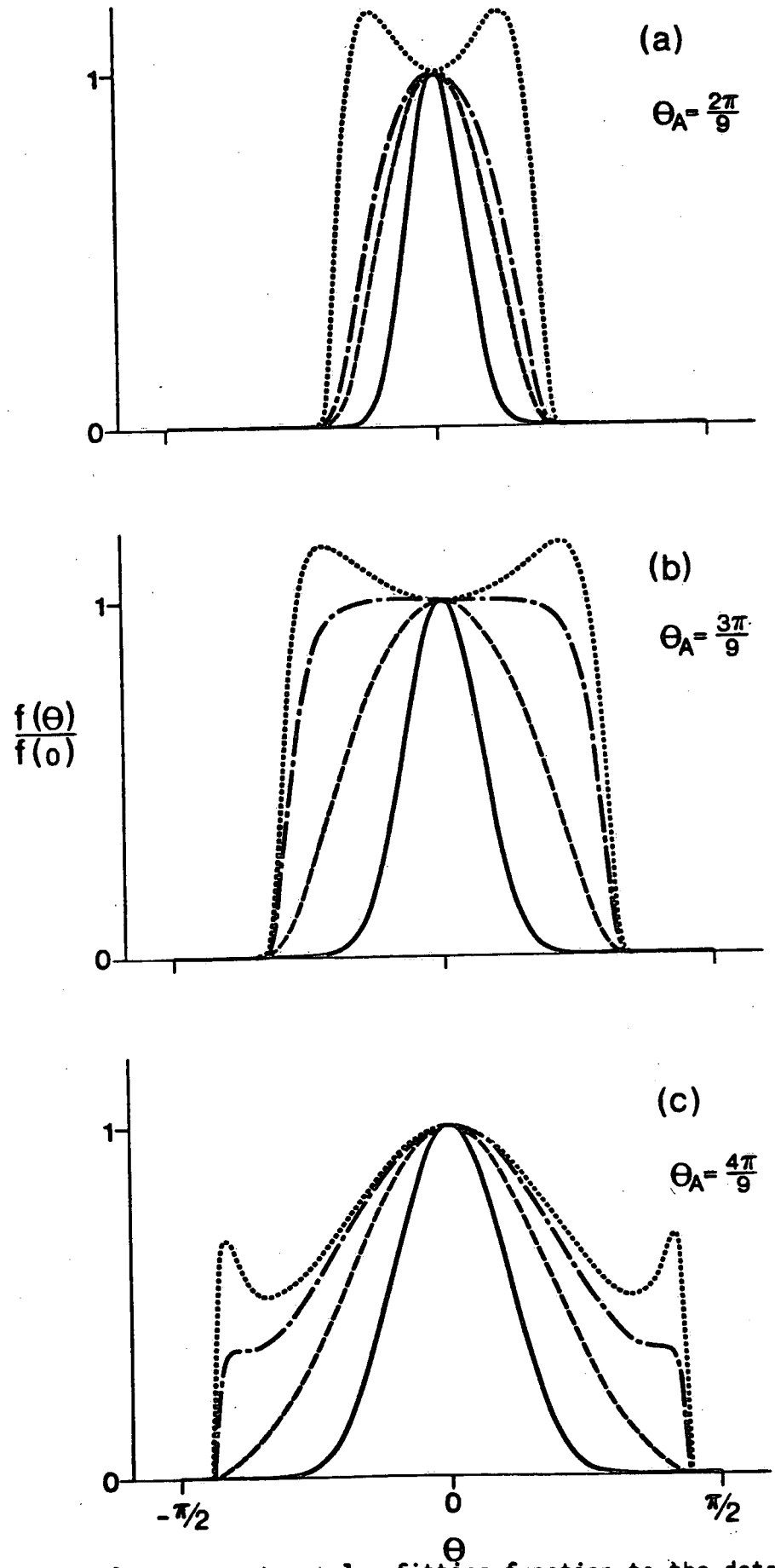

7.4 Examples of the four parameter polar fitting function to the detected directional spectra. The four parameters correspond to mean direction $\bar{\theta}$, height in that direction A_0, spread θ_A and peakedness L. Multiple peaks occur for L > 3.2. The values of L correspond to (———) L = -5; (— — —) L = 2; (— - —) L = 3.2; (-----) L = 5.5, 3.5, 3.5 in (a), (b) and (c) respectively.

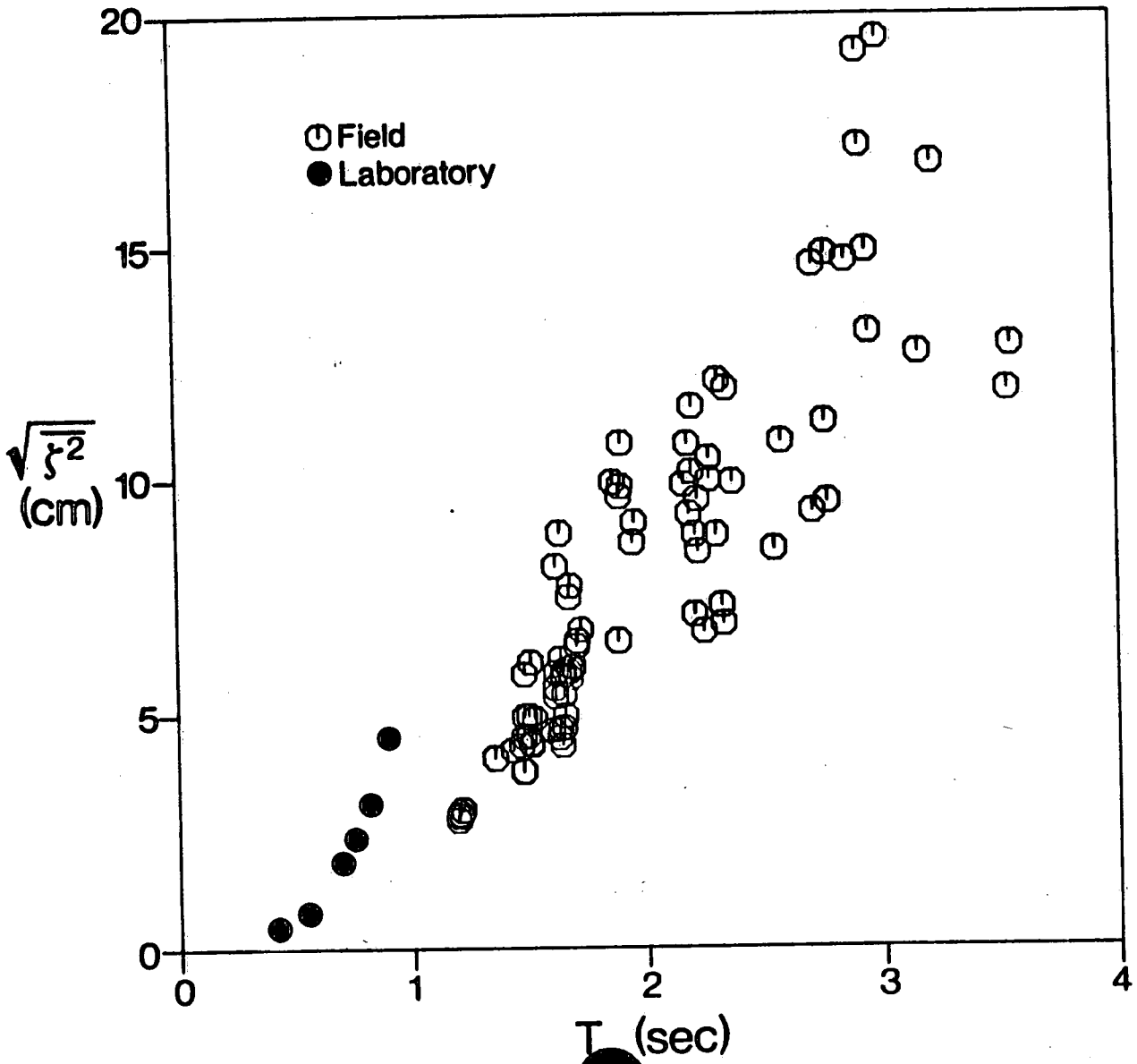

8.1 Root-mean-square surface elev[illegible]n versus peak period.

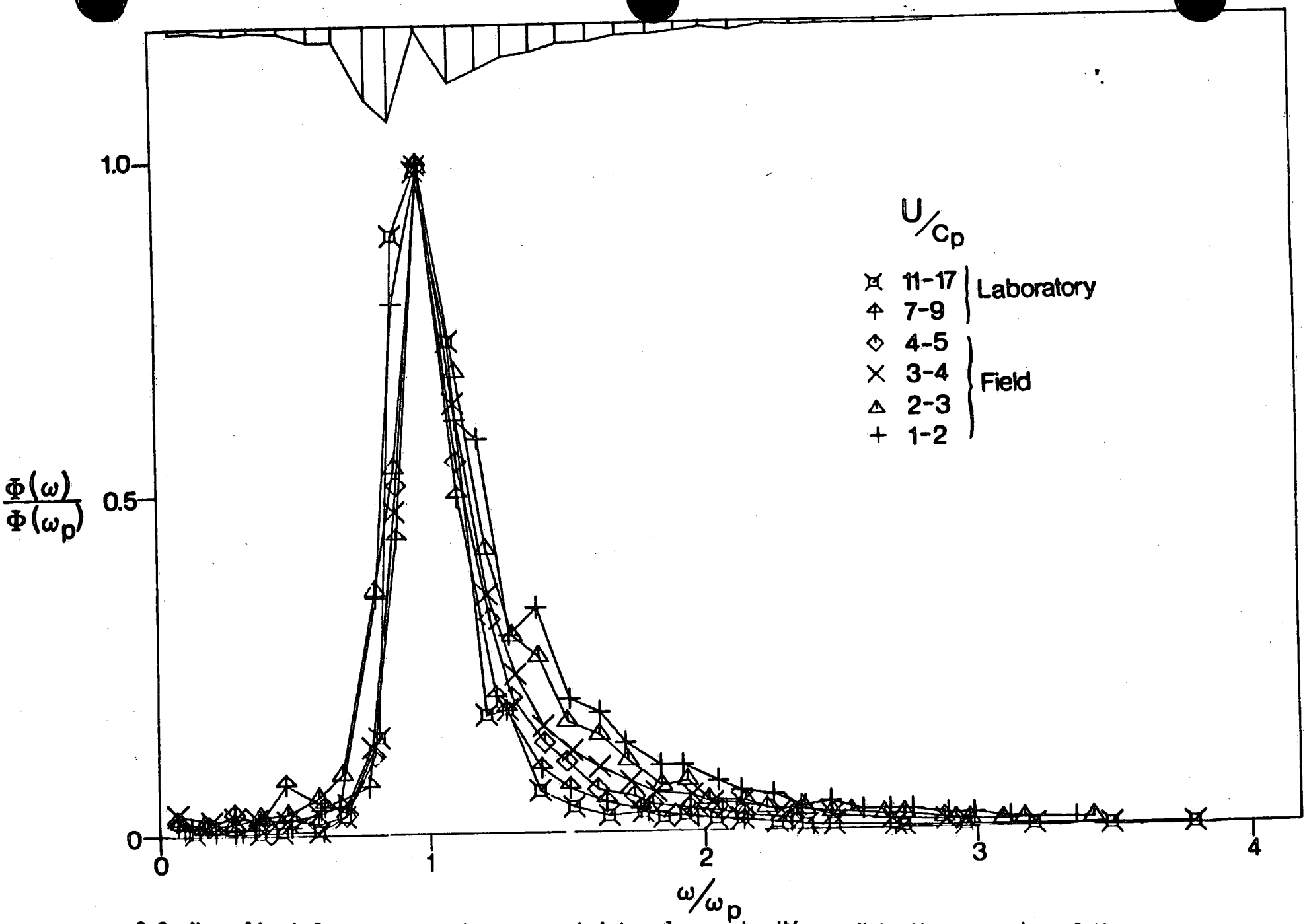

8.2 Normalized frequency spectra grouped into classes by U/c_p. Note the narrowing of the spectra with increasing U/c_p. The vertical bars at the top of the figure are an estimate of the 90% confidence limits based on the standard error of the mean.

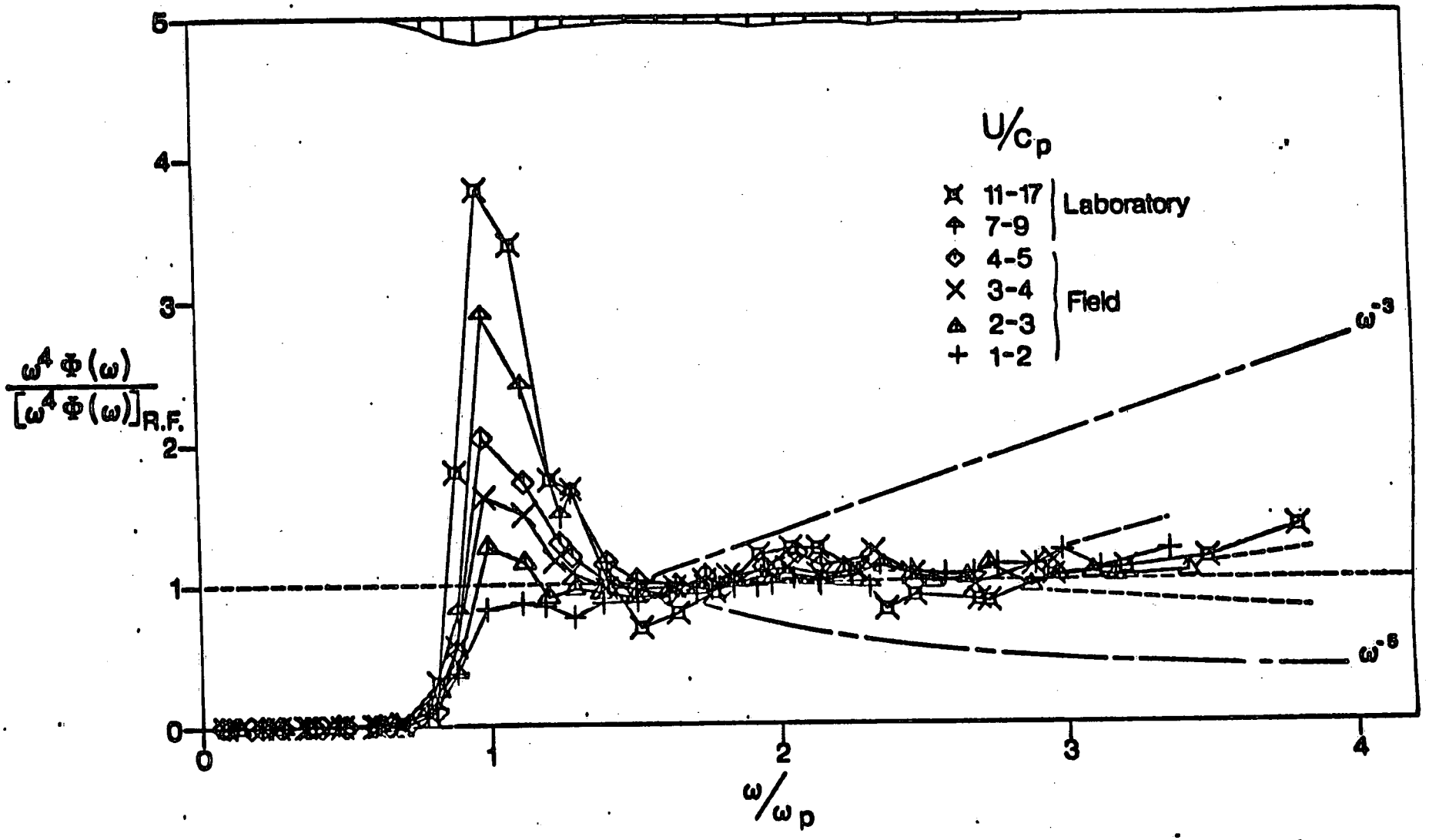

8.3 Frequency spectra x ω^4 normalized by the rear face $[\omega^4\Phi(\omega)]_{R.F.}$ which is the average of $\omega^4\Phi(\omega)$ in the region $1.5\ \omega_p < \omega < 3\omega_p$. The lines corresponding to ω^{-5} and ω^{-3} are also shown (—— – ——). The effect of a 10 cm/s ambient current with or against the waves is also shown (-----) as is the effect of wind drift in a 10 m/s wind (—— ——). The spectra are grouped in classes of U_c/c_p.

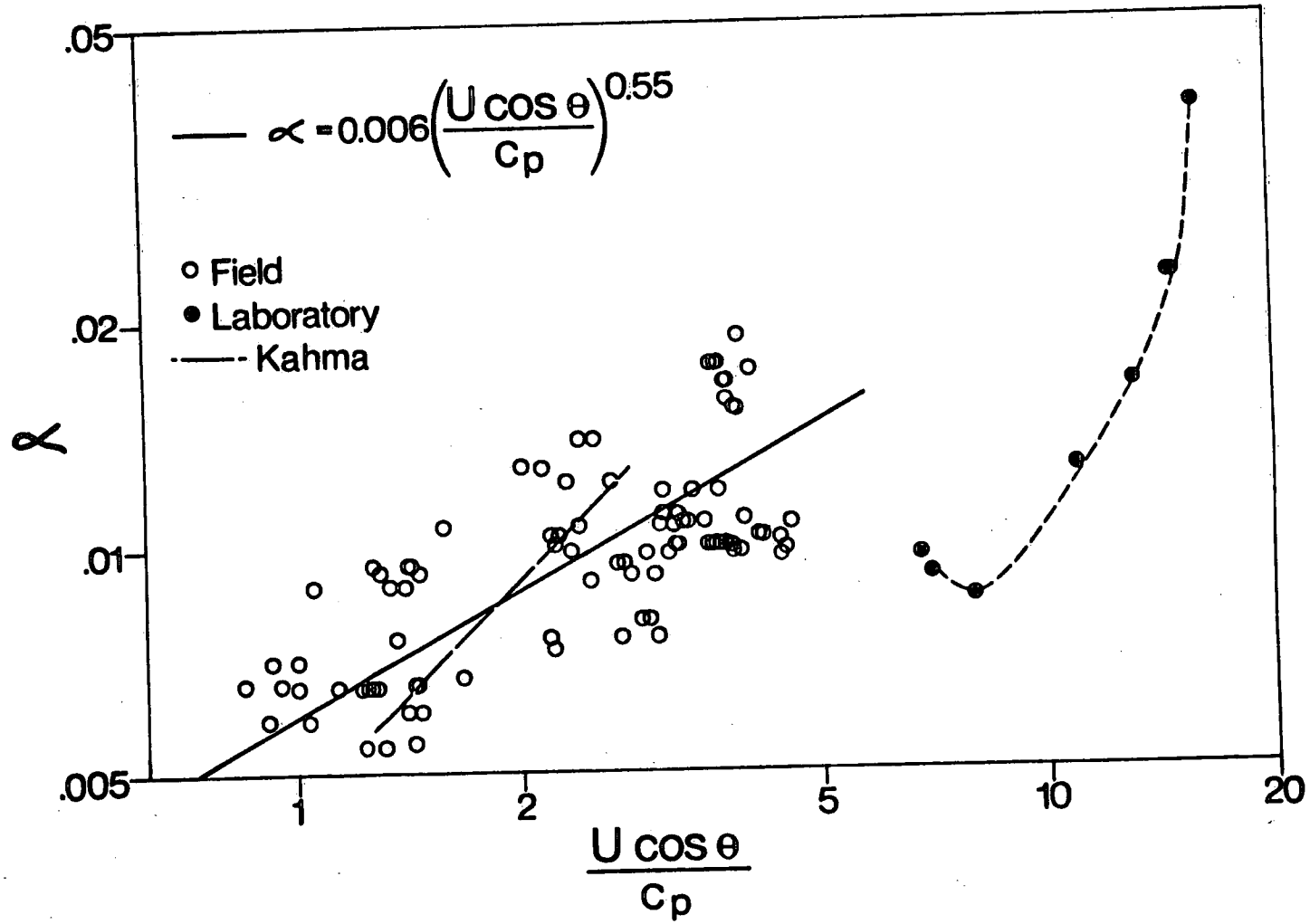

8.4 The equilibrium range spectral parameter α versus U_c/c_p. The solid line is (8.2) and the broken line is from the relation given by Kahma (1981).

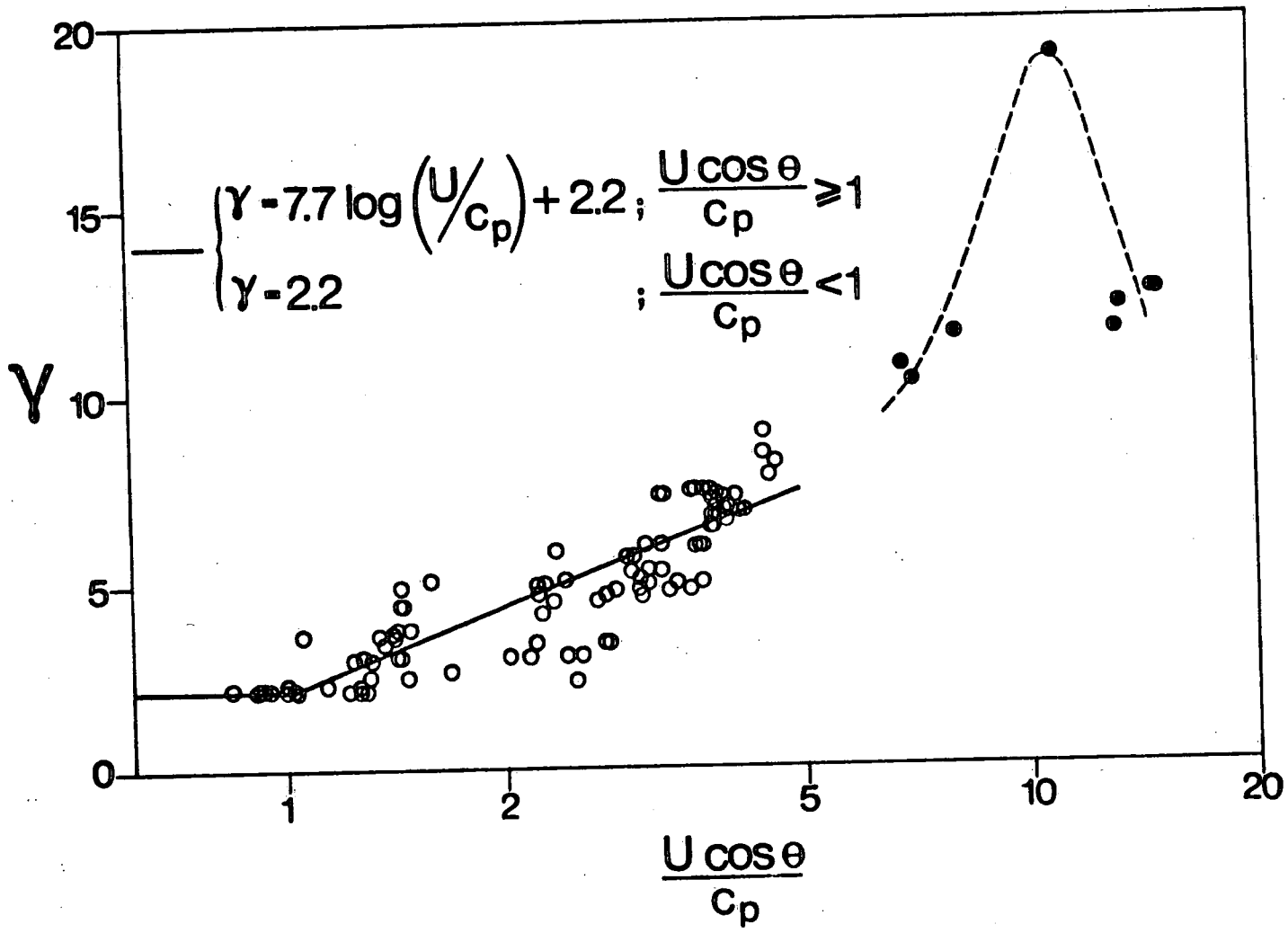

8.5 The peak enhancement parameter γ versus U_c/c_p.

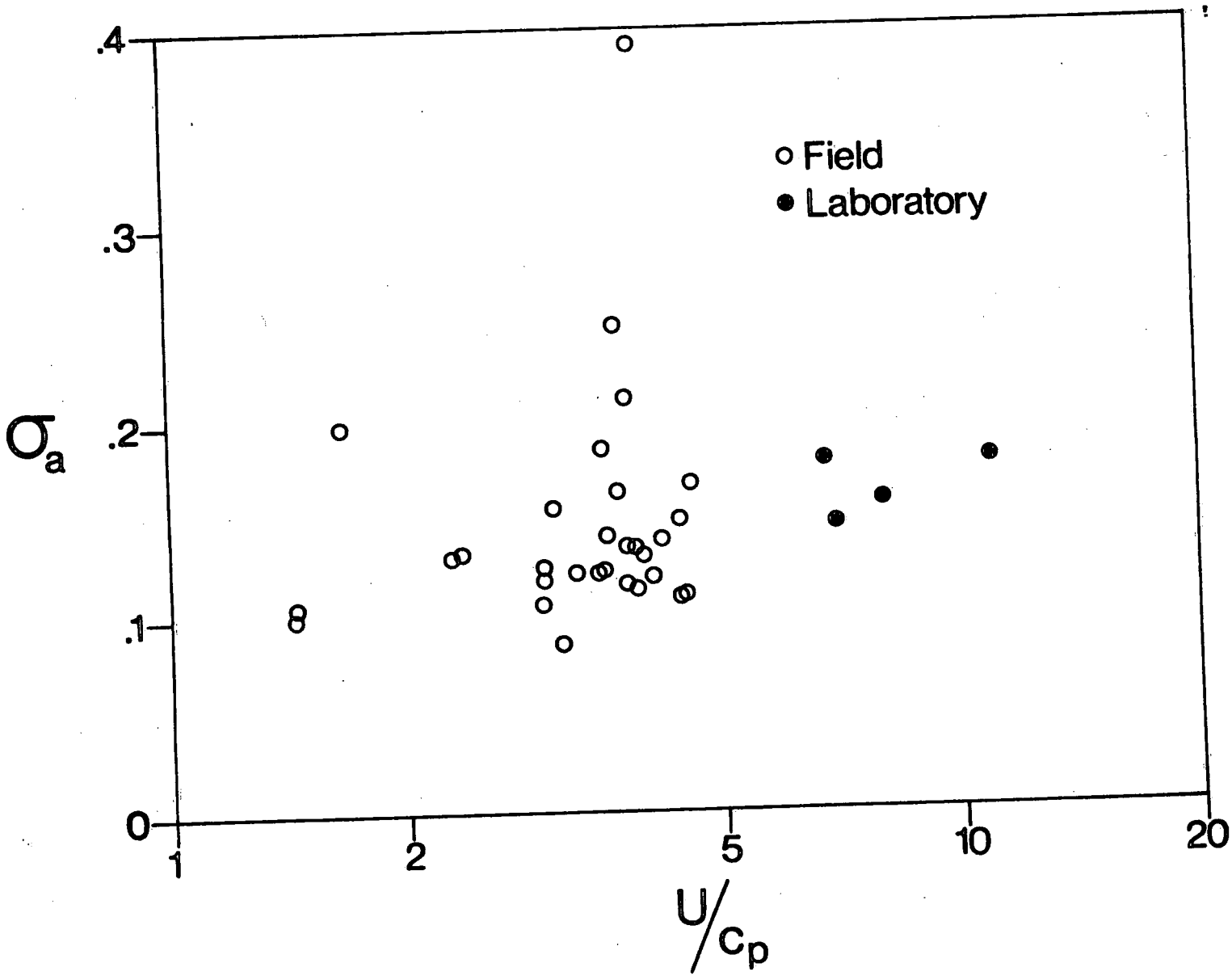

8.6 The peak width parameter σ_a versus U_c/c_p.

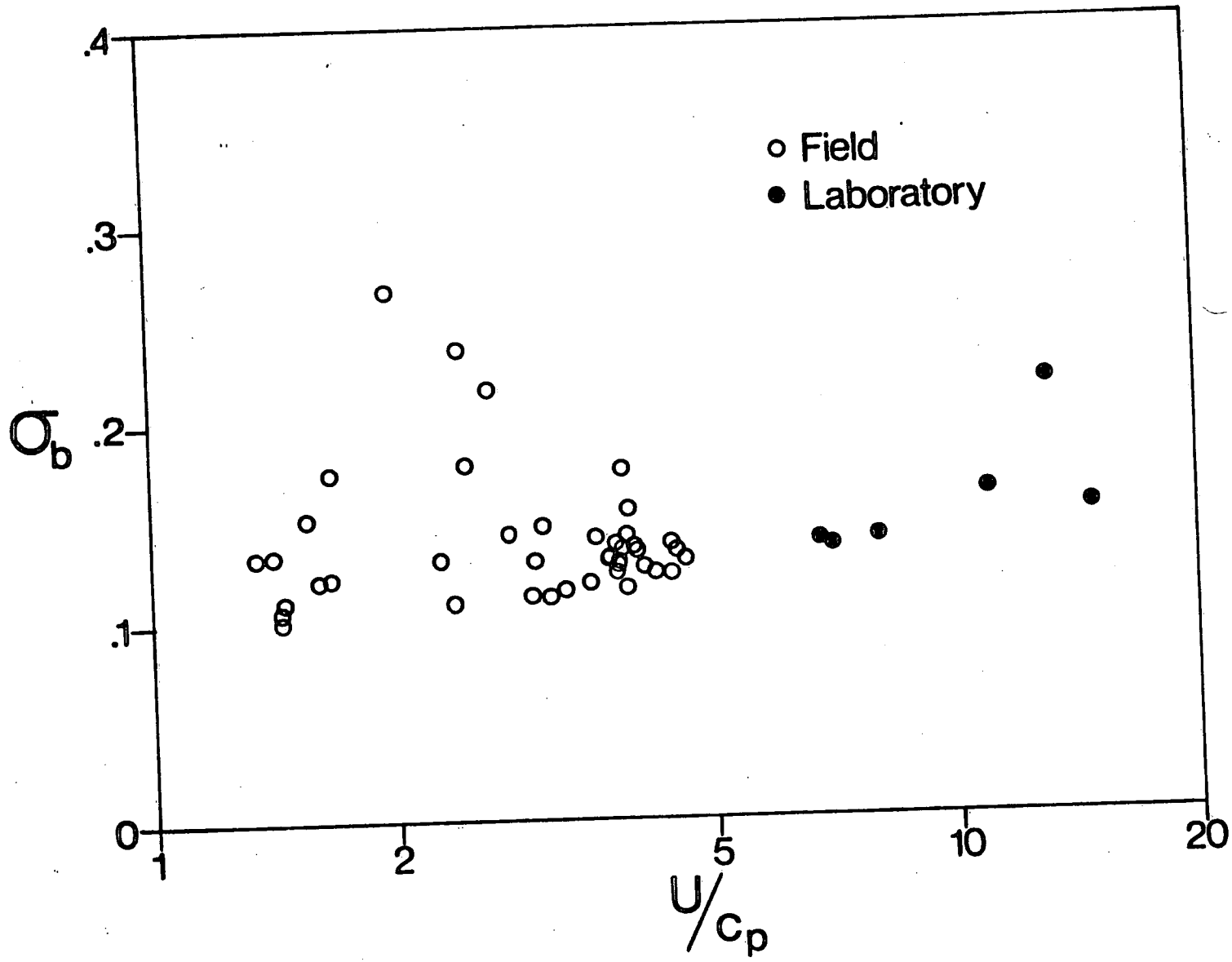

8.7 The peak width parameter σ_b versus U_c/c_p.

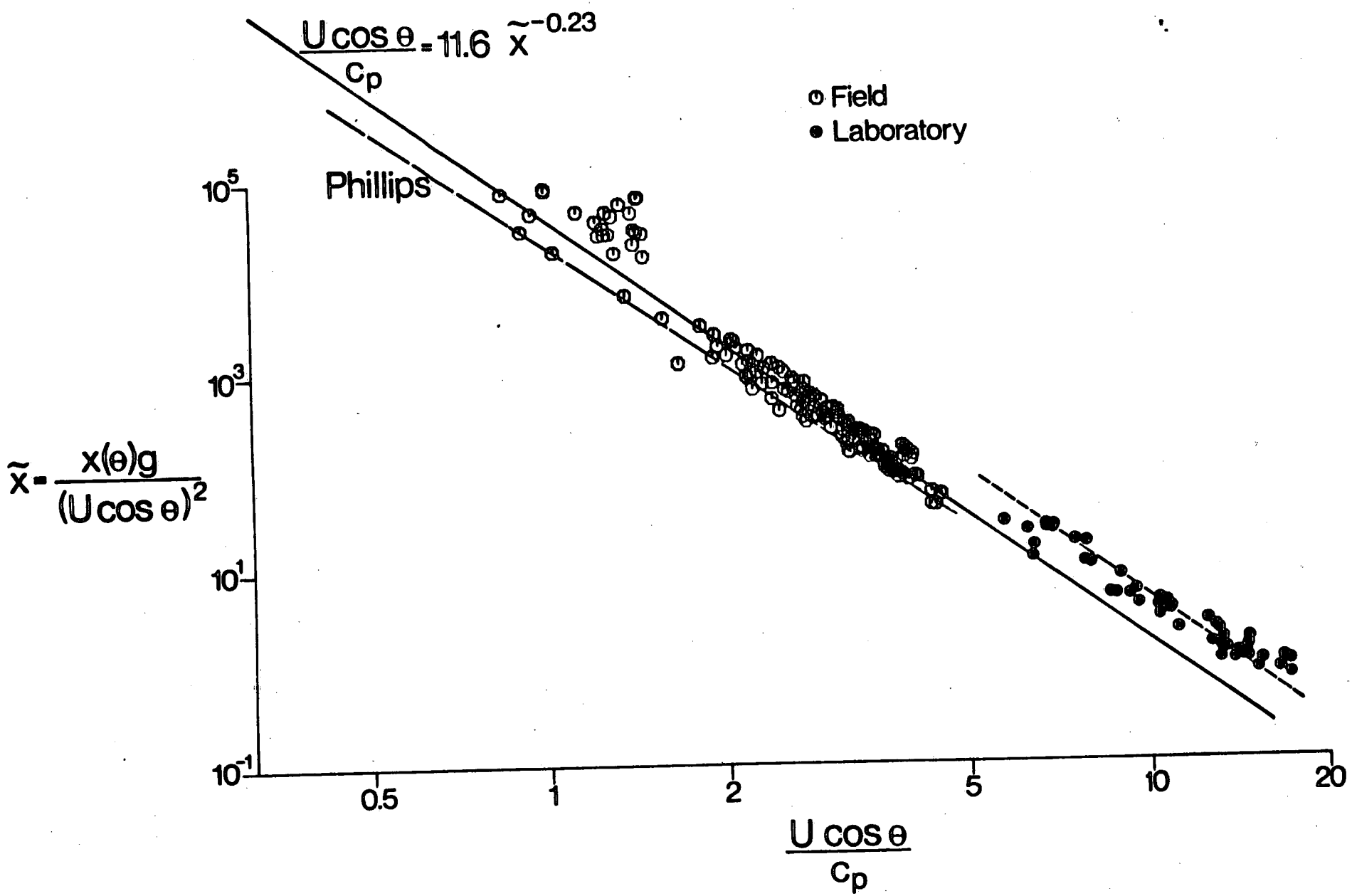

8.8 Non-dimensional fetch versus U_c/c_p. (———) fit to the field data; (-----) fit to the laboratory data; (— — — —) from Phillips (1977).

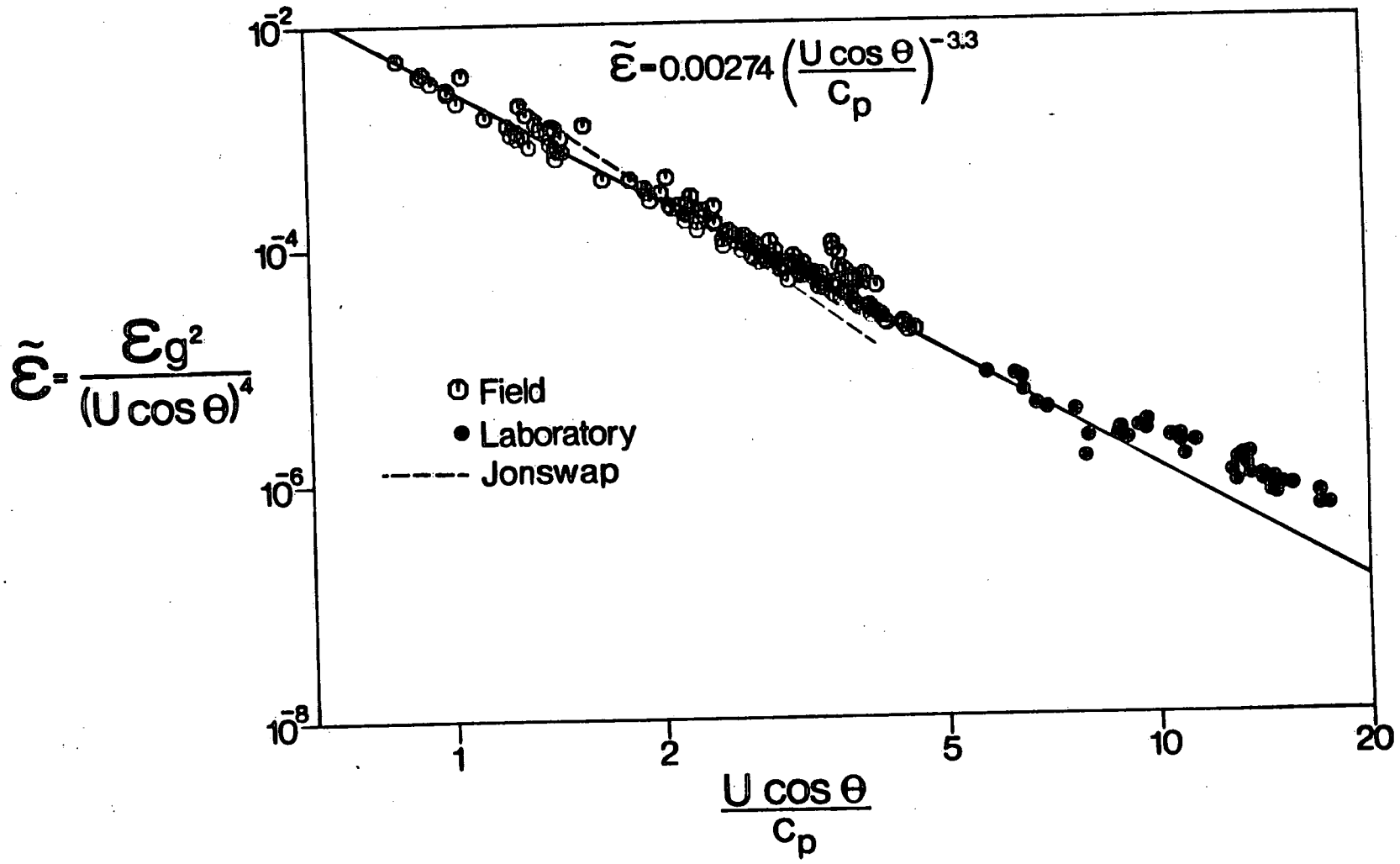

8.9 Non-dimensional variance of surface elevation versus U_c/c_p. (——) fit to the field data; (-----) JONSWAP, the length of the line indicates the range of data gathered during the JONSWAP experiment.

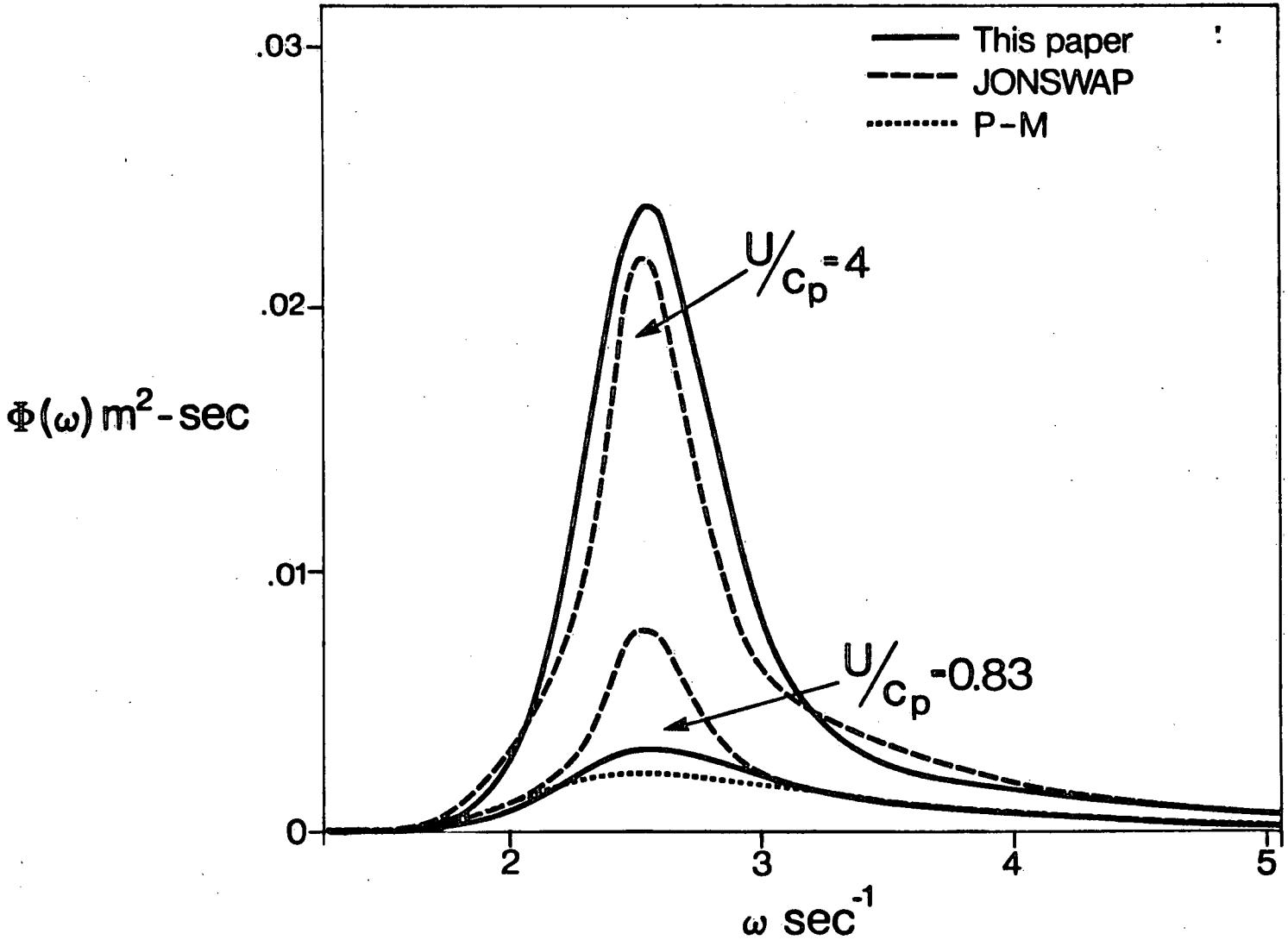

8.10 Comparison of spectra with $\omega_p = 2.5$ for two values of U/c_p or, equivalently, of non-dimensional fetch.

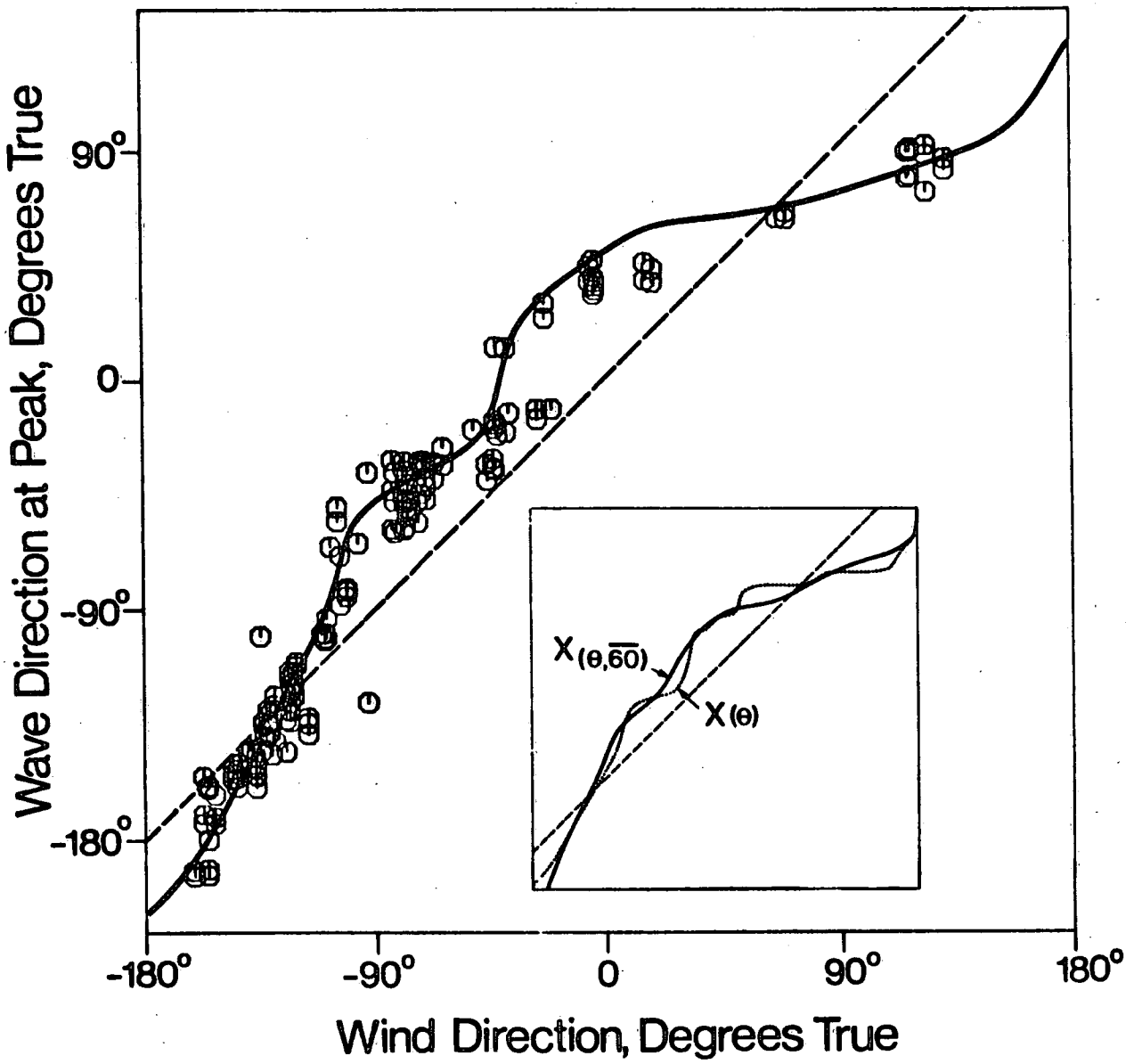

9.1 Mean direction of waves at the spectral peak versus mean wind direction (approach bearing in both cases). The broken line is the line of perfect agreement; the solid line has been deduced from similarity considerations (9.1), using fetch averaged over 30° (±15°) about the wave approach direction. The inset demonstrates the relative insensitivity to choice of averaging over 60° (solid) or not at all (broken).

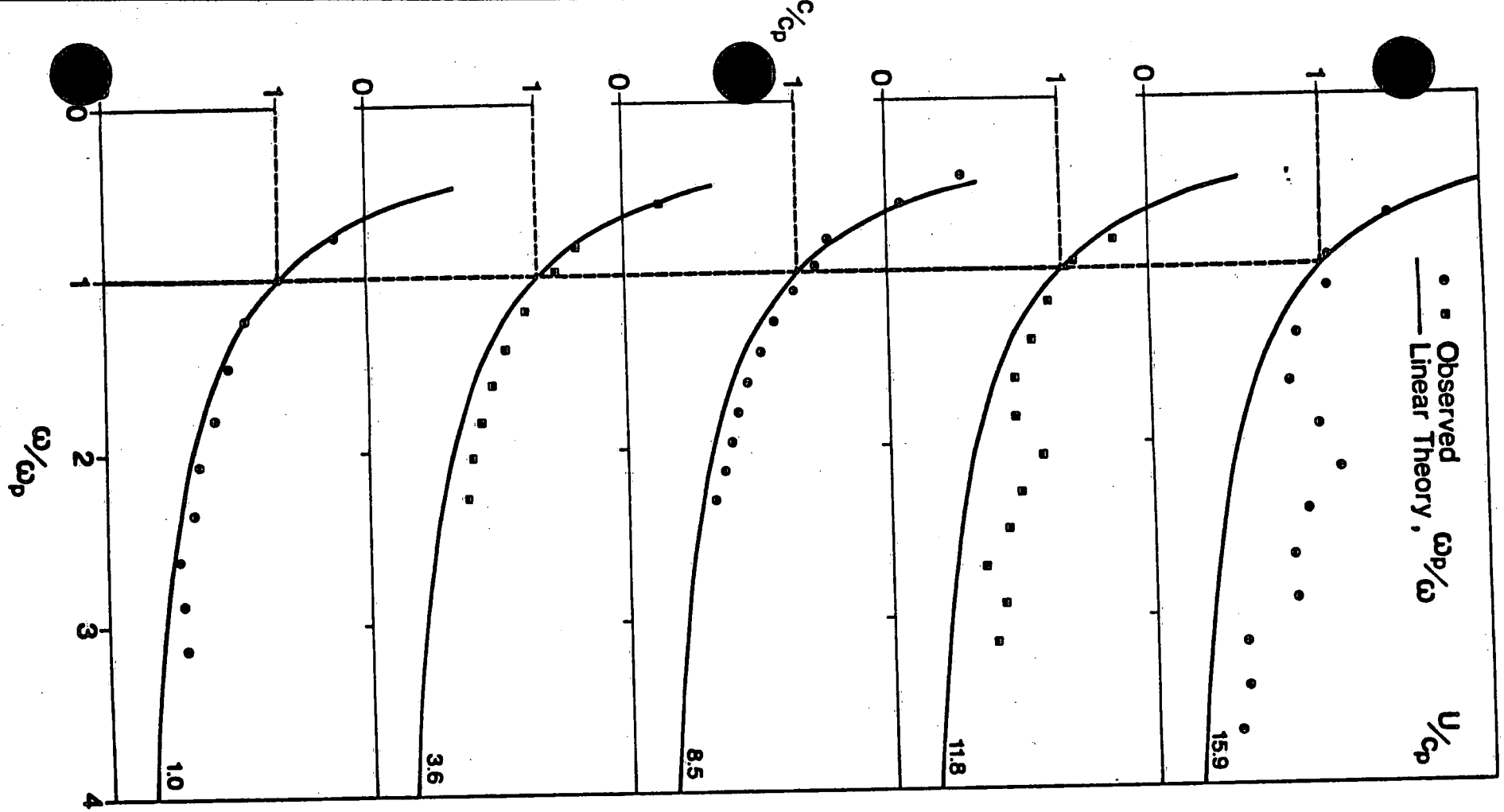

10.1 Normalized average phase speed versus ω/ω_p for five spectra. The two at the bottom of the figure are from field data, the others from laboratory data. As U/c_p increases the effects of bound harmonics are apparent. The normalizer c_p is the theoretical linear phase speed of the peak waves $c_p = g/\omega_p$.

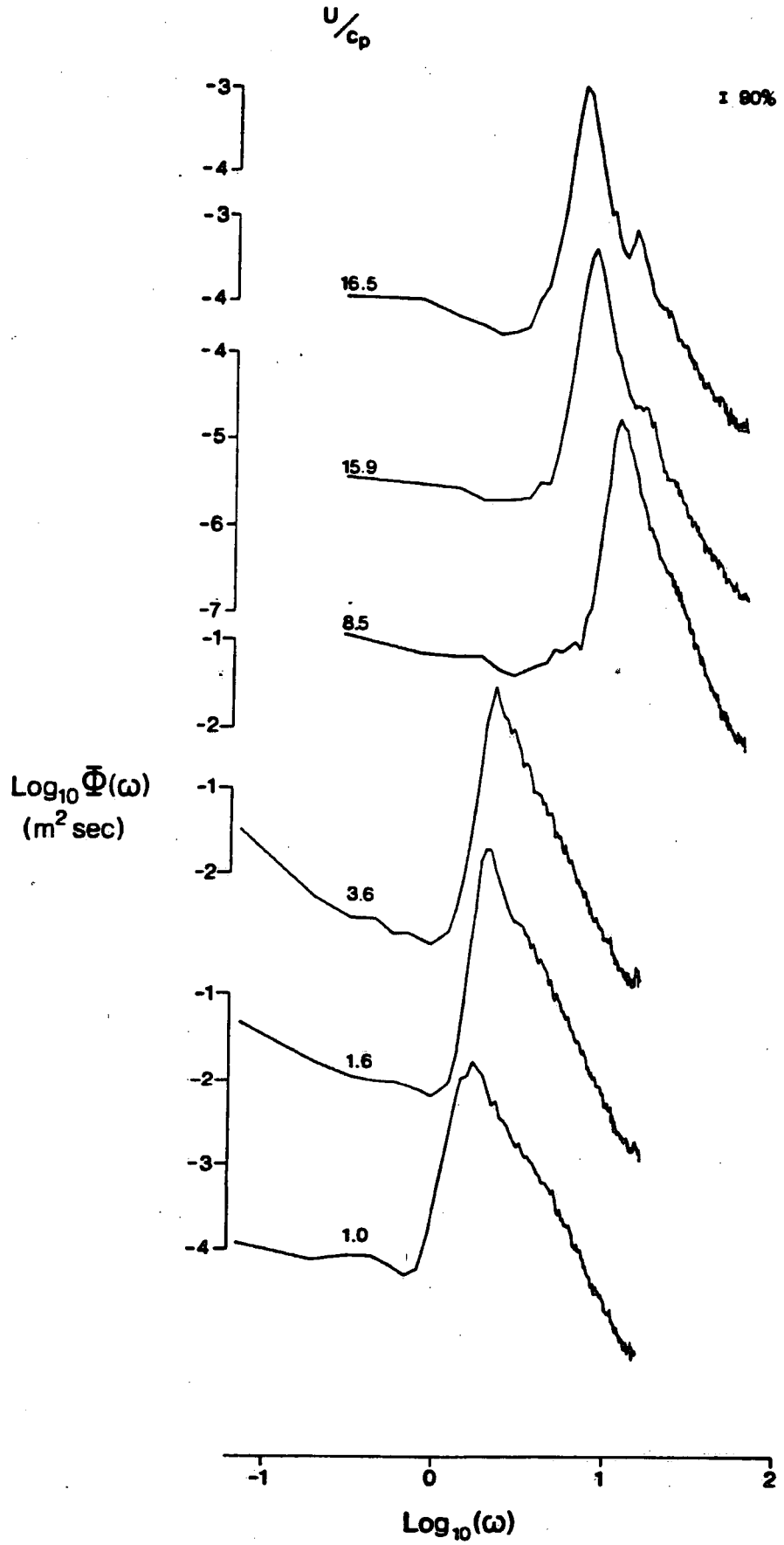

10.2 Log-log spectra for three runs of field waves (bottom) and three runs of laboratory waves. With increasing U/c_p the spectra become narrower and acquire secondary peaks at $n\,\omega_p$. The 90% confidence limits are indicated by a vertical bar.

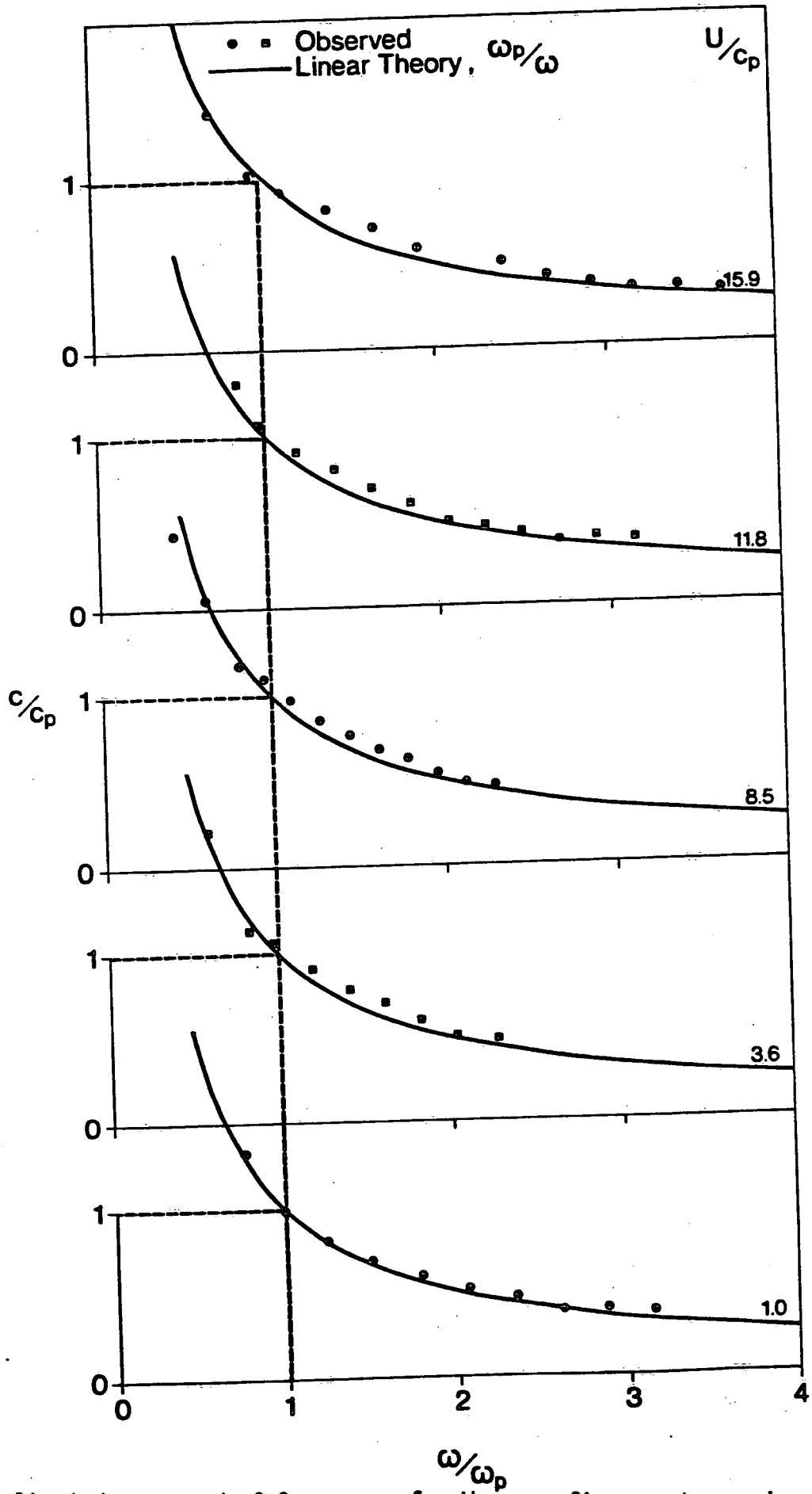

10.3 Normalized phase speed of free waves for the same five spectra as in figure 10.1. The effects of amplitude dispersion with increasing U/c_p are apparent.

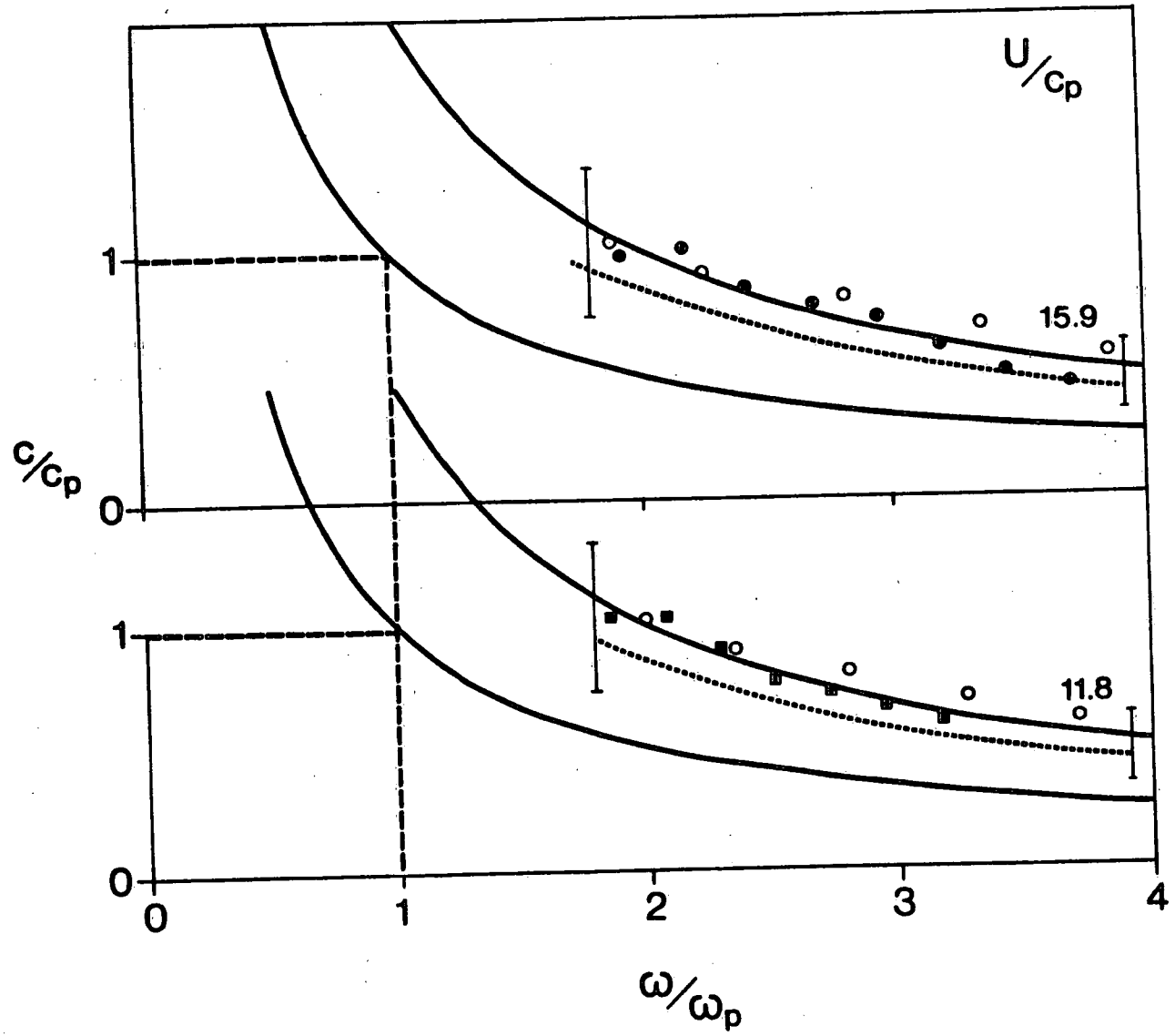

10.4 Normalized phase speed of the bound second harmonic for the two highest U/c_p cases. The solid circles are the measured values; the open circles are taken from figure 10.3 transposed to twice the frequency and represent the expected speed of second harmonics bound to the observed peak waves.

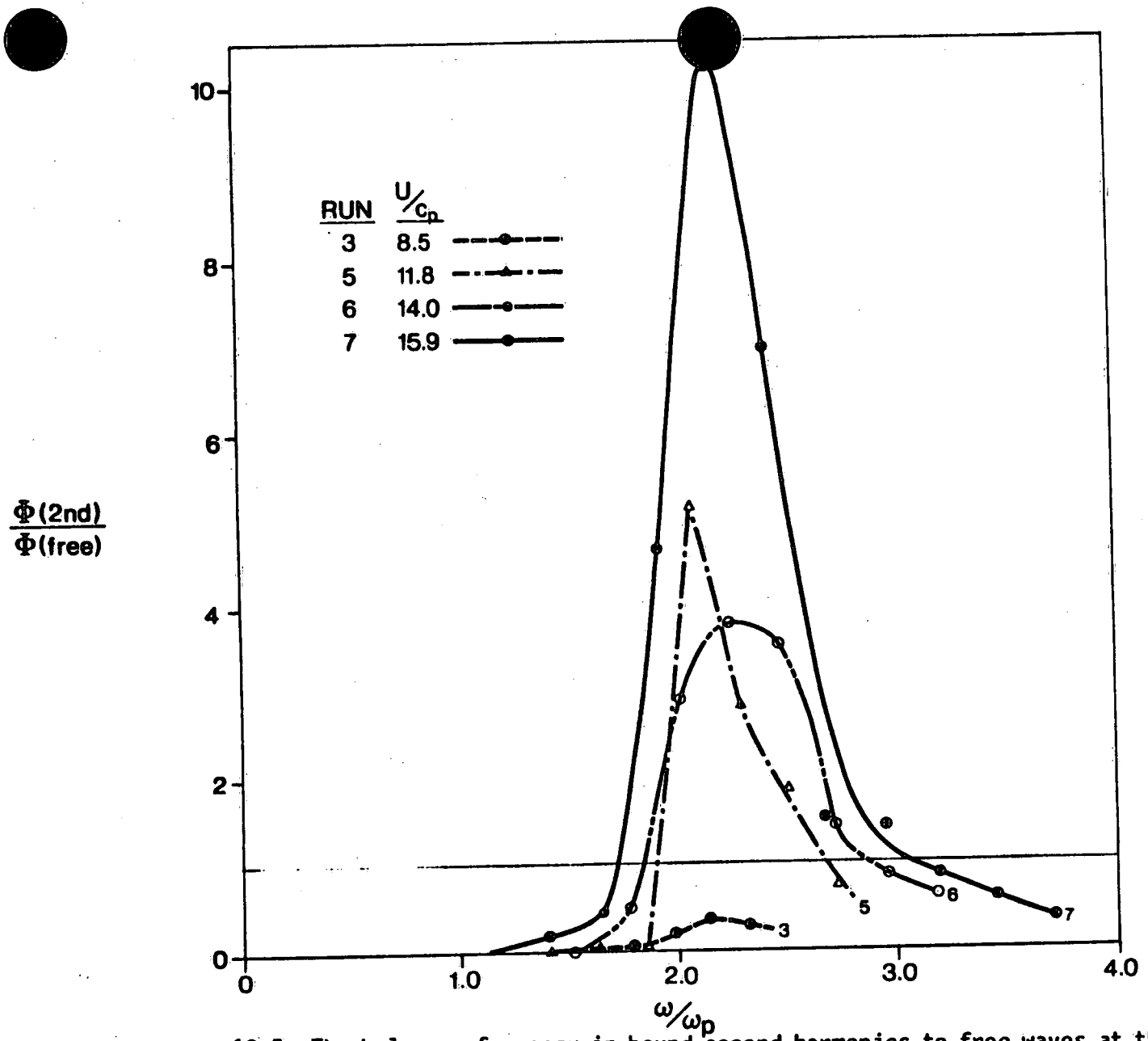

10.5 The balance of energy in bound second harmonics to free waves at the same frequency. In the range $8.5 < U/c_p < 11.8$ the energy in the second harmonics of the peak exceeds the energy in the free waves at $\omega = 2\,\omega_p$.

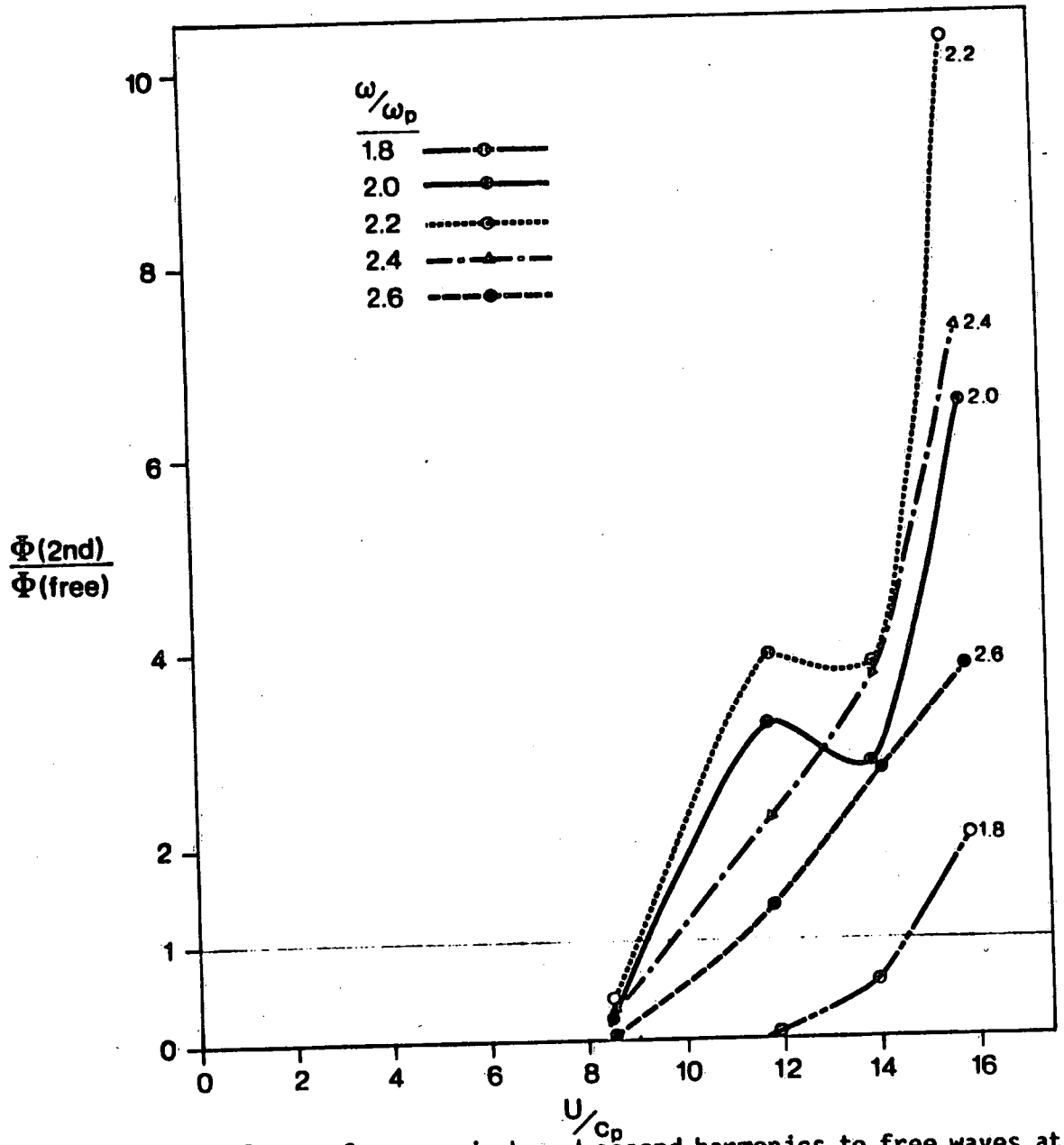

10.6 The balance of energy in bound second harmonics to free waves at the same frequency versus U/c_p. The energy in the second harmonic of the peak waves exceeds the energy in the free waves for $U/c_p > 9$.

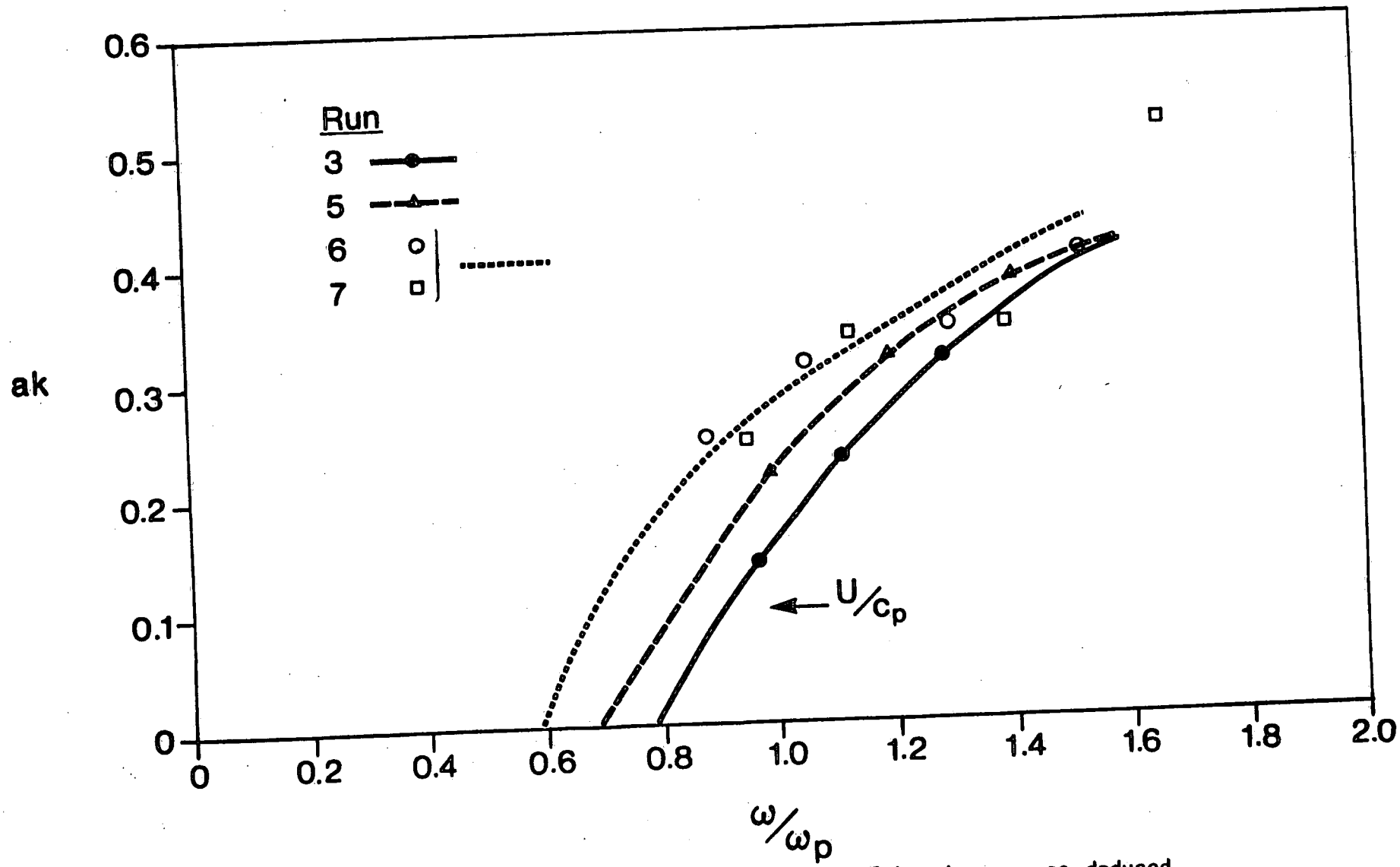

10.7 The steepness of spectral components of laboratory waves deduced from the balance of energy in second harmonics to that in the fundamental components.

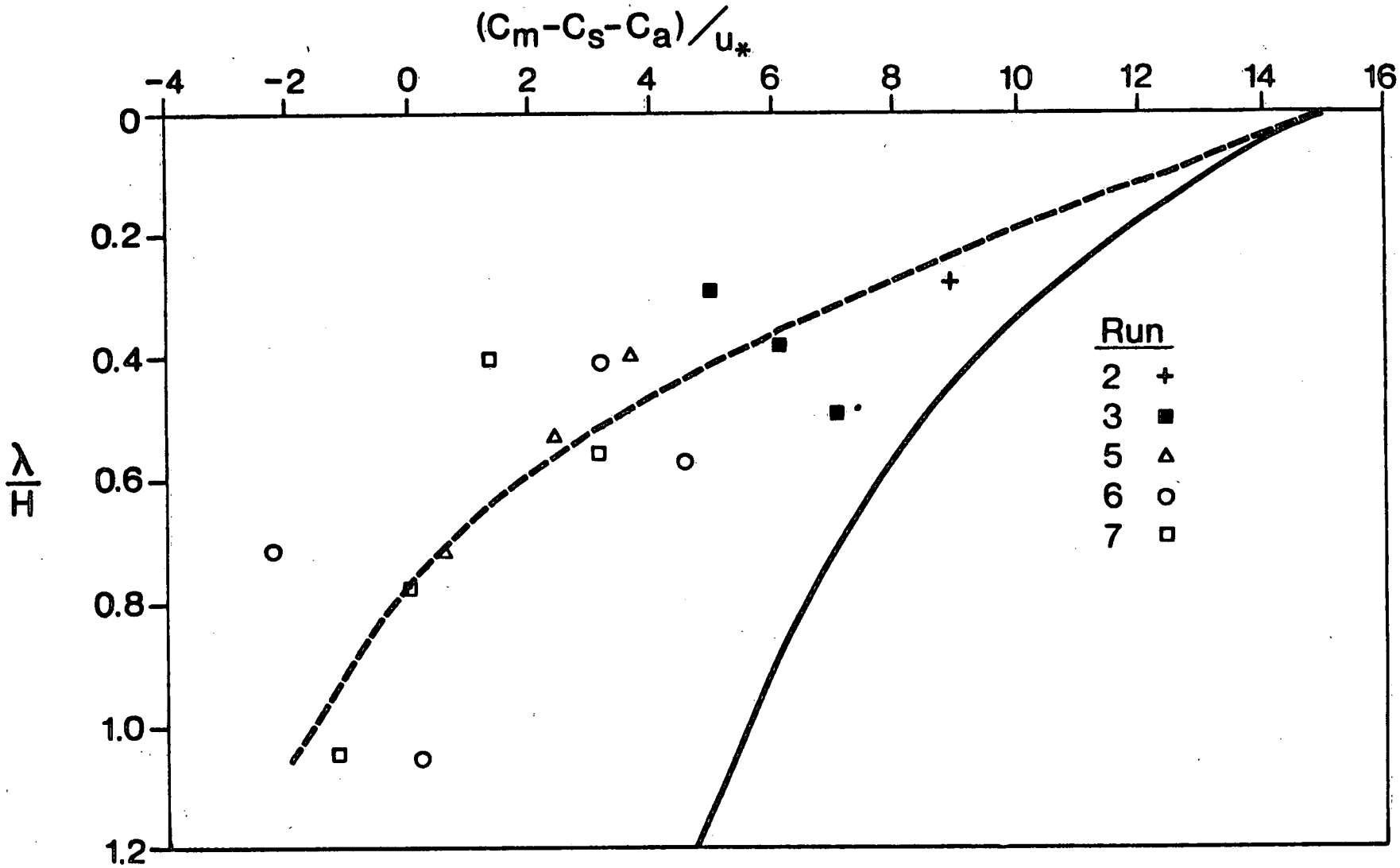

10.8 Measured phase speed minus amplitude dispersion minus wind forcing. This residual normalized by the friction velocity in the water $(-\tau/\rho_w)^{1/2}$ shows a depth dependence similar to the velocity profile measured by Donelan (1977) under similar conditions in the same tank. This similarity is exploited to deduce that the waves are being advected by the wind drift at a speed commensurate with the current at depth z such that kz = 1.

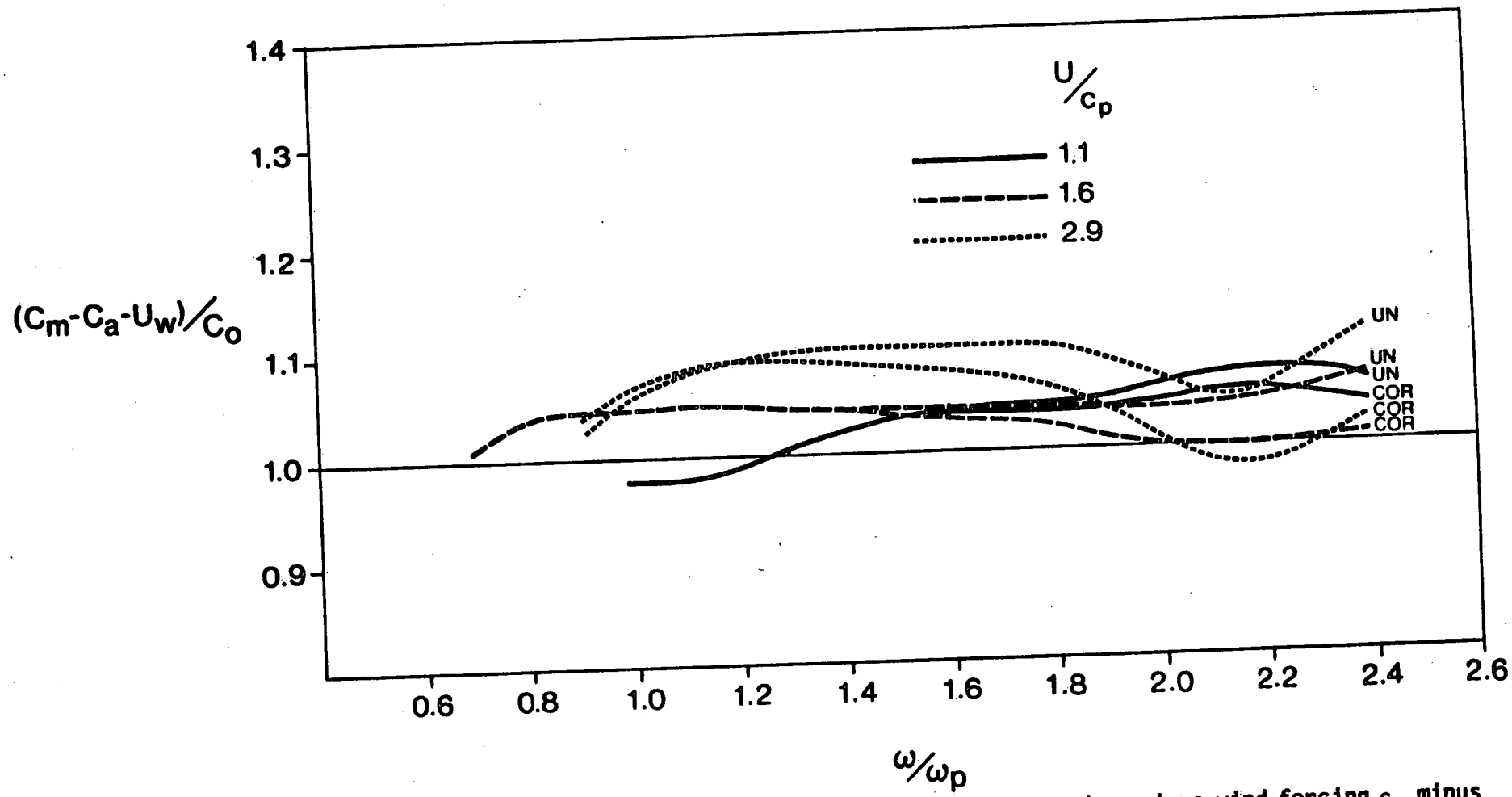

10.9 Phase speed of field waves from the residual of measured speed c_m minus wind forcing c_a minus wind drift U_w. The residual is normalized by the theoretical linear phase speed $c_o = g/\omega$ and graphed versus ω/ω_p. Eighteen field cases have been grouped into three sets by U/c_p. The uncorrected ($c_a = 0$, $U_w = 0$) and corrected curves are designated "UN" and "COR" respectively. The differences are larger for large U/c_p since this corresponds to strong winds and short waves.

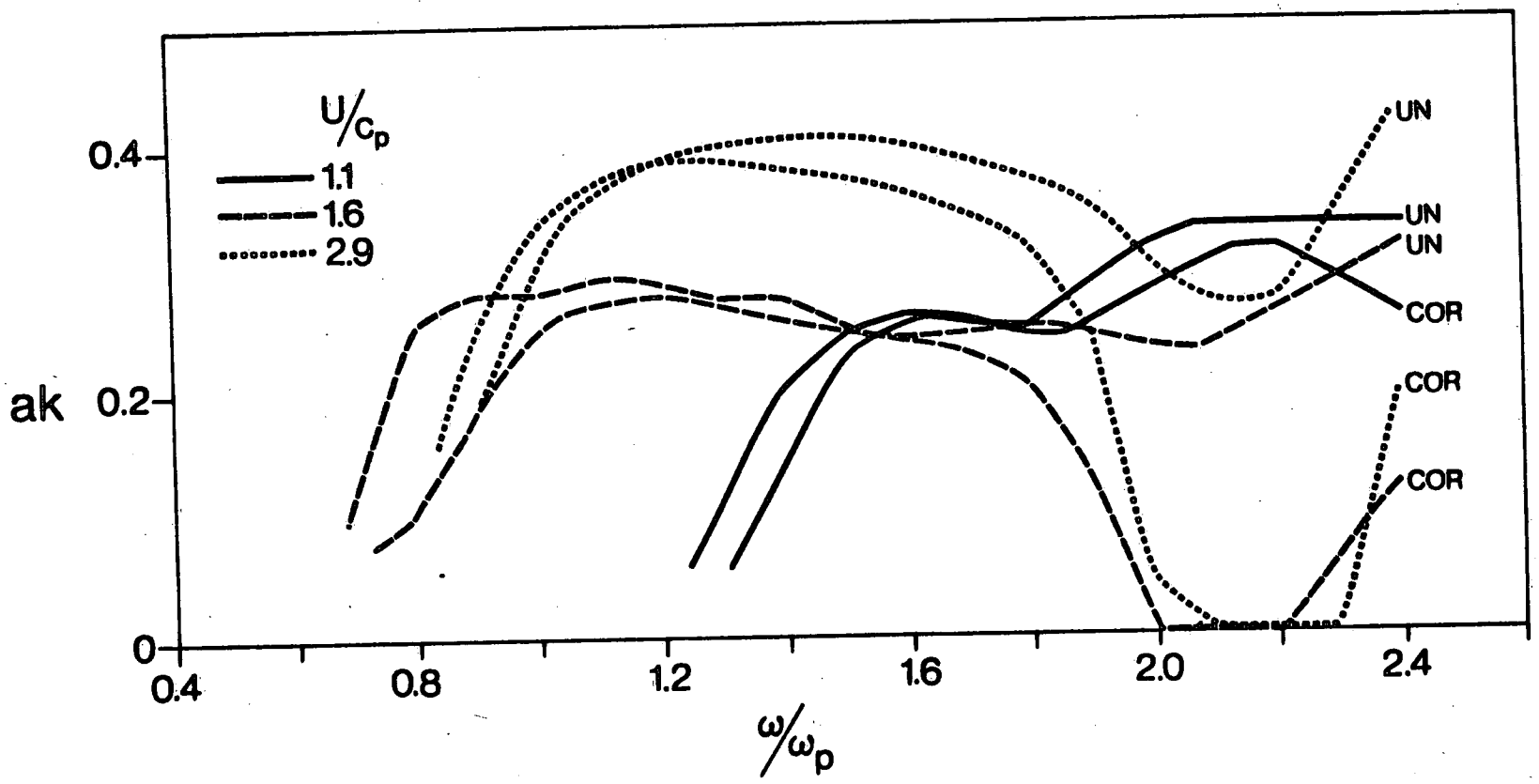

10.10 Wave slope deduced from figure 10.9 and relation (2.8).

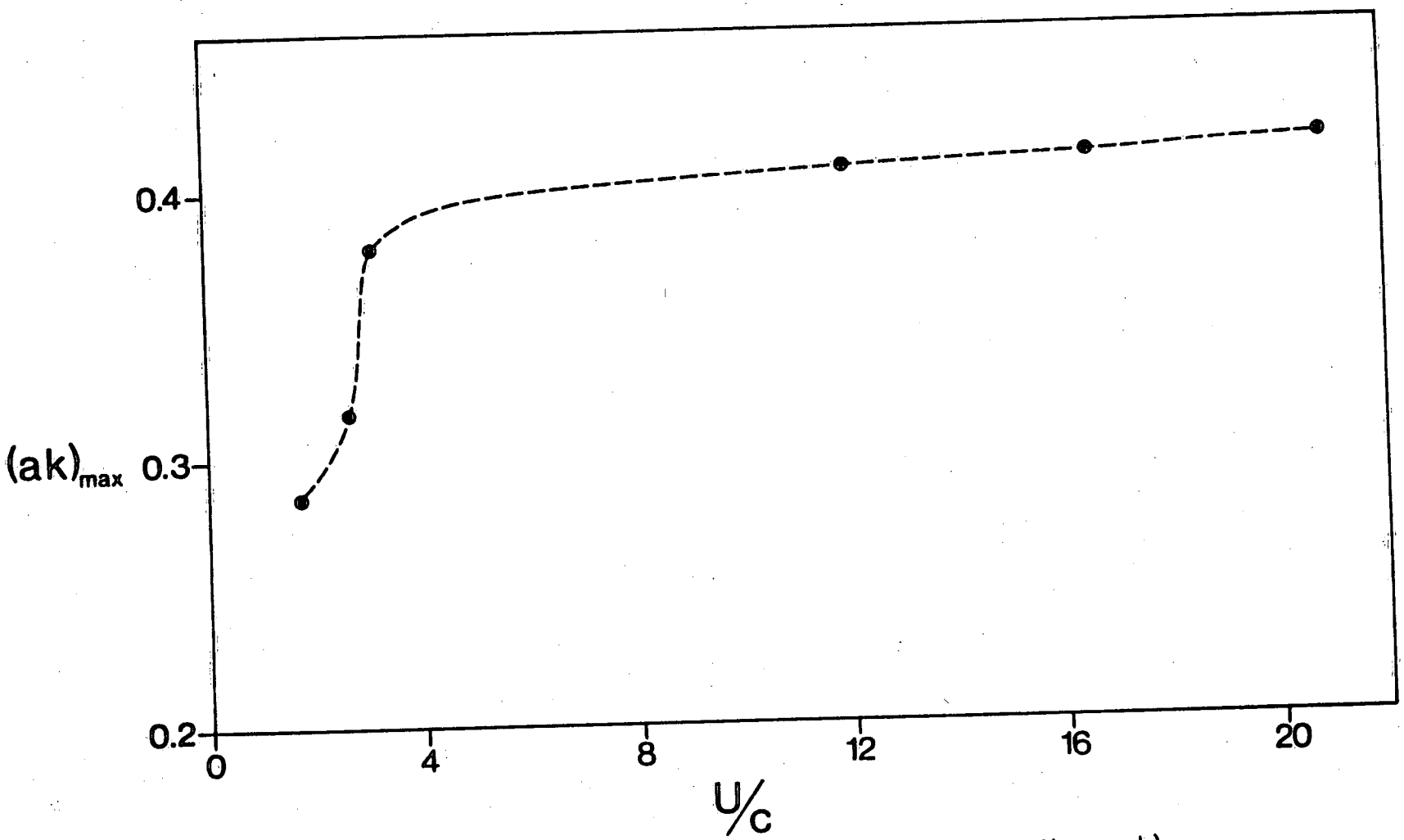

10.11 The maximum observed steepness (not necessarily near the peak) versus U/c, where c (=g/ω) is the theoretical linear phase speed for the maximally steep waves. Laboratory (figure 10.7) and field (figure 10.10) data are both represented.

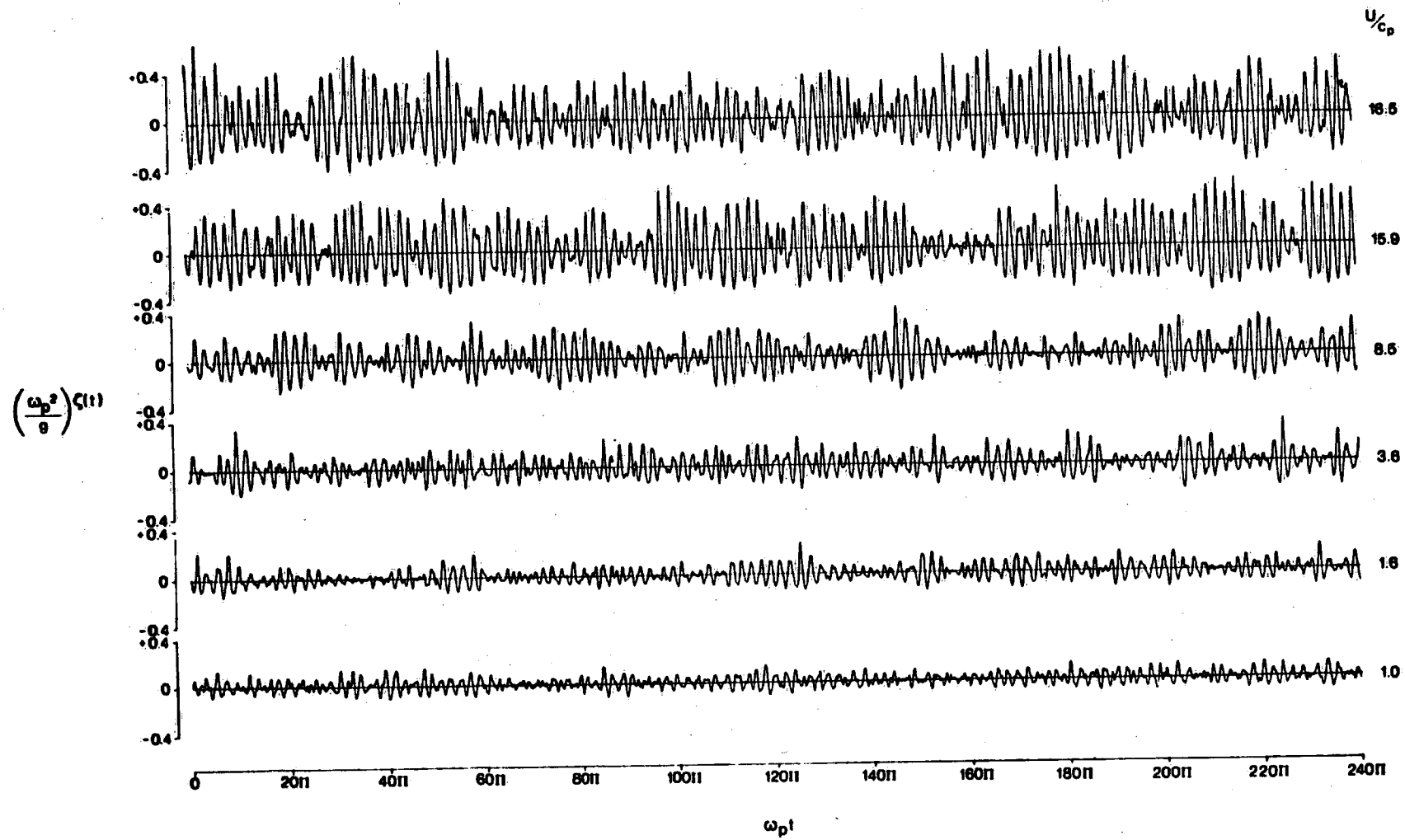

10.12 Time series of surface elevation normalized by the theoretical wave number of the peak $k_p = \omega_p^2/g$.

Run 339064 $\frac{U\cos\theta}{c_p} = 1.5$ $\omega_p = 2.13$

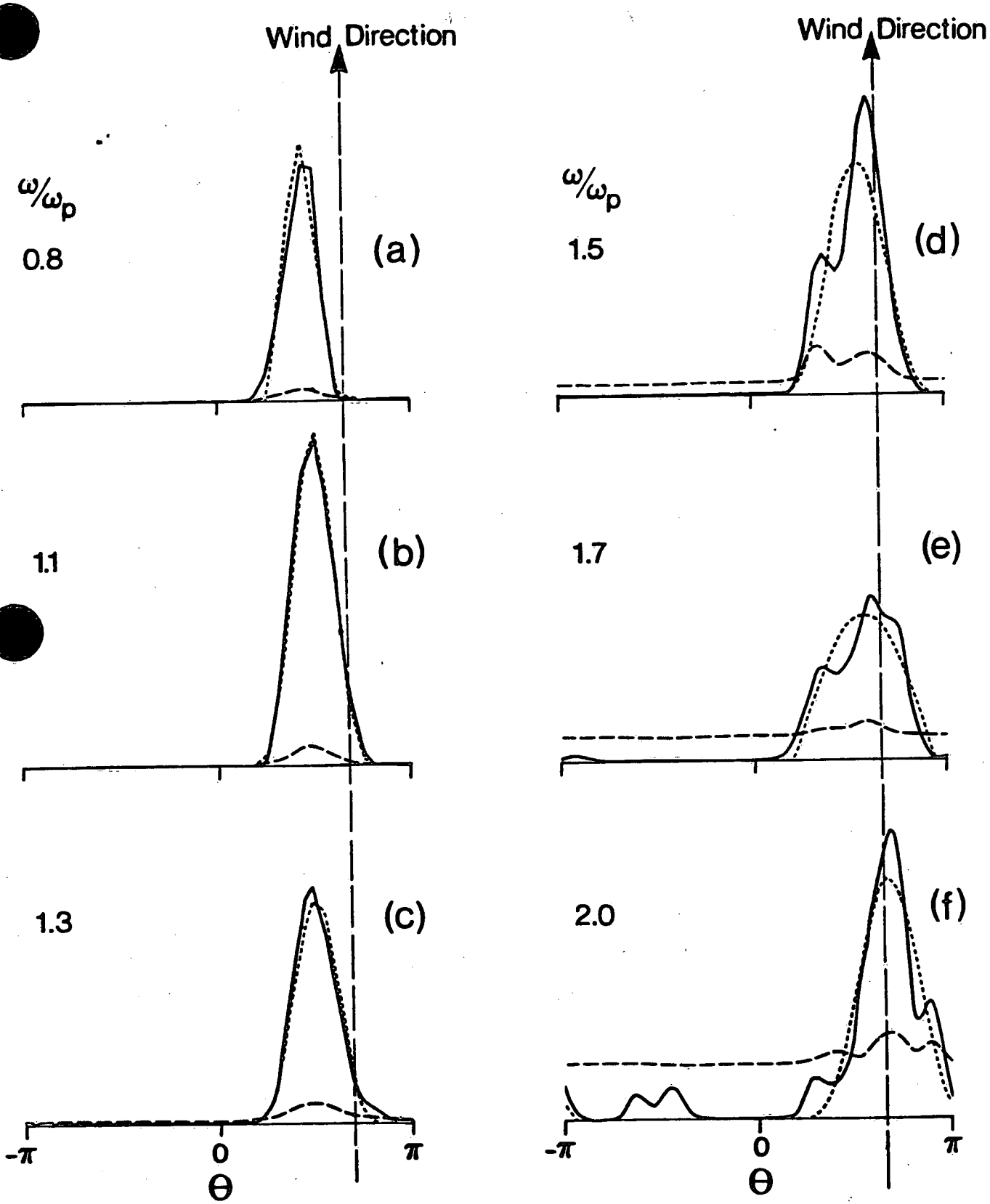

DIRECTIONAL SPECTRA F(ω,θ)

11.1 Directional (or polar) spectra F (ω,θ), (2.25) corresponding to the wave-number spectra of figure 6.1. The dotted line is the parametric representation described in §7.2; the dashed line is a measure of the error in the estimation of F.

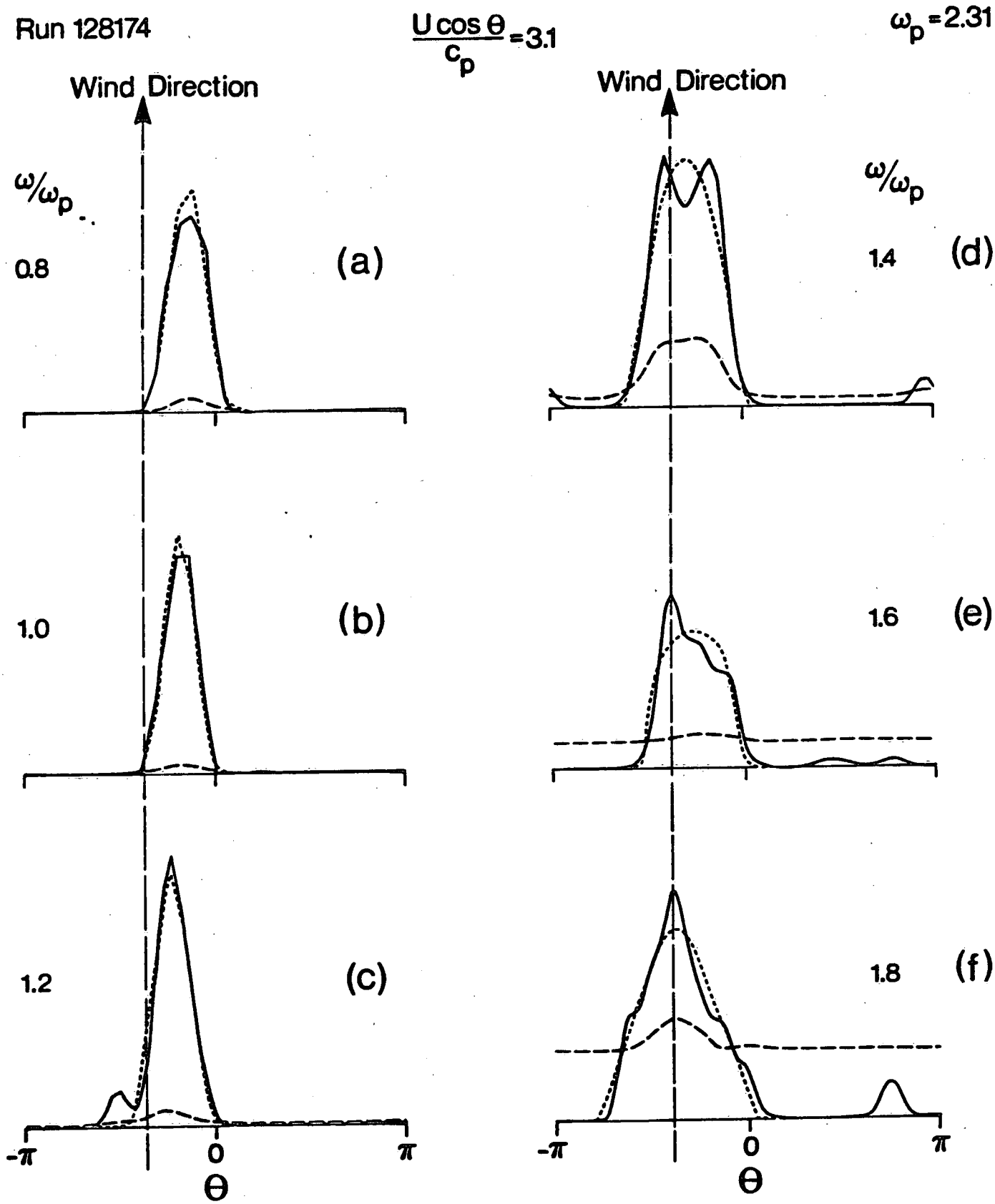

DIRECTIONAL SPECTRA $F(\omega,\theta)$

11.2 Directional spectra corresponding to the wave-number spectra of figure 6.2

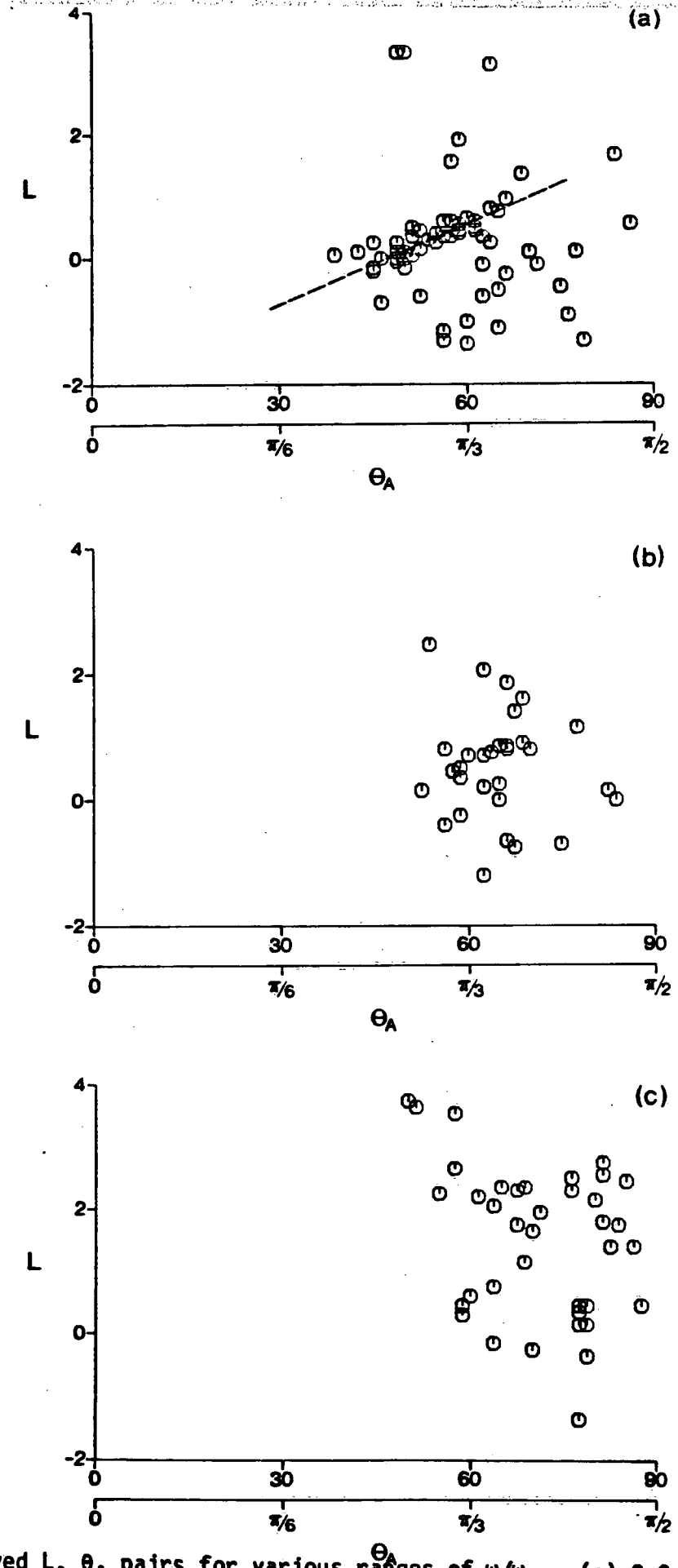

11.3 Observed L, θ_A pairs for various ranges of ω/ω_p. (a) $0.9 < \omega/\omega_p < 1.1$; (b) $1.1 < \omega/\omega_p < 1.25$; (c) $1.25 < \omega/\omega_p < 2$.

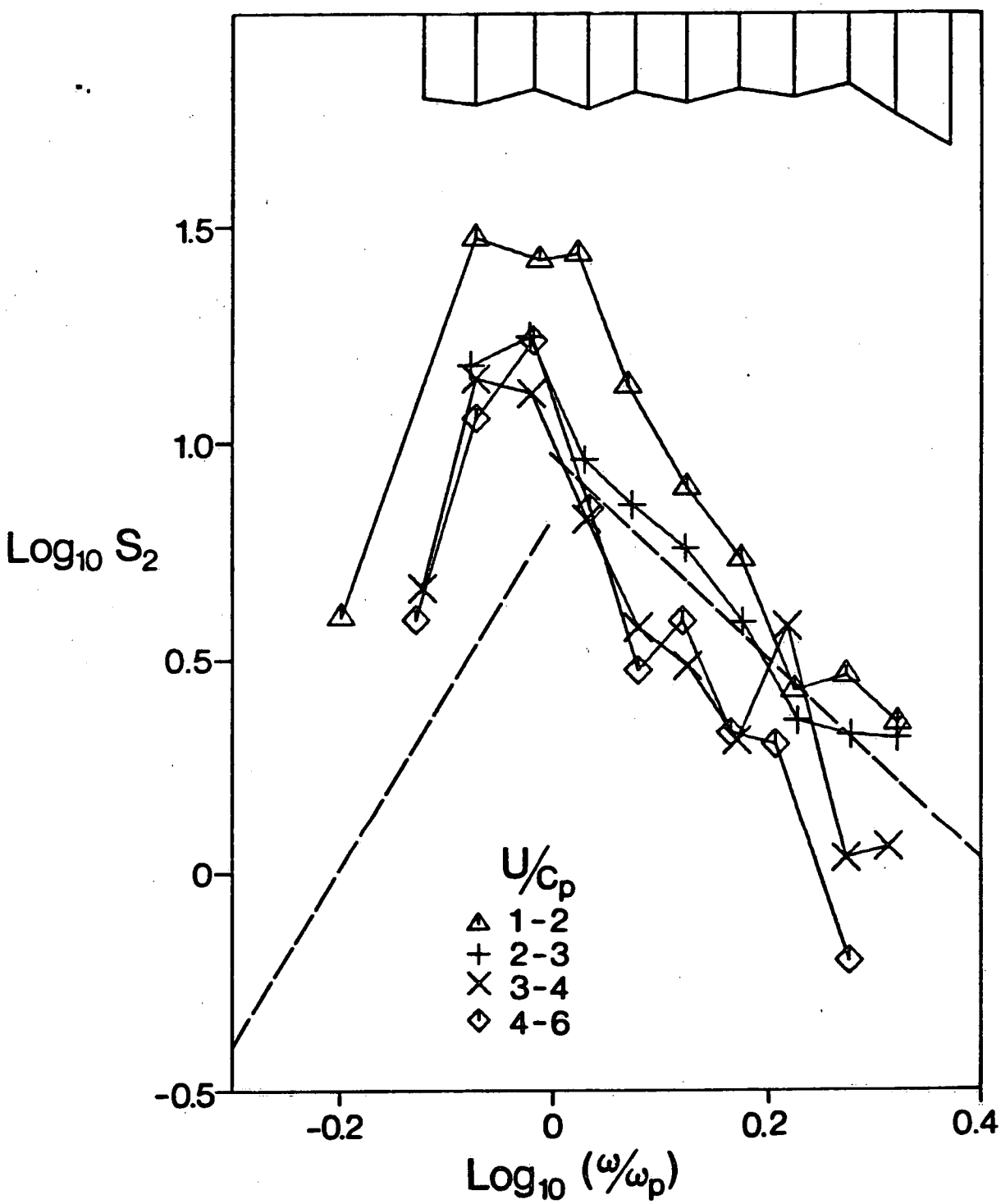

11.4 The s parameter calculated from the first two Fourier coefficients versus ω/ω_p. The data are grouped in U/c_p classes. The dashed lines are taken from Hasselmann et al. (1980). The vertical bars at the top of the figure are an estimate of the 90% confidence limits based on the standard error of the mean.

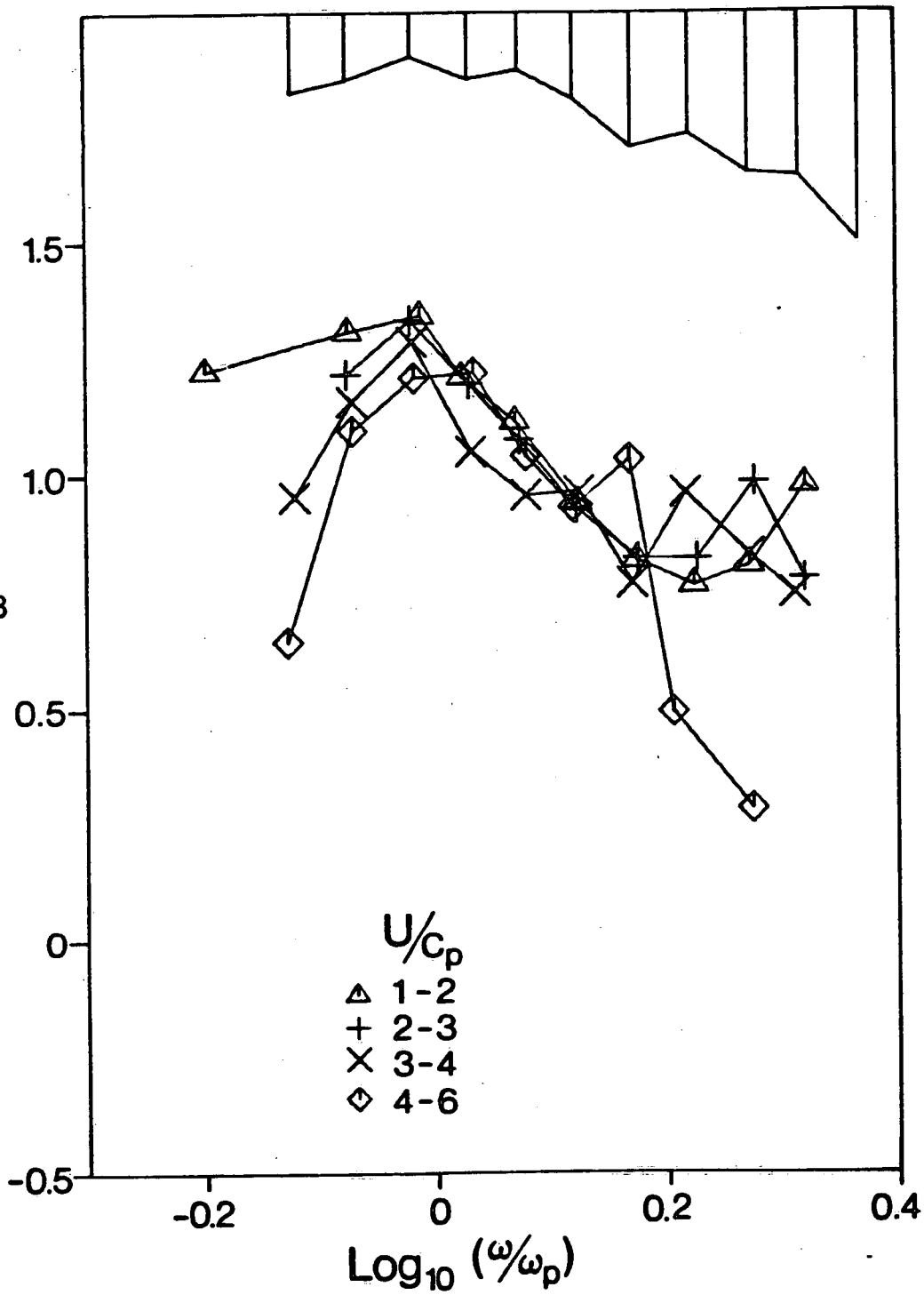

11.5 The s parameter calculated from the half height of observed polar distributions.

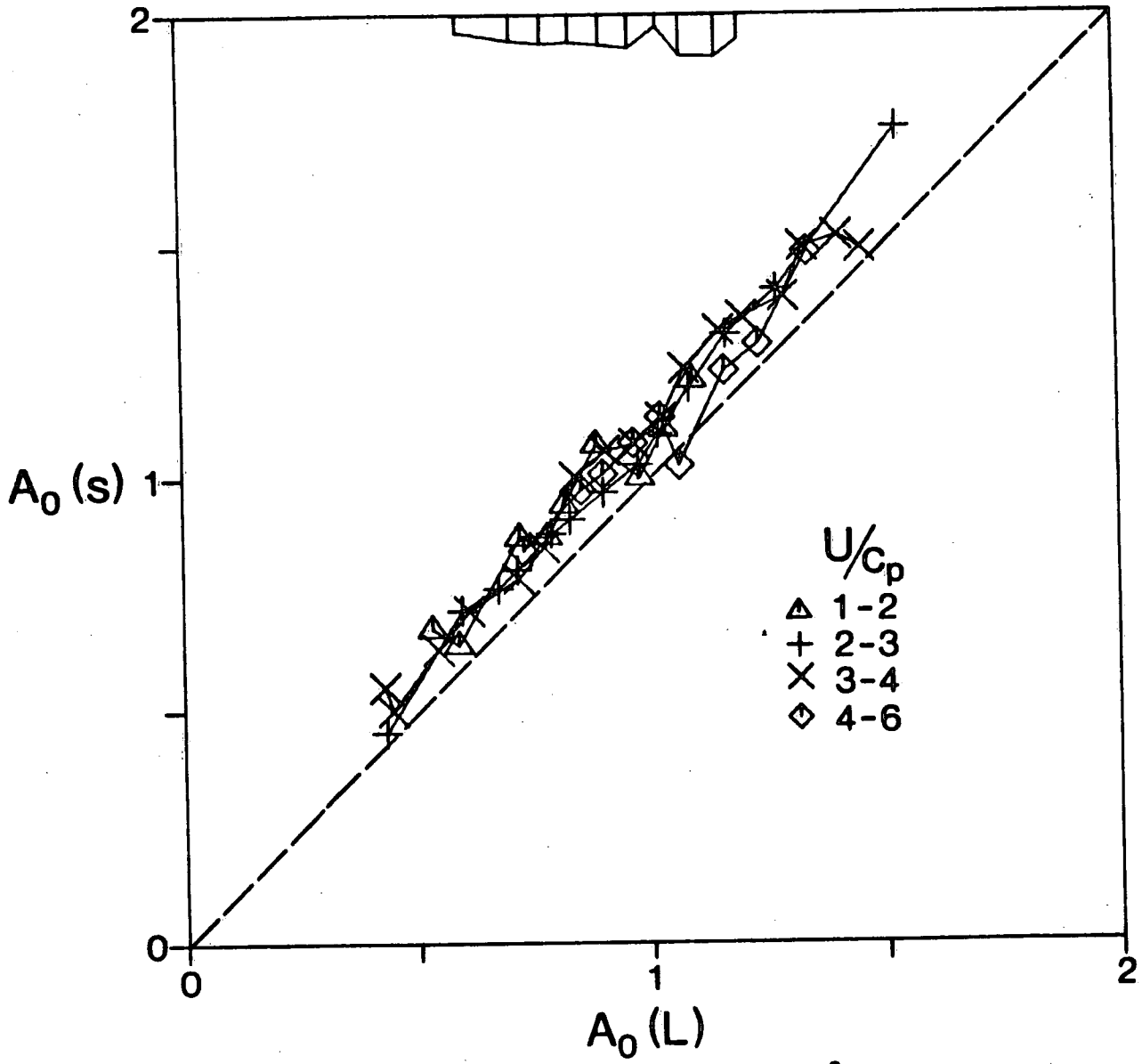

11.6 Comparison of the height of the peak of the $\cos^{2s}(\theta/2)$ distribution $A_0(s)$ with the height of the (L, θ_A) test model $A_0(L)$. The distributions have equal integrals over θ $(=\Phi(\omega))$ and the same half-height widths.

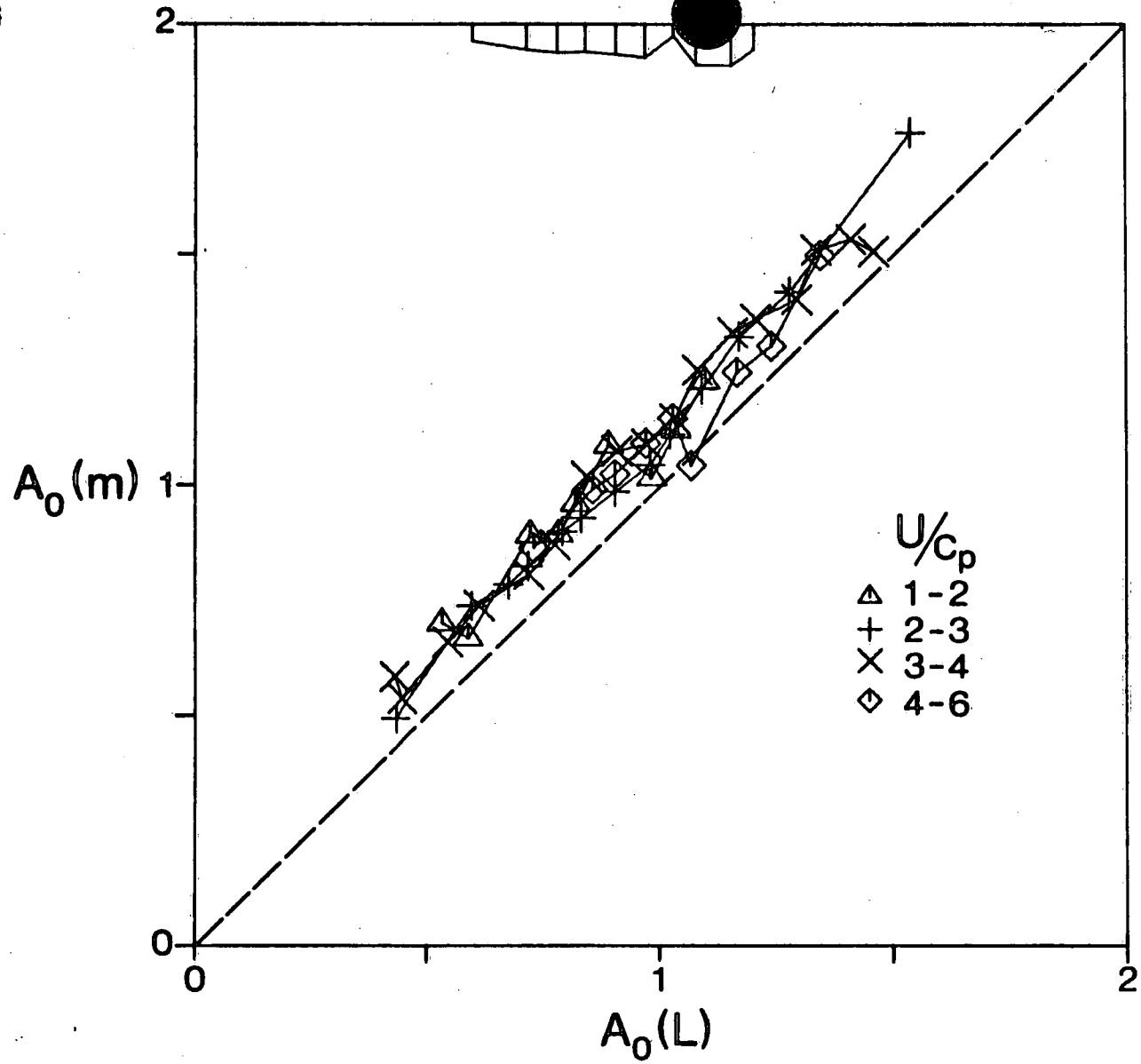

11.7 Comparison of the height of the peak of the $\cos^{2m}\theta$ distribution $A_0(m)$ with the height of the (L, θ_A) model $A_0(L)$.

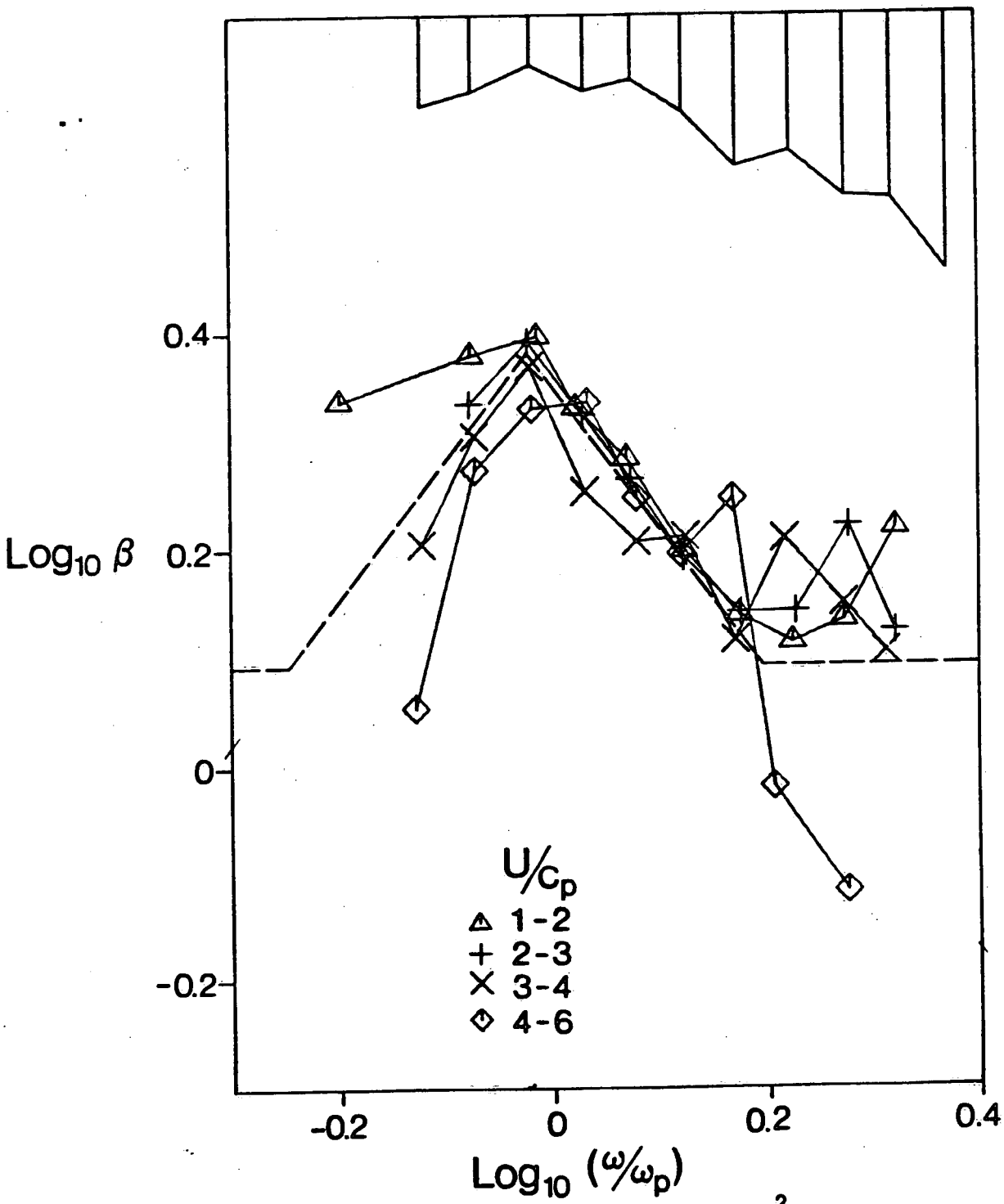

11.8 The β parameter derived from fitting $\mathrm{sech}^2\,(\beta\theta)$ to the half-height width of the test model.

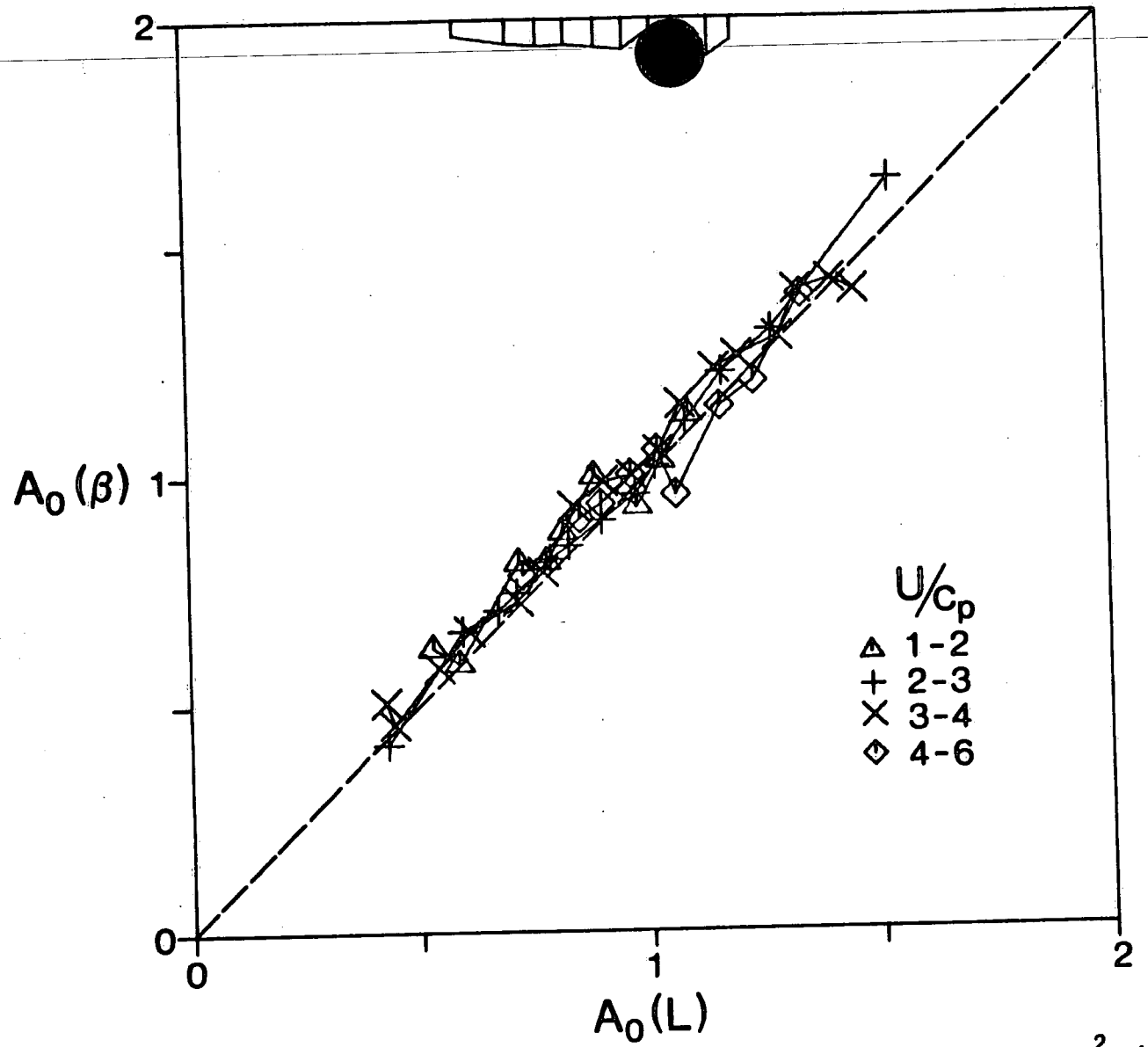

11.9 Comparison of the height of the peak of the $\mathrm{sech}^2(\beta\theta)$ distribution $A_0(\beta)$ with the height of the (L, θ_A) model $A_0(L)$.

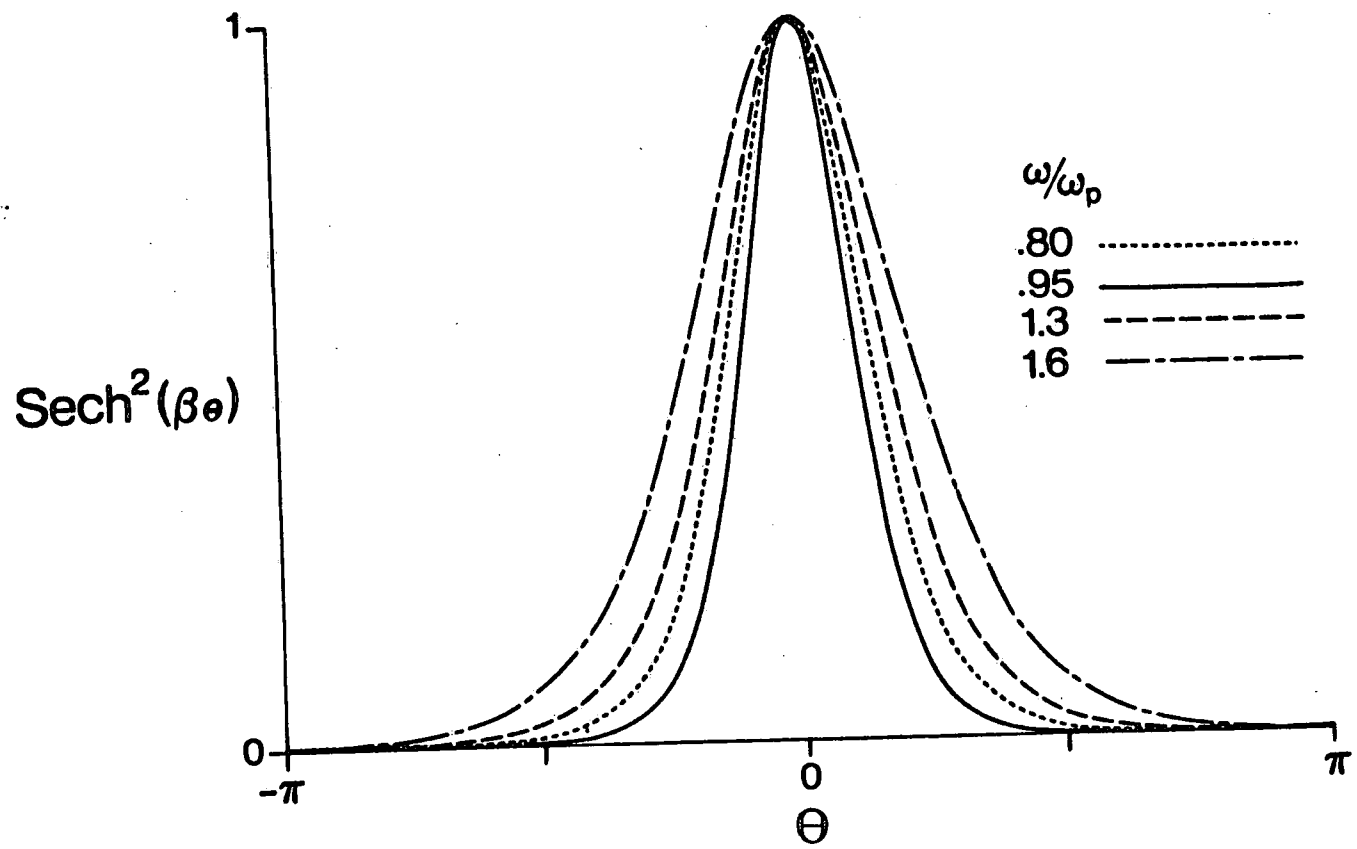

11.10 The sech^2($\beta\theta$) spreading function for various ω/ω_p.

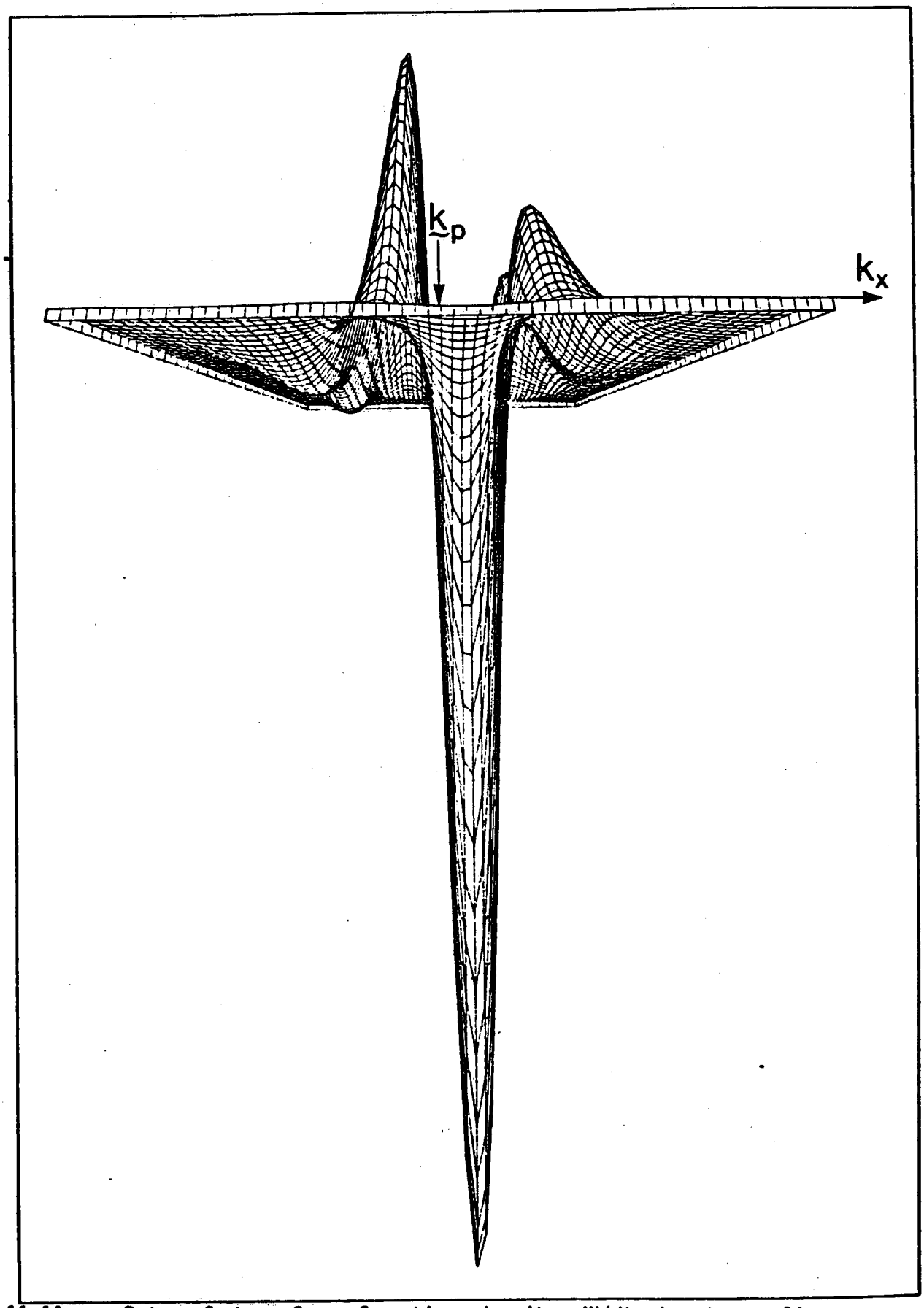

11.11 Rate of transfer of action density dN/dt due to nonlinear interaction of waves in a Gaussian spectrum of spectral width 0.3, calculated using the theory of Dungey & Hui (1979). The horizontal plane is the expanded wave-number plane relative to the spectral peak $\underset{\sim}{k}_p$. The vertical scale is arbitrary. This perspective view is along the k_y axis and at 10^0 below the wave-number plane.

15686

ENVIRONMENT CANADA LIBRARY, BURLINGTON
3 9055 1016 7321 7